

Inorganic and Metal-Organic Heterogeneous Catalysts for Hydrogen Energy Applications

Présentée le 15 octobre 2021

Faculté des sciences de base
Laboratoire de simulation moléculaire
Programme doctoral en chimie et génie chimique

pour l'obtention du grade de Docteur ès Sciences

par

Fatma Pelin URAN

Acceptée sur proposition du jury

Prof. A. Züttel, président du jury
Prof. B. Smit, directeur de thèse
Prof. J. G. Vitillo, rapporteuse
Prof. R. D. McIntosh, rapporteur
Prof. K. Sivula, rapporteur

“Science, my lad, is made up of mistakes,
but they are mistakes which it is useful to make,
because they lead little by little to the truth.”
— *Jules Verne, Journey to the Center of the Earth*

To my lovely and caring family.

Acknowledgements

Since this is the end of my PhD journey, I would like to thank the people without whom I would not have been able to complete this thesis.

First and foremost, I would like to express my sincere gratitude to Prof. Berend Smit for giving me the opportunity to conduct exciting research projects with lots of freedom and support. I am deeply indebted to his invaluable guidance, profound belief in my skills, and endless encouragement during my research. I am grateful to Prof. Kyriakos Stylianou for all the scientific advice, fruitful discussions, and motivation in the first two years of my PhD. I must also thank Dr. Christopher Ireland for his plentiful experience, willingness to help, and answering my endless questions any time I need.

I would like to express my deepest appreciation to Prof. Andreas Züttel, Prof. Kevin Sivula, Prof. Jenny Vitillo, and Prof. Ruairaidh McIntosh for their valuable time to review my thesis and being a part of my oral exam committee. I would like to extend my sincere thanks to all the collaborators who helped me while seeking the answers for most interesting questions. In particular, I would like to thank Dr. Emad Oveisi, Dr. Pascal Schouwink, Dr. Mounir Mensi, and Dr. Amber Mace for their contribution to my research.

I wish to thank our administrative assistant, Evelyn Ludi, for uplifting us with her joyful personality. I also appreciate all the help I received from Laurent Seydoux, Annabelle Coquoz, Fabio Taddei, Cédric Passerini, Jean Perruchoud, Robin Délèze, and Anne Lene Odegaard at different steps of my PhD study.

Being a part of LSMO has been a great experience for me, not only because of academic reasons but also thanks to the amazing friends that I shared all the unforgettable memories with. I would like to thank Mish for always being there for me with her warmest heart and soul, Ozge for her genuine and trustworthy friendship, Alina for being my rock and my joy, Sam for her sincerity and being filled with compassion, Bardiya for his positive attitude and helpfulness, Chris for his advice and tolerating my food recommendations, and Nancy for her friendliness and sympathy. I should also thank the former members of LSMO: Arun for

Acknowledgements

sharing his food enthusiasism with me, Tu for his mentorship and helpful discussions, and Andrzej for his good humour and nice friendship. I would also like to thank Gio for the hiking adventures and amazing food. Thanks should also go to my colleagues in the computational part of LSMO. My special thanks go to Andres for our enjoyable collaboration in the last year of our PhD studies. I also had a chance to work closely with Sauradeep, Elias, Kevin, Mehrdad, Sasha, Miriam, Mohamad and Daniele; which was a great pleasure. I must say that having our doggies Peanut, Lila and Luna around me was a great privilege that turning all the stressful moments to the joyful play times. Although we are apart by thousands of kilometers, the support of my dearest friends in Istanbul has been always with me during this journey. Tuğçe, Ezgi and Melis; I am thankful that you were always by my side whenever I was feeling blue.

Finally, I would like to express my deepest gratitude to my family. PhD had been an unprecedented period of my life where I experienced lots of mixed feelings. During all the ups and downs of this phase, my husband Arda was always there for me with his endless love, support and compassion. I feel extremely grateful every day to have him by my side since our high school years, and I am looking forward to start the new journeys together. My parents Ali and Necmiye, and my sister Aylin; without your positivity, support and endless love that I feel every minute of my life, I could not be where I am now. It will not be enough no matter how much I thank you. Benim ailem olduğunuz için çok şanslıyım. Sizi çok seviyorum ve bu tezi size adıyorum.

Sion, July 2021

Fatma Pelin Uran

Abstract

The main focus of this thesis is the exploration of inorganic and metal-organic heterogeneous catalysts for hydrogen (H_2) energy applications. In particular, we investigated metal nanoparticles (NPs) and metal-organic frameworks (MOFs) for their employment in different perspectives of H_2 energy. Our investigation includes; (i) H_2 generation from water by MOFs, (ii) H_2 release from a chemical storage medium (ammonia borane (AB)), and (iii) utilization of H_2 for hydrogenation reactions. Our research was aimed at understanding the catalytic behavior of these materials and proposing approaches for improving their efficiency and sustainability.

MOFs have been promising candidates for the photocatalytic H_2 evolution reaction (HER) from water. As yet, the main criteria for MOFs to be considered as “photocatalysts” have mostly been their light absorption capability, optical band gap and the alignment of their band edges with respect to the relevant redox levels. In **Chapter 2**, we present the synergy between the experiments and computations, to show that a deeper understanding is needed for evaluating their potential. We investigated isostructural pyrene-based MOFs (M-TBAPy, where TBAPy = 4,4',4''-(pyrene-1,3,6,8-tetrayl)tetrabenzic acid and M = Sc, Al, and In), which have similar band gap energies. Despite all being isostructural MOFs, Sc-TBAPy performed better in H_2 generation compared to its Al and In counterparts. Our investigation allowed us to identify that, in addition to optical and electronic properties, the chemical characteristics of the metal nodes and the morphology of the structure also play an important role on the photocatalytic HER rate. We conclude that all these key factors should be studied together for the optimization of photocatalytic activity. The knowledge obtained in this study can be transferred to other MOF photocatalysts.

AB has been considered as a promising H_2 storage medium owing to its high gravimetric capacity. Although non-noble metal NPs have been used for the release of H_2 from AB, they might suffer from deactivation during cycles. In **Chapter 3**, we demonstrate that the *in-situ* formation of copper NPs (Cu^0 NPs) upon reduction of the earth-abundant Jacquesdietrichite mineral ($Cu_2[(BO)(OH)_2](OH)_3$) with AB can provide an alternative solution for stability issues. The mineral catalyzes the release of almost all H_2 from AB. During the reaction, the Cu^{II} ions

Abstract

in mineral are *in-situ* reduced to Cu⁰ NPs, and after the reaction, following exposure to air, they re-form the fresh mineral. As a consequence, the catalytic activity of mineral remains unchanged over cycles. The regeneration of synthetic mineral gives a new perspective in heterogeneous catalysis.

In **Chapter 4**, we present that our approach presented in Chapter 3 can be applied in industrial hydrogenation reactions. We demonstrated that during the *in-situ* formation of Cu⁰ NPs, the released H₂ gas can be utilized for the reduction of nitroarenes to their corresponding anilines, at room temperature and under ambient pressure. After the nitroarene-to-aniline conversion is complete, regeneration of the mineral occurs upon the exposure of Cu⁰ NPs to air. Thus, the hydrogenation reaction can be performed multiple times without the loss of any activity of Cu⁰ NPs. As a proof-of-concept, the hydrogenation of drug molecules “flutamide” and “nimesulide” was also performed and their corresponding amino-compounds were isolated in high selectivity and yield.

Keywords: Hydrogen energy, photocatalysis, metal-organic frameworks, heterogeneous catalysis, ammonia borane, hydrogenation, copper nanoparticles, in-situ generation.

Résumé

L'objectif principal de cette thèse est l'exploration de catalyseurs hétérogènes inorganiques et organométalliques pour les applications de l'énergie hydrogène (H_2). En particulier, nous avons étudié les nanoparticules métalliques (NPs) et des charpentes métalliques-organiques (MOFs) pour leur emploi dans différentes perspectives de l'énergie de l' H_2 . Notre enquête comprend; (i) H_2 génération à partir de l'eau par les MOF, (ii) la libération d' H_2 à partir d'un milieu de stockage chimique (ammoniac borane (AB)), et (iii) utilisation de H_2 pour les réactions d'hydrogénation. Notre recherche inclut la compréhension du comportement catalytique de ces matériaux et la proposition d'approches pour améliorer leur efficacité et leur durabilité.

Les MOFs ont été des candidats prometteurs pour la réaction d'évolution photocatalytique H_2 (HER) à partir de l'eau. Jusqu'à présent, les principaux critères pour lesquels les MOFs doivent être considérés comme des "photocatalyseurs" ont été principalement leur capacité d'absorption de la lumière, leur bande interdite optique et leurs alignements de bandes. Dans le **Chapitre 2**, nous présentons la synergie entre les expériences et les calculs, pour montrer qu'une meilleure compréhension est nécessaire pour évaluer leur potentiel. Nous avons étudié les MOFs isostructuraux à base de pyrène (M-TBAPy, où TBAPy = 4,4',4'',4'''-(pyrene-1,3,6,8-tetrayl)tetrabenzoinic acid et M = Sc, Al, and In), qui ont des énergies de bande interdite similaires. Bien que tous soient des MOFs isostructuraux, Sc-TBAPy a mieux performé dans la génération d' H_2 par rapport à ses homologues Al et In. Notre enquête nous a permis d'identifier l'effet des caractéristiques morphologiques et liées aux métaux sur le taux de HER photocatalytique. Nous concluons que tous ces facteurs clés doivent être étudiés ensemble pour l'optimisation de l'activité photocatalytique. Les connaissances acquises dans cette étude peuvent être transférées à d'autres MOFs.

AB a été considéré comme un support de stockage H_2 prometteur en raison de sa grande capacité gravimétrique. Bien que des NP de métaux non nobles aient été utilisées pour la libération de H_2 de AB, elles pourraient souffrir de désactivation au cours des cycles. Dans le **Chapitre 3**, nous démontrons que la formation *in-situ* de NPs de cuivre (Cu^0 NPs) lors de la réduction du minéral Jacquesdietrichite abondant en terre ($Cu_2[(BO)(OH)_2](OH)_3$) avec de

Résumé

l'ammoniaque borane (AB) peut fournir une solution alternative aux problèmes de stabilité. Le minéral catalyse la libération de presque tous les H_2 d'AB. Pendant la réaction, les ions Cu^{II} dans le minéral sont *in-situ* réduits en Cu^0 NPs, et suite la réaction, après exposition à l'air, ils sont re formant le minéral frais. En conséquence, l'activité catalytique du minéral reste inchangée au fil des cycles. La régénération du minéral synthétique en l'absence de tout apport d'énergie supplémentaire donne une nouvelle perspective en catalyse hétérogène.

Dans le **Chapitre 4**, nous présentons que notre approche présentée au Chapitre 3 peut être appliquée dans les réactions d'hydrogénation industrielle. Nous avons démontré que lors de la formation *in-situ* de Cu^0 NPs, le gaz H_2 libéré peut être utilisé pour la réduction des nitroarènes en leurs anilines correspondantes, à température ambiante et sous pression ambiante. Une fois la conversion nitroarène-aniline terminée, la régénération du minéral se produit lors de l'exposition des NPs Cu^0 à l'air. Ainsi, la réaction d'hydrogénation peut être effectuée plusieurs fois sans perte de toute activité de Cu^0 NPs. Comme preuve de concept, l'hydrogénation des molécules médicamenteuses "flutamide" et "nimesulide" a également été réalisée et leurs composés amino correspondants ont été isolés avec une sélectivité et un rendement élevés.

Mots clés : Énergie hydrogène, photocatalyse, charpentes métalliques-organiques, catalyse hétérogène, ammoniac-borane, hydrogénation, nanoparticules de cuivre, génération *in-situ*.

Contents

Acknowledgements	i
Abstract (English/Français)	iii
List of Figures	ix
List of Tables	xi
List of Abbreviations	xiii
1 Hydrogen Energy: A Summary	1
1.1 Importance of Hydrogen Energy	1
1.2 Generation of Hydrogen Energy	3
1.2.1 Photocatalytic Hydrogen Evolution Reaction (HER) from Water	4
1.3 Storage of Hydrogen Energy	6
1.3.1 Challenges in Hydrogen Storage	6
1.3.2 Hydrogen Storage Methods	7
1.4 Catalytic Hydrogenation Reactions	9
1.5 Thesis Objectives and Organization	10
2 Optimized Photocatalytic Hydrogen Generation with Pyrene-Based MOFs	11
2.1 Introduction	11
2.1.1 MOFs for Photocatalytic HER	11
2.1.2 Pyrene-Based MOFs for Photocatalytic HER	13
2.2 Toward Optimal Photocatalytic HER with Pyrene-Based MOFs	15
2.2.1 Synthesis and Characterization	16
2.2.2 Photocatalytic Activity of M-TBAPy MOFs	17
2.2.3 Investigation of Morphological Characteristics	25
2.3 Summary and Conclusions	27
3 Hydrogen Release from Ammonia Borane by Cu-based Mineral	29
3.1 Introduction	29

Contents

3.1.1	Ammonia Borane as Hydrogen Storage Medium	29
3.1.2	Cu ⁰ NPs for AB Hydrolysis: A Stability Issue to Consider	31
3.2	In-Situ Generation of Cu ⁰ NPs for AB Hydrolysis	33
3.2.1	Synthesis and Characterization	33
3.2.2	AB Hydrolysis	34
3.3	Summary and Conclusions	39
4	Hydrogenation of Nitroarenes to Anilines by Ammonia Borane Hydrolysis	41
4.1	Introduction	41
4.2	Hydrogenation of Nitroarenes by <i>in-situ</i> Generated Cu ⁰ NPs	42
4.2.1	Hydrogenation of Nitroarenes to Anilines	43
4.2.2	Hydrogenation of Drug Molecules	47
4.3	Summary and Conclusions	48
5	Conclusions and Outlook	51
5.1	Summary	51
5.2	Future Work	52
A	Appendices	55
A.1	Materials	55
A.2	Experimental Methods	55
A.3	Supporting Information for Chapter 2	57
A.3.1	Material Synthesis	57
A.3.2	Photocatalytic Experiments	57
A.3.3	Computational Details	58
A.3.4	Structural and Optical Characterization	59
A.3.5	Calculation of Apparent Quantum Yield	59
A.4	Supporting Information for Chapter 3	65
A.4.1	Characterization Experiments	66
A.5	Supporting Information for Chapter 4	70
A.5.1	UV-Vis and ¹ H NMR Spectra	71
	Bibliography	96
	Curriculum Vitae	97

List of Figures

1.1	Overview of the generation and applications of H ₂ .	3
1.2	Schematic energy diagram of photocatalytic water splitting.	5
1.3	Summary of physical and material-based H ₂ storage methods.	9
2.1	Promising features of MOFs for photocatalysis.	12
2.2	Photo-induced charge transfer mechanisms in MOFs.	13
2.3	Structure of TBAPy ligand.	14
2.4	Structural characterization of M-TBAPy MOFs.	17
2.5	Photocatalytic HER rates of M-TBAPy MOFs.	18
2.6	Fundamental band gaps of M-TBAPy MOFs.	19
2.7	Band structure calculations and CBM and VBM orbitals of M-TBAPy MOFs.	20
2.8	Symmetric and rotated structures of Sc-TBAPy.	21
2.9	UV-Vis spectra of M-TBAPy MOFs.	23
2.10	nTAS and excitation spectra of M-TBAPy MOFs.	26
2.11	Characterization and photocatalytic performances of Sc-MOFs.	27
3.1	AB as H ₂ storage medium.	30
3.2	Plausible mechanism of AB hydrolysis on a catalyst.	31
3.3	Structure of Jacquesdietrichite mineral.	34
3.4	Confirmation of synthetic version of Jacquesdietrichite mineral.	35
3.5	Optimization of reaction conditions.	36
3.6	Formation of <i>in-situ</i> generated Cu ⁰ NPs.	37
3.7	Schematic representation of AB hydrolysis.	38
3.8	Regenerability of synthetic mineral.	39
4.1	Simultaneous AB hydrolysis and hydrogenation of nitroarenes.	43
4.2	Nitrobenzene to aniline hydrogenation.	44
4.3	Regeneration of synthetic mineral.	47
4.4	¹ H NMR spectra of commercial and hydrogenated flutamide.	48
4.5	¹ H NMR spectra of commercial and hydrogenated nimesulide.	49

List of Figures

A.1	Le Bail fit obtained from the PXRD data of Sc-TBAPy.	61
A.2	Characterization of M-TBAPy MOFs.	61
A.3	Photoluminescence spectra of M-TBAPy MOFs.	62
A.4	Optimization of photocatalytic reaction conditions.	62
A.5	UV-Vis and PXRD analyses of Sc-MOFs.	63
A.6	Density of states of M-TBAPy MOFs.	63
A.7	Band structure calculations of phenyl-rotated M-TBAPy MOFs.	64
A.8	The catalytic setup for AB hydrolysis.	66
A.9	Characterization of synthetic mineral.	66
A.10	TEM images of as-synthesized mineral and Cu ⁰ NPs.	67
A.11	ICP-OES analysis of as-synthesized mineral.	67
A.12	Kinetics of H ₂ evolution from AB.	68
A.13	Optimization of hydrogenation reaction conditions.	71
A.14	Determination of 4-chloroaniline yield.	72
A.15	Determination of 4-fluoroaniline yield.	72
A.16	Determination of 4-bromoaniline yield.	73
A.17	Determination of 1,3-diaminobenzene yield.	73
A.18	Determination of 3-aminopyridine yield.	74
A.19	¹ H NMR spectra of aniline.	74
A.20	¹ H NMR spectra of 4-chloroaniline.	75
A.21	¹ H NMR spectra of 4-fluoroaniline.	75
A.22	¹ H NMR spectra of 4-bromoaniline.	76
A.23	¹ H NMR spectra of 1,3-diaminobenzene.	76
A.24	¹ H NMR spectra of 3-aminopyridine.	77
A.25	¹ H NMR spectra of hydrogenated flutamide and nimesulide.	78
A.26	Determination of hydrogenated flutamide yield.	79
A.27	Determination of hydrogenated nimesulide yield.	79

List of Tables

1.1	Energy densities of common fuels.	2
2.1	Ground state and optical bandgaps of M-TBAPy MOFs.	22
4.1	Hydrogenation of various nitroarenes to anilines.	46
A.1	HER rates of M-TBAPy MOFs irradiated at 400 and 450 nm.	60
A.2	Photoluminescence lifetimes of M-TBAPy MOFs.	60
A.3	Catalytic activity of some Cu-based catalysts for AB hydrolysis.	69
A.4	Catalytic activity of some Cu-based catalysts for nitrobenzene hydrogenation. .	80

List of Abbreviations

AB : Ammonia Borane
BET : Brauner-Emmett-Teller
 BO_2^- : Borate Ion
CB : Conduction Band
CBM : Conduction Band Minimum
CO : Carbon Monoxide
 CO_2 : Carbon Dioxide
CTAB : Cetyltrimethylammonium Bromide
 Cu^0 NPs : Copper Nanoparticles
 D_2O : Deuterated Water
DFT : Density Functional Theory
DMF : Dimethylformamide
FTIR : Fourier Transform Infrared Spectroscopy
g : Gram
GC : Gas Chromatography
GSB : Ground State Bleach
h : Hour
 H_2 : Hydrogen
 H_2O : Water
HCl : Hydrochloric Acid
HER : Hydrogen Evolution Reaction
 HNO_3 : Nitric Acid
HOMO : Highest Occupied Molecular Orbital
ICP-OES : Inductively Coupled Plasma - Optical Emission Spectrometry
LC : Ligand-Centered
LLCT : Ligand to Ligand Charge Transfer
LMCT : Ligand to Metal Charge Transfer
LUMO : Lowest Unoccupied Molecular Orbital
MC : Metal-Centered
mg : Milligram

Chapter 0. List of Abbreviations

min : Minute
mL : Milliliter
MLCT : Metal to Ligand Charge Transfer
MMCT : Metal to Metal Charge Transfer
mmol : Millimole
MOF : Metal-Organic Framework
 ^1H NMR : Proton Nuclear Magnetic Resonance
 N_2 : Nitrogen
 NaBH_4 : Sodium Borohydride
 NH_4^+ : Ammonium Ion
NHE : Normal Hydrogen Electrode
NP : Nanoparticles
nm : Nanometer
 O_2 : Oxygen
OER : Oxygen Evolution Reaction
PL : Photoluminescence
PXRD : Powder X-ray Diffraction
RT : Room Temperature
SEM : Scanning Electron Microscopy
SCXRD: Single Crystal X-Ray Diffraction
TAS : Transient Absorption Spectroscopy
TBAPy : 4,4',4'',4'''-(pyrene-1,3,6,8-tetrayl)tetrabenzoic acid
TEA : Triethylamine
TEM : Transmission Electron Microscopy
TGA : Thermogravimetric Analysis
THF : Tetrahydrofuran
UV : Ultraviolet
UV-Vis : Ultraviolet-Visible
VB : Valence Band
VBM : Valence Band Minimum
XPS : X-Ray Photoelectron Spectroscopy
 λ : Wavelength
 μL : Microliter
 \AA : Angstrom

1 Hydrogen Energy: A Summary

1.1 Importance of Hydrogen Energy

In 1984, a research study on power for the future alleged that: “Without a continuing supply of energy, in the right form, in the right place and at the right price, civilization as we know it today would collapse” [1]. After few decades, it is still a valid argument. One of the most important concerns of the 21st century is to provide sufficient amount of energy sources that can meet the accelerating global energy demand. With the increasing population, developments in technology, and growing industrialization, the energy demand has been augmented in the last decades. The world energy consumption is expected to reach its maximum in the next 20 years; therefore, the possible energy supplies have to be evaluated and secured [2]. Right now, more than 80% of the global energy consumption has been sourced by fossil fuels; such as petroleum, natural gas, and coal [2]. However, the abundance of fossil fuels is finite. Another problem is that, fossil fuels are not environmentally friendly due to the release of greenhouse gases and other pollutants, which results in affecting our environment sorely. Therefore, building an energy system based on a clean, abundant and renewable source has been targeted.

In recent times, hydrogen energy has been recognized as a cleaner candidate compared to fossil fuels and the research on this future energy source has been growing rapidly. At standard temperature and pressure conditions, hydrogen is a colorless, non-toxic and highly combustible diatomic gas with the formula of H_2 [3]. When it burns, the only product is water which makes H_2 clean [4]. Since H_2 has to be generated by using energy from a hydrogen-rich compound, it is considered as an “energy carrier” instead of being fuel itself. Table 1.1 shows that H_2 contains the highest energy per unit mass (143 MJ kg^{-1}), which is three times larger than those of natural gas (53.6 MJ kg^{-1}) and gasoline (46.4 MJ kg^{-1}) [5]. Moreover, unlike conventional petroleum-based fuels and natural gas derivatives, H_2 has a very small and light-weight molecular structure [6]. Although H_2 has been an important raw material in chemical and petrochemical industry for many years, the interest in H_2 energy for different

Table 1.1: Volumetric and gravimetric energy densities of common fuels [6].

Material	Energy per kilogram (MJ kg^{-1})	Energy per liter (MJ L^{-1})
(H_2) (liquid)	143	10.1
(H_2) (compressed, 700 bar)	143	5.6
(H_2) (ambient pressure)	143	0.0107
Methane (ambient pressure)	55.6	0.0378
Natural gas (liquid)	53.6	22.2
Natural gas (compressed, 250 bar)	53.6	9.0
Natural gas	53.6	0.0364
LPG propane	49.6	25.3
LPG butane	49.1	27.7
Gasoline (petrol)	46.4	34.2
Diesel	45.4	34.6
Biodiesel oil	42.2	33

applications has increased immensely in the last decades, not only by researchers but also by industry.

H_2 has the potential as a promising energy carrier in several applications, where fossil fuels are used today. It has been an appealing candidate especially for transportation, where it would offer several advantages for reduced pollution and cleaner environment [7]. Different vehicle companies such as Toyota, Hyundai and Honda have developed cars where H_2 can be either used directly in an internal combustion engine or utilized in a fuel cell [8]. H_2 has started to be considered as an aviation fuel due to the absence of CO_2 emissions after its combustion, as well as its high energy content [9]. Airbus has recently introduced the first zero-emission commercial aircraft named “ZEROe”, which is targeted to be launched by 2035 [10]. The aircraft is planned to be powered by the combustion of liquid H_2 with oxygen (O_2). NASA has used H_2 as rocket fuel in different space shuttle vehicles to deliver crew and cargo to space [11]. H_2 has also been attractive for residential purposes. In 2009, Japan has commercialized the use of fuel cell systems for the residential use (named as “ENE-FARM”), in which the cumulative number of sales has exceeded 150,000 in December 2015 [12]. In this system, the fuel cell extracts H_2 from liquefied petroleum gas and combines it together with ambient O_2 to generate electrical power, while simultaneously capturing residual heat to warm up water. In 2016, Toshiba Corporation introduced a H_2 -based energy supply system called $\text{H}_2\text{One}^{\text{TM}}$ into the market [13]. The system produces H_2 by the electrolysis of water, stores it in the tank, and converts it into electricity when needed. The examples will develop further in the following years with the increasing importance of H_2 energy in our lives.

1.2 Generation of Hydrogen Energy

In order to produce H_2 from different sources, various processes are available. They can be mainly grouped as “conventional” and “renewable” technologies, based on the raw materials used for the H_2 generation. The first category includes fossil fuels, which meet almost the entire H_2 demand on the world currently. The conventional methods used in the industry are: (i) steam reforming of natural gas, (ii) partial oxidation of hydrocarbons, and (iii) coal gasification [14]. The distribution of these methods among the current hydrogen generation methods can be given as: 48% from natural gas, 30% from hydrocarbons (i.e. heavy oils and naphtha), and 18% from coal processes [15]. The main disadvantage of the steam reforming process is that, large amounts of carbon dioxide (CO_2) are released into the atmosphere due to the use of fossil fuels as raw materials. In the case of partial oxidation of hydrocarbons, the use of heavy oil or petroleum refinery residual oil as feedstocks cause the emission of carbon monoxide (CO) along with CO_2 . Similar products are also released in the case of coal gasification [14]. It should be highlighted that H_2 can be counted as a clean energy carrier only if it is directly generated by solar light, or indirectly via electricity from a renewable source (e.g. wind power or hydro power) [16].

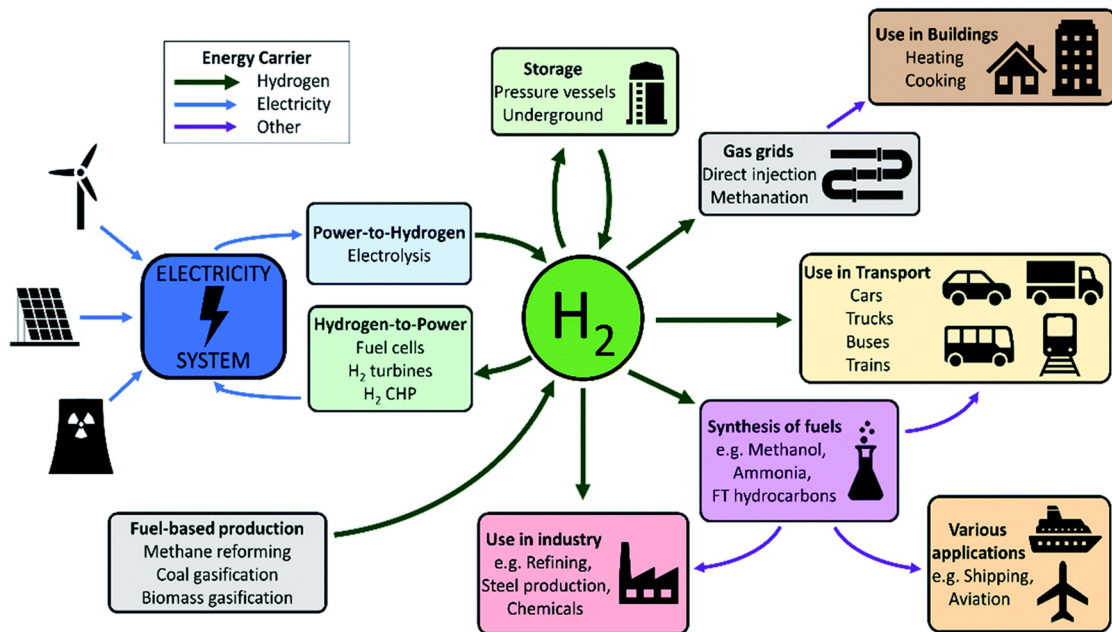


Figure 1.1: Overview of the different generation methods and applications of H_2 . Reproduced from [17].

Due to the disadvantages of conventional methods, the research on H_2 energy has shifted to its production from the renewable sources. Renewable sources can be listed as biomass, geothermal, wind, and solar energy; which are ideal candidates for replacing fossil fuels in the near future. Among renewable energy technologies, a huge research effort has been paid

for solar H₂ generation. Solar H₂ energy is considered as the most promising method of H₂ generation using a source of renewable energy due to its abundance and efficiency [18]. It can take place by splitting water via electrolysis, thermolysis, and direct photoconversion (including photocatalytic, photoelectrochemical, and photobiological generation), utilizing water as the only material input [19]. Here, we will focus on H₂ generation from water by photocatalysis in more detail, which has been a highly popular research topic lately.

1.2.1 Photocatalytic Hydrogen Evolution Reaction (HER) from Water

Photocatalytic water splitting to generate H₂ and O₂ has been of interest due to being a promising approach for eliminating the use of fossil fuels. It has drawn attention after the discovery of the activity of titanium dioxide (TiO₂) for UV light-induced water splitting by Fujishima and Honda in early 1970s [20]. In order to drive water splitting reaction, a “photocatalyst” which is active upon light illumination is needed. The two important characteristics of a photocatalyst are the width of the band gap, and the energetic positions of the conduction band (CB) and valence band (VB). The band gap energy of the photocatalyst defines the required energy to excite an electron from VB (highest occupied band) to CB (lowest unoccupied band). To promote this transfer, the energy of photons that excites the photocatalyst should be greater than or equal to band gap of the photocatalyst. For water splitting reaction, the bottom level of the CB (CB minimum, CBM) has to be more negative than the redox potential of H⁺/H₂ (0 V vs. NHE), while the top level of the VB (VB maximum, VBM) has to be more positive than the redox potential of O₂/H₂O (1.23 V) [21]. Therefore, the theoretical minimum band gap energy for water splitting is 1.23 eV [22, 23].

There are 3 major steps in photocatalytic water splitting: (i) absorption of photons by the photocatalyst to form electron–hole pairs, (ii) charge separation and migration of photogenerated carriers, and (iii) chemical reactions (redox reactions) to split water [22]. The schematic representation of water splitting is given in Figure 1.2. Each of these steps is equally important to achieve an efficient photocatalytic activity:

(i) A numerous semiconducting materials have been investigated as photocatalysts for water splitting; including d⁰ metal (e.g. Ti⁴⁺ and Zr⁴⁺) oxide photocatalysts, d¹⁰ metal (e.g. In³⁺ and Ga³⁺) oxide photocatalysts, f⁰ metal (e.g. Ce⁴⁺) oxide photocatalysts, and semiconductors free from metal species (e.g. black phosphorous and carbon nitride (C₃N₄)). However, the main bottleneck about these materials is that, they mostly present activity only under UV-light irradiation [23, 24]. The solar spectra is mainly composed of visible (43%) and infrared (53%) light, while the UV light only corresponds to 4% of it [25]. Therefore, it is important to design photocatalysts which can function under realistic solar spectra conditions. The bandgap energy of the photocatalyst should be < 3.0 eV (> 400 nm) to perform water splitting under

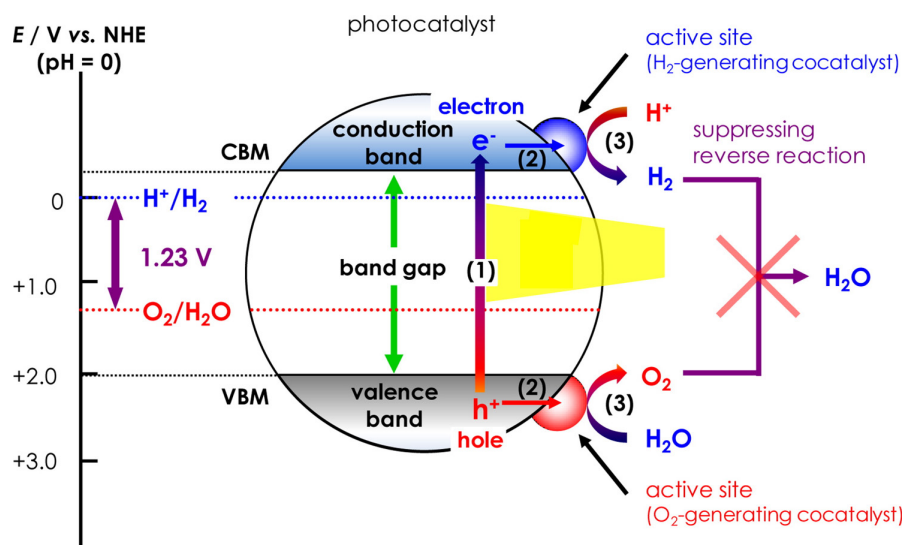


Figure 1.2: Schematic energy diagram of photocatalytic water splitting using a photocatalyst. Modified and reproduced with permission from [28].

visible-light [22]. Therefore, the identification of the electronic structure of a material is highly important to determine the densities of the relevant energy states [26].

(ii) The desired light absorption capability of the photocatalyst does not guarantee a good photocatalytic efficiency. The generated free charge carriers (electrons and holes) upon light illumination should be separated efficiently and they must travel through the photocatalyst to reach the redox active sites. The charge separation and recombination are competitive processes in photocatalysis. Therefore, the water-splitting redox reactions should be occurring within the lifetimes of photoexcited charges [27]. This step is highly affected by the crystal structure, the level of crystallinity, and particle size [22]. Moreover, the understanding of electronic structures of the photocatalysts is important to achieve the desired carrier separation and transport.

(iii) The electrons and holes should be trapped by the active sites and rapidly participate in the reactions with adsorbed species, to prevent the electron-hole recombination. It should be emphasized that the step (ii) and step (iii) are correlated to each other [27]. A highly common method to improve the efficiency of electron-hole separation is to introduce co-catalysts to the photocatalytic systems (e.g. Pt, Ru, or nickel phosphide (Ni_2P) nanoparticles (NPs)) as the active sites [22].

Although it is a highly desirable reaction, overall water splitting is challenging to achieve thermodynamically. This is mainly due to the Gibbs free energy value of the reaction ($237.13 \text{ kJ mol}^{-1}$), which means an energy input is required [29]. Overall water splitting involves two half-reactions: the oxidation of water to form O_2 and the reduction of protons to form H_2 .

While photocatalytic oxidation of water requires the coupling of 4 electrons, the reduction of water is less demanding and it only involves 2 electrons [30]. Therefore, oxidation of water is usually repressed by including sacrificial reagents in the photocatalytic reaction. The role of sacrificial reagent (i.e. electron donors or hole scavengers) is to be oxidized instead of water by the photogenerated holes when the electron is excited. By this way, a possible electron-hole recombination is eliminated and photocatalytic H_2 evolution reaction (HER) is promoted [22, 31]. Different sacrificial reagents (e.g. methanol, triethylamine (TEA), triethanolamine (TEOA), Na_2S/Na_2SO_3) have been applied in photocatalytic HER studies up to date [32, 33].

An extensive research has been performed on semiconductor materials (especially on metal oxides, such as TiO_2 and ZnO) as promising candidates for photocatalytic HER from water. However, their large band gaps ranging between 3.0-3.3 eV result in poor efficiency under the visible light conditions [34]. Therefore, it is important to design materials that can have visible-light-driven band gap excitation (< 3.0 eV), efficient electron-hole separation, high carrier mobility and photocatalytically active sites. With this aim, different approaches have been followed to enhance the photocatalytic HER performance of semiconductor materials; including anion/cation doping, coupling with other metal/semiconductor materials, and incorporating photosensitizers for better light utilization [23]. Recently, metal-organic frameworks (MOFs) have been suggested as promising and practical alternatives due to the combination of many advantageous characteristics in one porous network [34]. The promising features of MOFs for photocatalytic HER will be discussed in Chapter 2 in detail.

1.3 Storage of Hydrogen Energy

1.3.1 Challenges in Hydrogen Storage

Although a wide range of methods have been investigated for the production of H_2 , its storage still remains a challenging task to achieve. It is promising to store H_2 as an energy carrier and use in different technologies; including power generation, fuel cells, internal combustion engines, and turbines [2]. While liquid and compressed H_2 have the highest energy density of common fuels by weight, they have lower energy density by volume compared to that of gasoline (Table 1.1) [5]. Another concern is that, H_2 can explode violently when it is in contact with air. Therefore, its safe and efficient storage is of great importance for large-scale utilization of H_2 energy. The methods for H_2 storage have been under development for two systems: stationary applications and mobile applications. Stationary applications mainly cover the on-site H_2 storage and power generation, while mobile applications involve the transport of H_2 and its utilization in a vehicle as fuel [2]. Therefore, there are different requirements for each application.

The stationary storage systems are less restricted in terms of requirements compared to those of mobile storage systems. The weight and volume of H_2 are not the major concerns for stationary storage. These systems can occupy more space and can function at high temperatures and pressures. Nevertheless, different storage capacities by appropriate storage vessel are desired and the material used in the design of vessel is important [35]. Distinctively, mobile applications have many more requirements compared to those of stationary H_2 systems, due to the importance of “gravimetric” and “volumetric” capacities. While “gravimetric capacity” defines the quantity of H_2 gas that is stored at a given weight of storage material, “volumetric capacity” refers to the amount of H_2 gas contained in a specific volume of storage material [5]. For the mobile applications, there should be a balance between these two capacities in order to prevent any weight or volume restrictions in the vehicle. There are other important parameters for mobile storage systems, including: (i) low-operating pressure and temperature, assuring safe operating conditions, (ii) fast and efficient release of H_2 and its reversible storage, (iii) minimum energy loss during charge and discharge of H_2 , and (iv) resistance to oxygen and humidity for long cycles [2]. In order to meet aforementioned criteria for both systems, different H_2 storage methods have been extensively explored in the last decades.

1.3.2 Hydrogen Storage Methods

The H_2 storage technologies can be divided into two main groups as physical-based storage and material-based storage, as shown in Figure 1.3. These methods will be summarized in the following sections.

Physical Storage of Hydrogen

Currently, H_2 is mostly stored using physical-based methods, in which H_2 does not interact with the storage media. Physical-based storage can be performed either in “compressed” form of H_2 in high-pressure tanks (350-700 bar tank pressure), or in its “liquid” form in cryogenic tanks. At present, most of the fuel cell vehicles in the market use high-pressure cylinders to store H_2 on board [36]. However, compressed H_2 has safety issues due to the requirement of high pressure values for storage, which arises from the low density of H_2 . Another problem is the cycles of filling and consumption of the H_2 gas, which make the storage tank fatigued. Therefore, there are specific requirements for the design of the tanks [5]. In the case of liquid H_2 , the temperature should be kept below the boiling point of H_2 (20 K), which is energy demanding. Moreover, the evaporated H_2 gas should be released regularly in order to prevent the undesired pressure increase in the tank [5]. It should be highlighted that the volumetric energy densities of compressed and liquid H_2 are still not compatible with that of gasoline, in addition to their high costs and safety issues. Therefore, the research efforts have been shifted towards material-based storage in the last years.

Material-Based Storage of Hydrogen

All material-based storage methods involve the interaction of H₂ with the storage media, via strong covalent/ionic bonds or via weak van der Waals forces [37]. The main goal of material-based H₂ storage has been to find materials which can overcome the ultimate gravimetric (6.5 wt%) and volumetric density (50 g L⁻¹) targets determined by the Department of Energy (DOE) [38]. Material-based H₂ storage can be divided into two main groups as molecular storage and atomic storage.

Molecular storage is a process where H₂ molecules adsorb on the surface of the material through van der Waals bonding. Porous materials such as MOFs, carbon-based materials (fullerenes, nanotubes and graphene) and zeolites are the main candidates for the molecular storage of H₂ [37]. This approach can take advantage of the high surface area of the materials and the low binding energy of H₂ (promoting faster kinetics for the adsorption and desorption). However, it suffers from the weight of the carrier materials and the requirement of low temperature and high pressure to efficiently store H₂. For example, although MOFs are good sorbents at cryogenic temperatures and high pressures (as high as 9 wt.% at 56 bar and 77 K) their storage capacities diminish to ~ 1 wt.% at ambient conditions, which arises from the weak interaction (usually 4-12 kJ mol⁻¹) between H₂ molecules and the MOFs [39].

In atomic storage, H₂ molecules are coordinated in the chemical structure of the storage material. Atomic storage suggests stronger binding energy (50-100 kJ mol⁻¹) of H₂ molecules compared to that of molecular storage [40]. Therefore, the source material should be subjected to either thermal or catalytic decomposition to release the H₂ [41]. Atomic storage materials can be listed as solid storage media (e.g. metal hydrides and chemical hydrides) and liquid storage media (e.g. liquid organic hydrogen carriers (LOHC), alcohols, and formic acid) [41]. Among these methods, H₂ storage in chemical hydrides has drawn attention in the recent years since chemical hydrides are typically composed of lighter elements, leading to high H₂ density. In addition, they can release H₂ easily under relatively moderate operating conditions compared to those of metal hydrides, which can suffer from slow kinetics and uptake/release H₂ at a high temperature range [2]. Among chemical hydrides, boron- and nitrogen-based compounds, such as metal borohydrides, hydrazine borane, hydrazine, and ammonia borane (AB) have been increasingly investigated in the past years [42]. These materials are promising not only because of their high H₂ density but also thanks to their easy storage and transport without requiring harsh conditions. In Chapter 3, AB as one of the most promising chemical hydrides will be presented in detail.

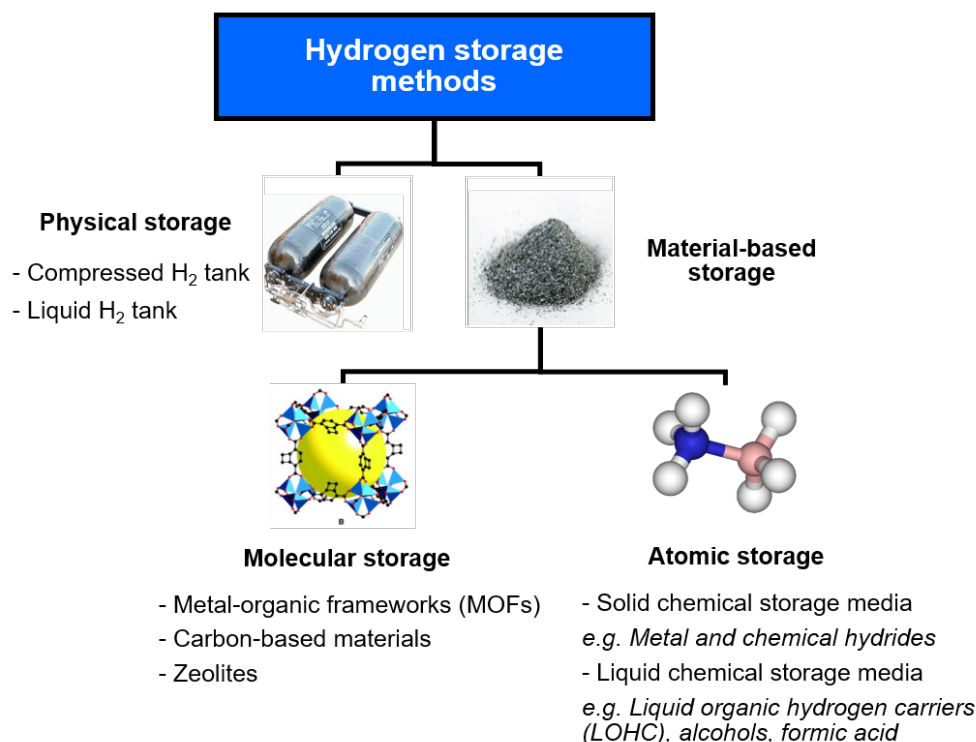


Figure 1.3: Summary of physical and material-based H₂ storage methods.

1.4 Catalytic Hydrogenation Reactions

Utilization of H₂ in different applications has been as significant as its production and storage. In majority of industries where H₂ is used as a reactant, hydrogenation takes place [43]. Hydrogenation can be defined as the reduction reaction, where H₂ is inserted to the target molecule. Catalysts are mostly required for the hydrogenation reactions, to realize the reaction or to enhance the reaction rate and selectivity. Hydrogenation reactions have been important for different processes; including saturation of liquid oils, Haber–Bosch process for ammonia synthesis, and Fischer–Tropsch process for hydrocarbon synthesis [44]. In addition, the hydrogenation of organic compounds in the presence of a catalyst has been of great importance not only for research purposes but also in the chemical and pharmaceutical industries. It should be emphasized that the conditions of hydrogenation reactions; including temperature, H₂ pressure, and solvent, are important due to their effects on reaction kinetics and product selectivity [45].

Hydrogenation has been performed mainly by gaseous H₂ in the industry. However, the main concerns of gaseous H₂ are its storage and transportation due to the chemical properties of H₂. Another problem is the low solubility of H₂ in most solvents, which causes the requirement of high pressure and high temperature, resulting in safety issues [46]. Therefore, different

alternatives which can eliminate the use of high-pressure storage equipment and challenges of H_2 activation dynamics have been investigated [47]. Lately, the supply of H_2 from chemical hydrides have been of interest as alternatives for gaseous H_2 . A tandem route that couples the dehydrogenation of chemical hydride with hydrogenation of target compounds has been found as an efficient strategy to boost the productivity of the reduction process remarkably [48, 49, 50, 51]. In Chapter 4, the use of AB as the H_2 source for one of the most important industrial hydrogenation reactions, hydrogenation of nitroarenes to anilines, will be discussed in detail.

1.5 Thesis Objectives and Organization

This thesis focuses on H_2 energy in different aspects; including its production from water, release from a storage medium, and utilization for important hydrogenation reactions. We focus on the generation of H_2 energy from water by photocatalysis, which is a renewable way and is highly important considering the need of today's world for cleaner energy production. Bearing in mind that the storage is as crucial as the generation of H_2 , we study the catalytic release of H_2 from a safe and efficient storage medium, AB. Then, we demonstrate that the H_2 storage medium can be utilized adequately for important industrial hydrogenation reactions. In all three cases, we aim to put the emphasis on the importance of the catalyst, since it plays a crucial role for both activity and sustainability.

In Chapter 2, we provide a brief summary about the importance of MOF characteristics for the efficient photocatalytic HER from water. We discuss the important parameters that can affect the efficiency of a MOF-photocatalyst; including metal-related properties (e.g. electronic structure and optical characteristics), as well as morphological features. We chose isostructural pyrene-based MOFs as our catalysts due to the favorable optical and electronic characteristics of pyrene molecule for photo-related applications.

In Chapter 3, we introduce an efficient and sustainable catalyst for releasing H_2 from its storage medium. Due to its advantageous storage features, AB was investigated as the H_2 storage material. The simultaneous *in-situ* release of H_2 from AB with the *in-situ* generation of active Cu^0 NPs from a copper-rich earth-abundant mineral are presented as an efficient approach for the most common deactivation problems of Cu^0 NPs.

In Chapter 4, we demonstrate the applicability of our approach that we present in Chapter 3 for hydrogenation of nitroarenes to their corresponding anilines. We discuss the advantages of *in-situ* generation of H_2 with the simultaneous *in-situ* generation of Cu^0 NPs during the hydrogenation reaction. We generalize our concept from most commonly studied nitroarene molecules to some complicated drug molecules.

2 Optimized Photocatalytic Hydrogen Generation with Pyrene-Based MOFs

2.1 Introduction

2.1.1 MOFs for Photocatalytic HER

MOFs are porous materials composed of metal-containing units connected by organic linkers, creating open crystalline frameworks with permanent porosity. Thanks to the possibility of combining different organic ligands with different metal ions/clusters, a numerous MOFs with high structural tunability, versatile porosity and internal surface features, as well as adjustable catalytic and optoelectronic properties can be synthesized [52]. In particular, MOFs suggest an ideal platform for photocatalytic applications due to their availability for photon absorption and catalytic activity. The photocatalytic activities of MOFs are originated from their semiconductor-like behaviors. Previous theoretical calculations showed that MOFs can have band gaps ranging from 1.0 eV to 5.5 eV by ligand functionalization, which shows that they can act as an insulating or semiconducting materials by tailoring the structure [53]. In addition, it was demonstrated that the band gaps of MOFs can be also tuned by altering the dimensions of the metal clusters involved in the structure [54]. These band gap values depend on the differences between the energy levels of VB and CB [53]. This indicates that the opto-electronic/catalytic properties of MOFs can be significantly altered by tuning the

This chapter is based on our manuscript in preparation: “**Kinik, F. P.**, Ortega-Guerrero, A., Ebrahim, F. M., Ireland, C. P., Kadioglu, O., Mace, A., Asgari, M., and Smit, B. Towards optimal photocatalytic hydrogen generation from water using pyrene-based metal-organic frameworks.” F. P. K. synthesized the MOFs, performed the photocatalysis and characterization experiments, analyzed the experimental data, and wrote the manuscript with the contribution from all authors. Calculations were performed by A. O. G and transient absorption spectroscopy data was collected by F. M. E. In addition, a part of introduction is based on our literature review “**Kinik, F. P.**, Ortega-Guerrero, A., Ongari, D., Ireland, C. P., Smit, B., 2021. Pyrene-based metal organic frameworks: from synthesis to applications. *Chemical Society Reviews*, 50, 3143-3177”.

structure of MOFs.

MOFs have exciting features that can be highly promising for photocatalytic HER from water [55]. The catalytic active sites (metal nodes/clusters) in MOFs are exposed and easily accessible for the reactants owing to the high porosity of the structures. Moreover, porosity promotes the efficient electron-hole separation by shortening the charge transfer path. Thanks to the high surface areas and well defined pore structures of MOFs, co-catalysts (e.g. noble and non-noble metal NPs) can be incorporated into the pores, to increase the efficiency of photogenerated electron-hole pairs and prolonging their lifetimes [55]. The light absorption spectra of MOFs can be tuned in a wide range, from UV to visible, in different ways: (i) by the careful selection of the ligand (e.g. chromophore molecules such as porphyrin and pyrene), (ii) by the functionalization of the ligand (e.g. the attachment of -OH and -NH₂ groups), and (iii) by the incorporation of photosensitizers (e.g. dyes) in the structure [55]. The promising features of MOFs for photocatalytic HER is summarized in Figure 2.1.

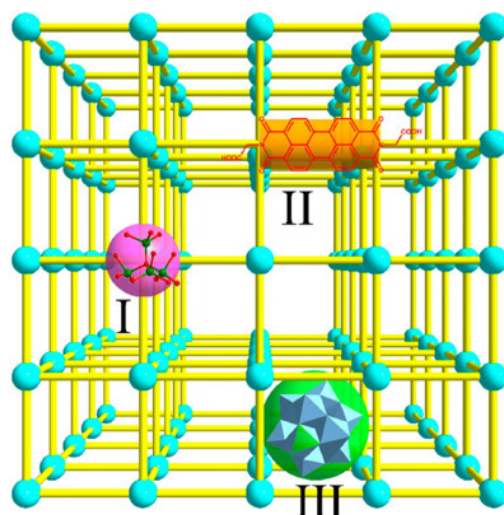


Figure 2.1: Schematic representation of the roles of catalytically active parts of MOFs in photocatalysis: (a) part I, inorganic cluster nodes including active metal centers, (b) part II, organic linker, acting as photon antenna to promote both light-harvesting and the electron transfer, and (c) part III, encapsulated guests in the porous structure (e.g. co-catalysts), which can enhance the lifetime of charge carriers. These three active sites are considered together to evaluate the electron transfer process in a MOF. Reproduced with permission from [56].

Depending on the combination of organic linker and metal node in the MOF, different photo-generated charge transfer mechanisms might occur upon light excitation, which is summarized in Figure 2.2 [57]. While designing MOFs for photocatalytic HER, enhancing the lifetime of the photo-generated charge carriers is important. Therefore, the use of metals having unoccupied states has been a popular approach to promote spatial charge separation. In this case, ligand-to-metal charge-transfer (LMCT) occurs when CB is localized in the organic ligand

[57]. Another possibility is metal-to-ligand charge-transfer (MLCT), where easily oxidizable metals are coordinated with reducible ligands. In both LMCT and MLCT, the recombination of photo-generated charges are expected to be prohibited since the charges are localized in either the ligand or the metal cluster of the MOF [57]. It should be highlighted that ligand-centered (LC) and metal-centered (MC) charge transfers are also observed in MOFs, which result in short and intense emission exploited in photoluminescence applications [57]. LC charge transfers have been studied in MOFs since π - π stacking interactions play an important role for promising electronic and optical properties [58]. Light-induced ligand-to-ligand charge transfer (LLCT) and metal-to-metal charge transfer (MMCT) are the other charge transfer mechanisms that have been reported in MOFs [57].

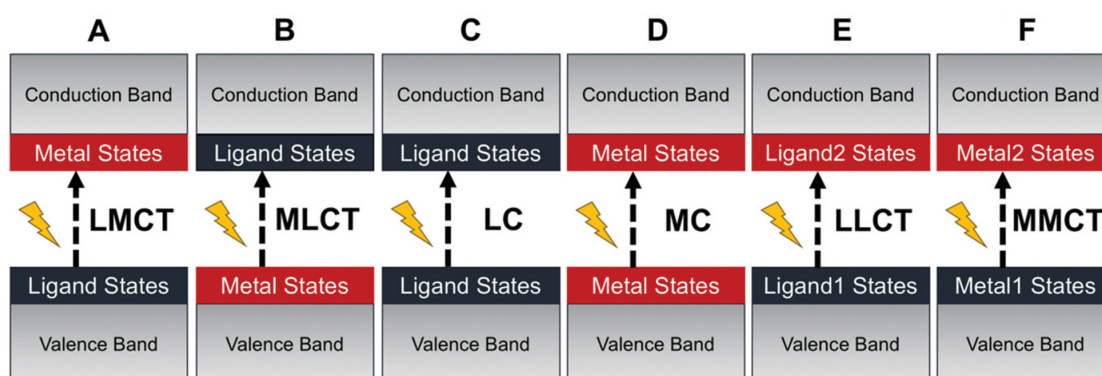


Figure 2.2: Possible photo-generated charge transfer mechanisms in MOFs: A) LMCT, B) MLCT, C) LC charge transfer, and D) MC charge transfer. In the structures having more than one ligand or metal, E) LLCT and F) MMCT charge transfers can be observed, respectively. In each charge transfer representations, black and red colors demonstrate ligand or metal states, respectively. In (E) and (F), black and red colors represent different ligands or different metals, respectively. Reproduced with permission from [57].

2.1.2 Pyrene-Based MOFs for Photocatalytic HER

A chromophore is a molecule which is capable of absorbing particular wavelengths of visible light, giving rise to some changes in electron density after the excitation process. Chromophore organic molecules have unique characteristics; such as high charge carrier mobility, light absorption, solution processability, thermal stability, and availability for the coordination with metal ions [59]. Among chromophoric materials, conjugated π -systems are perfect candidates for applications based on fluorescence, phosphorescence, or charge separation [60]. Pyrene is a highly symmetrical four-benzene-ringed polycyclic aromatic hydrocarbon, which is one of the most studied chromophore molecules after its discovery in the residue of the distillation of coal tar in 1837 [61]. After it became commercially available, the first use of pyrene was for the synthetic dye industry thanks to its intense yellow colour. With the discovery of its favorable properties as being a “fluorophore” with excellent emission properties, having long

excited-state lifetime, and successful electron hole-pair dissociation, pyrene has been one of the most investigated aromatic hydrocarbons [62].

Pyrene molecule allows the addition of different functional groups by traditional synthetic techniques such as formylation/acetylation, bromination, oxidation, and borylation reactions [59]. In this way, pyrene-based molecules have been used as substrates in the synthesis of molecules such as nanographenes and metal cages [63]. In addition, the optical properties of pyrene have been exploited in different materials such as organic light-emitter diodes (OLEDs) due to its emission characteristics, as well as organic photovoltaics (OPVs) and solar cells due to its absorption properties [59]. Owing to their promising optical and structural characteristics, pyrene-based molecules have attracted the researchers in the MOF field to be used as ligands. The interest in the design of pyrene-based MOFs has tremendously increased after the synthesis of some novel pyrene-based tetratopic ligands. An important milestone was the synthesis of 4,4',4'',4'''-(pyrene-1,3,6,8-tetrayl)tetrabenzoic acid (TBAPy) ligand, which was obtained using a standard Suzuki-Miyaura reaction between 1,3,6,8-tetrabromopyrene and (4-(ethoxycarbonyl)phenyl)boronic acid, to design a fluorescent-MOF to respond to small guest molecules [64]. TBAPy is a fluorescent ligand where the pyrene core is relatively rigid, and the benzoate groups substituted at the 1-, 3-, 6-, and 8-positions have a degree of rotational freedom (Figure 2.3). The carboxylate groups make this molecule attractive to link to the metal in a MOF. To date, different types of metals including alkali earth metals, transition metals, and post-transition metals have been coordinated with TBAPy ligand, resulting in 2D and 3D networks [65].

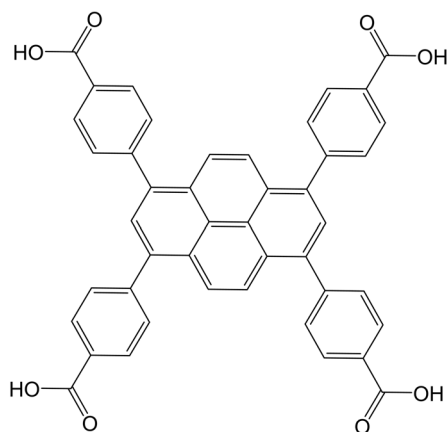


Figure 2.3: The structure of TBAPy ligand.

The optical characteristics of pyrene as a MOF-ligand gives pyrene-based MOFs some promising optical properties; including long-lived excited states, high fluorescence quantum yield, and the sensitivity of excitation spectra to micro-environmental changes [62]. The coordination of pyrene-based ligands with metal centers can give rise to new photophysical and

photochemical properties, which cannot be observed if the pyrene molecule is isolated [66]. These properties have been successfully incorporated in MOFs, which make them promising for luminescence and photocatalytic applications. The introduction of pyrene-based ligands into the MOF structure can enhance the electron transfer efficiency due to the strong π - π interactions between the pyrene and the reactant molecule, resulting in promising activity in catalytic applications. Consequently, pyrene-based MOFs are a growing field with published structures in the literature displaying an interesting rich topological, optical, and physicochemical properties covering a surprisingly large number of different applications.

The photo-sensitizing properties of pyrene-based MOFs have been exploited in promising energy applications like photocatalytic HER [67]. Theoretical and experimental studies have shown key features of photocatalytic systems like absorption [68], charge transfer [69, 70], and charge-separation [70, 71] present in pyrene-based MOFs. TBAPy linker has been combined with different metals such as Cd, Bi, and Ti which has led to materials with compelling photocatalytic HER properties. Cd-based pyrene MOF (Cd-TBAPy) is a 2D layer material exhibiting visible-light absorption around 600 nm and is capable of water reduction combined with Pt [72]. Although the MOF itself was not active toward photocatalytic HER, after loading Pt as co-catalyst, the HER rate could reach up to $86 \mu\text{mol g}^{-1} \text{h}^{-1}$. The Bi-based pyrene MOF (Bi-TBAPy) is another example of pyrene-based MOFs with good photocatalytic HER rate when combined with co-catalyst, where photocatalytic HER rate was $140 \mu\text{mol g}^{-1} \text{h}^{-1}$ in the presence of Pt [73]. Differently, Ti-based pyrene MOF (ACM-1) synthesized by Cadiau *et al.* [74] showed that pyrene-based MOFs can be also active for photocatalytic HER without the addition of co-catalyst. ACM-1 exhibits a typical LMCT leading to intrinsic charge separation confirmed by X-ray photoelectron spectroscopy (XPS) measurements and density functional theory (DFT) calculations. The optimal photocatalytic HER rate of ACM-1 was found to be $147.5 \mu\text{mol g}^{-1} \text{h}^{-1}$, which is more than those of Cd-TBAPy and Bi-TBAPy when they are combined with co-catalysts. Therefore, it is clear that there is still a large room for the investigation of pyrene-based MOFs for photocatalytic HER since the number of structures investigated for this application is still small, while the potential of these materials is really high due to their promising electronic and optical characteristics.

2.2 Toward Optimal Photocatalytic HER with Pyrene-Based MOFs

To design MOFs for photocatalytic HER from water, it is important to understand different factors that contribute to overall performance. Like any photocatalytic material, the HER photocatalytic activity of a MOF relies on having a material with adequate light absorption capability, optical band gap, and band alignment [75]. In addition, Guo *et al.* [76] demonstrated that different morphologies of the same MOFs can have strikingly different performances. Nasalevich *et al.* [77] showed that MOFs having different electronic properties perform dif-

ferently toward photocatalytic HER. However, the lack of a systematic study investigating all these affects together makes it difficult to compare the relative importance of these different factors.

In this chapter, we present a combined experimental and computational study on a family of pyrene-based isostructural MOFs. We believe that isostructural MOFs offer a good platform for this investigation, thanks to their similar crystal structures. We systematically investigate the different factors that contribute to the photocatalytic HER from water. In particular, we study: (i) the effect of metal coordinated in the MOF, causing differences in electronic and optical properties, and (ii) the effect of morphological characteristics. We show how these insights can be used to tune different factors that effective on the HER performance of MOFs, and generalized to other photocatalytic MOFs.

2.2.1 Synthesis and Characterization

For our study, we compared the performances of photocatalytic HER for a family of isostructural pyrene-based MOFs, which we refer to as “M-TBAPy” (M = Al, In, and Sc) (Figure 2.4(a)). AlPyrMOF [78] and ROD-7 [64] were synthesized using the procedures from the literature. In this work we refer to these two materials as Al-TBAPy and In-TBAPy, respectively. We synthesized the novel isostructural Sc version of the M-TBAPy MOFs, Sc-TBAPy, where TBAPy ligand and Sc^{3+} salt were reacted at 85 °C for 12 hours (for more details, see Appendix). The framework of Sc-TBAPy is based on chains of octahedral $\text{ScO}_4(\text{OH})_2$ units, where each Sc(III) is bound to four TBAPy ligands and two μ_2 trans hydroxide anions (Figure 2.4(a)). The comparison of experimental powder X-ray diffraction (PXRD) with the simulated pattern shows that for each of the three materials we obtained the desired structure (Figure 2.4(b)). Scanning electron microscopy (SEM) images revealed that, although the synthesis conditions for all three MOFs are the same (85 °C for 12 hours, in a mixture of DMF/dioxane/ H_2O), the metal has a pronounced effect on the crystal morphology. Sc-, Al-, and In-TBAPy form spherical crystals, circular discs, and intergrown rectangular plates, respectively (Figure 2.4(c)). The size of Al-TBAPy crystals is close to the Sc-TBAPy crystals, while the size of In-TBAPy crystals is an order of magnitude bigger. Cadiau *et al.* [74] reported the synthesis of the Ti version of M-TBAPy MOFs (ACM-1), which we refer to as Ti-TBAPy in our study. As the detailed HER experiments for Ti-TBAPy have been reported, we used the data from the reported study [74] in our comparison of the different properties. It should be highlighted that while Sc, Al and In have 3+ oxidation state in the M-TBAPy MOF structure, Ti has 4+ oxidation state. Therefore, there is a slight difference in the structure of Ti-TBAPy, being that the μ_2 -OH groups in Sc, Al and In-TBAPy are μ_2 -O in Ti-TBAPy to account for the 4+ oxidation state of Ti [74]. Despite the differences in the oxidation states, this family of M-TBAPy allows us to systematically study the effect of metal on the HER activity thanks to their isorecticular structures. In addition,

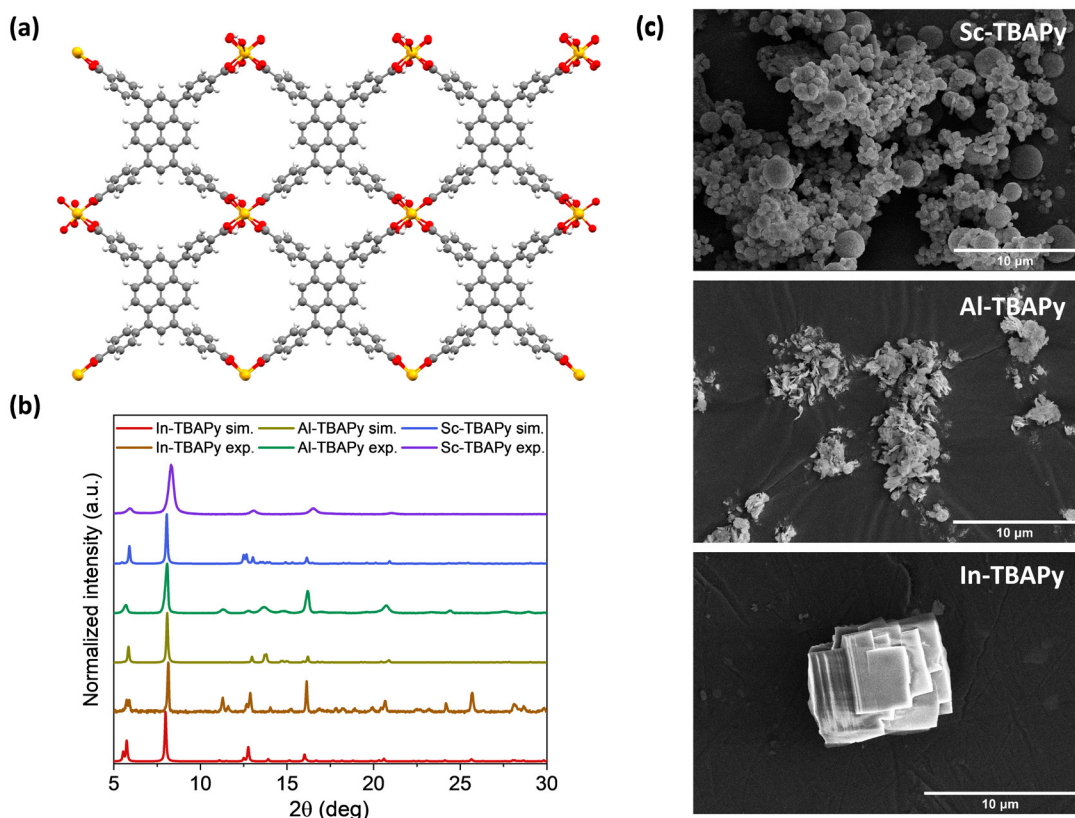


Figure 2.4: (a) Crystal structure of M-TBAPy (where M = Sc, Al, and In) MOFs. Color code: M: yellow, O: red, C: gray, H: white. (b) PXRD patterns of isostructural M-TBAPy MOFs, showing a good match between the individual experimental and simulated patterns. (c) SEM images of Sc-TBAPy (top), Al-TBAPy (middle) and In-TBAPy (bottom), demonstrating different structural characteristics of the MOFs.

we investigate in detail how the metal impacts the different factors that contribute to the photocatalytic HER, such as electronic structure and the optical characteristics of the MOF.

2.2.2 Photocatalytic Activity of M-TBAPy MOFs

The photocatalytic HER performances of Sc-, Al-, and In-TBAPy MOFs were investigated under visible-light irradiation using a 300W Xe lamp, with a 420 nm cut off filter to remove any UV light. Reactions were performed in the presence of TEA as the sacrificial reagent. The same conditions (17 mg MOF in 17 mL photocatalytic solution in a 25 mL reactor, 3 hours of reaction) were established for all MOFs for the comparability of the photocatalytic performances. Figure 2.5 shows that all three MOFs are capable of producing H_2 from water under specified conditions. The HER rates of In-TBAPy ($4.7 \mu\text{mol g}^{-1} \text{h}^{-1}$) and Al-TBAPy ($6.3 \mu\text{mol g}^{-1} \text{h}^{-1}$) are comparable, while Sc-TBAPy has a higher HER rate of $32.8 \mu\text{mol g}^{-1} \text{h}^{-1}$. The

HER rate of Sc-TBAPy was found to be less than that of Ti-TBAPy ($147.5 \mu\text{mol g}^{-1} \text{h}^{-1}$) [74]. Therefore, it can be envisioned that the differences in the photocatalytic HER performances are arising from different effects of different metals.

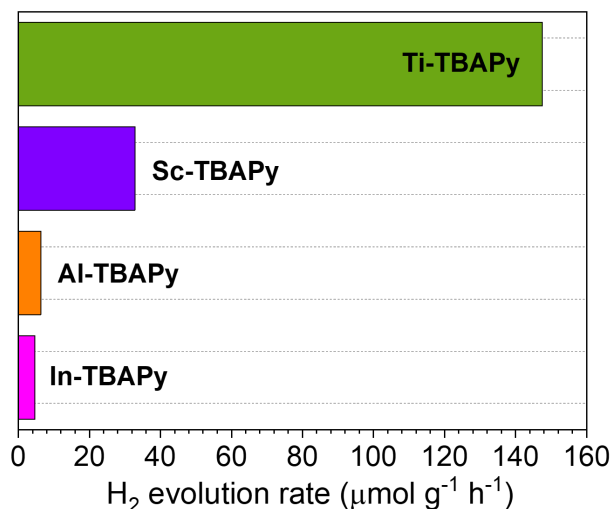


Figure 2.5: Photocatalytic HER rates of Sc-, Al- and In-TBAPy MOFs, under visible light irradiation ($\lambda \geq 420 \text{ nm}$, 3h reaction). Ti-TBAPy was included for comparison, where photocatalysis was conducted under visible light irradiation ($\lambda \geq 380 \text{ nm}$, data from Cadiau *et al.* [74]).

Investigation of Electronic Characteristics

There can be different factors that can explain the effect of the metal on the HER performance. One of these factors is the position of the band edges with respect to the redox potential of water. A thermodynamic requirement is the proper alignments of the band edges of the materials with the reduction and oxidation potential for water splitting, i.e., the CBM is above the H^+/H_2 reduction potential for HER and the VBM below the $\text{H}_2\text{O}/\text{O}_2$ oxidation potential for O_2 evolution reaction (OER). To analyze the positions of these band edges of the M-TBAPy MOFs ($\text{M} = \text{Al}, \text{In}, \text{Sc}, \text{and Ti}$), DFT calculations were carried out. In these calculations, the structures were optimized with the PBE0 functional using the *Cmmm* space group symmetry. Figure 2.6 shows that for all materials this requirement is fulfilled. The alignment of the VBM in Ti-TBAPy is lower than in the other materials despite their similarities, which can be associated to the difference in coordination of the $\mu_2\text{-OH}$ groups in Al-, In-, and Sc-TBAPy MOFs compared to $\mu_2\text{-O}$ in Ti-TBAPy [74].

Our DFT calculations also provide us the band structures of M-TBAPy MOFs. From the shape of the band structure, we can obtain some insights into the photoconductive properties and the mobility of the charge carriers. The curvature of the CBM and VBM will be related to the

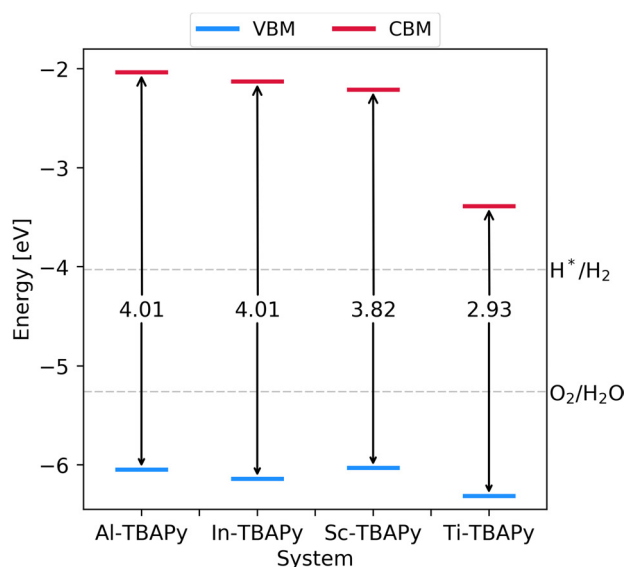


Figure 2.6: Energy diagrams of fundamental band gaps and the band edge positions with respect to the vacuum potential computed at the pore centre for Al-TBAPy, In-TBAPy, Sc-TBAPy, and Ti-TBAPy. The dashed lines are redox potentials of water splitting.

mobility of the photo-excited electrons and holes, respectively. The flatter the shape of the band, the higher the effective mass, and as a high effective mass gives a low charge mobility, such a flat shape can be associated with poor photoconductivity [79]. Figure 2.7 shows the band structure calculations of the different M-TBAPy MOFs together with a visualization of the CBM and VBM orbitals. All MOFs show a similar flat band for the VBM, but for the CBM we see the effect of the metals. For Al- and In-TBAPy the CBM orbitals are located on the pyrene core of the ligands, while for Sc- and Ti-TBAPy these are localized along the coordination complex, involving the metal and phenyl groups. For all four materials, the VB is the result of the contribution of pyrene π orbitals (Figure 2.7). The metals do impact the shape of the CB. Al-TBAPy and In-TBAPy have a flat band for the CBM and have the same band gap. For Al-TBAPy and In-TBAPy the VBM and CBM are both localized on the π and π^* pyrene orbitals of the TBAPy ligand, respectively [80]. As the band gaps for Al-TBAPy and In-TBAPy materials are dominated by the pyrene orbitals of the ligand, the calculation will predict the same values for band gaps. In contrast, Sc-TBAPy and Ti-TBAPy have a CBM placed below the pyrene orbitals, leading to smaller band gaps. Sc-TBAPy presents a slightly smaller band gap than Al- and In-TBAPy, since the CBM composed by orbitals of the Sc and phenyl groups is placed just below the pyrene orbitals (Figure 2.7(c)). The former are the ones associated with the one-dimensional Sc metal-rod like structure form in the topology of the M-TBAPy MOFs. Ti-TBAPy MOF has the smallest band gap of the four materials, since its CBM is localized only in the Ti d-orbitals and it has a more pronounced dispersion among the four materials (Figure 2.7(d)).

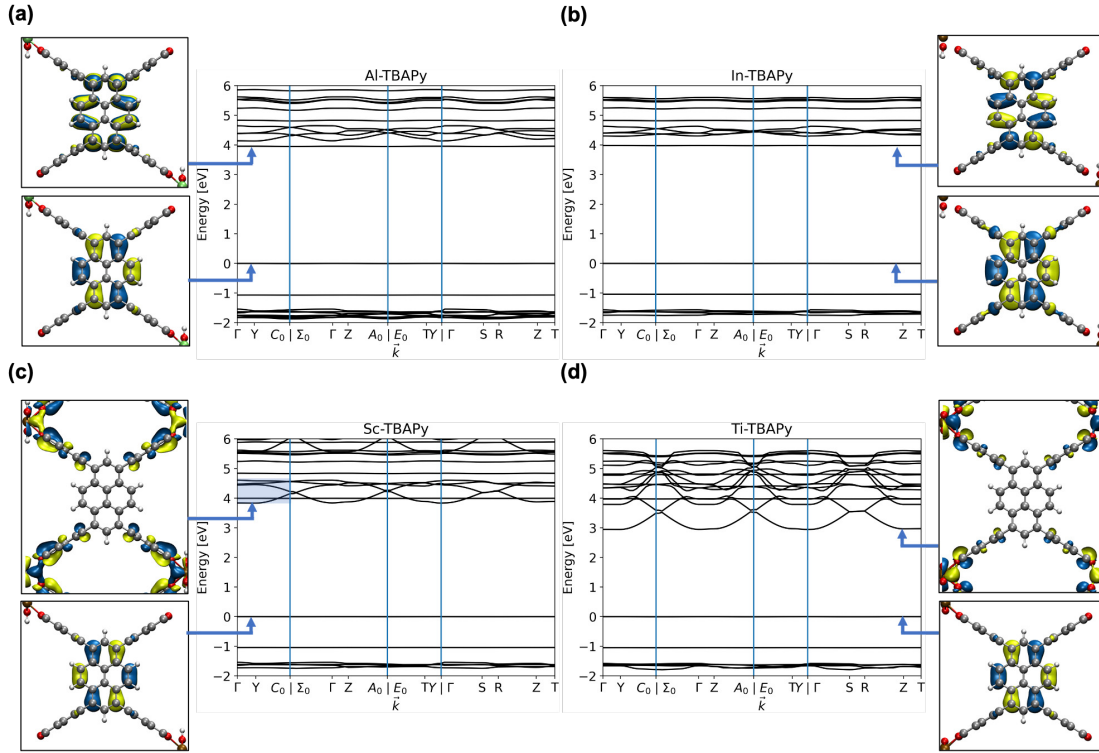


Figure 2.7: Band structure calculations and CBM and VBM crystal orbitals of the pyrene-based MOFs using PBE0 functional with $Cmmm$ space group (symmetrical structure). (a) Al-TBAPy, (b) In-TBAPy, (c) Sc-TBAPy, and (d) Ti-TBAPy. The blue square highlights the CB in Sc-TBAPy.

In this scenario, Ti-TBAPy (curved) band structure depicts a system with higher electron mobility among the four MOFs. In the case of Al-TBAPy and In-TBAPy, due to having a low dispersion (flat bands), and having carriers localized on the pyrene, carrier mobility is through a much slower hopping transport regime. In the case of Sc-TBAPy, in its bandstructure, the CBM presents less curvature than Ti-TBAPy, yet it suggests a better electron photoconductivity than its Al and In counterparts. CB of Sc-TBAPy suggests a better participation from the pyrene and the Sc metal-rod orbitals (i.e. π^* -orbitals of the benzoic acid fragment of the ligand and d-orbitals of Sc metal) in the mobility of the photogenerated electrons. However, the contribution of Sc orbitals in the CBM is small unlike the case of Ti-TBAPy, where the Ti d-orbitals present most of the contribution (Figure A.6(a), Appendix). The above depicts LMCT in the case of Ti-TBAPy as it was reported by Cadiau *et al.* [74].

Sc-TBAPy is particularly interesting from a theoretical point of view because of the proximity of the CBM to the orbitals of the pyrene ligand. This proximity makes the calculations very sensitive to the exact orientation of the phenyl groups in the ligands [81]. The optimized ground state structure of Sc-TBAPy is with high symmetry. We conducted vibrational frequencies calculation on Sc-TBAPy, where the vibrational mode of the phenyl rotations has a

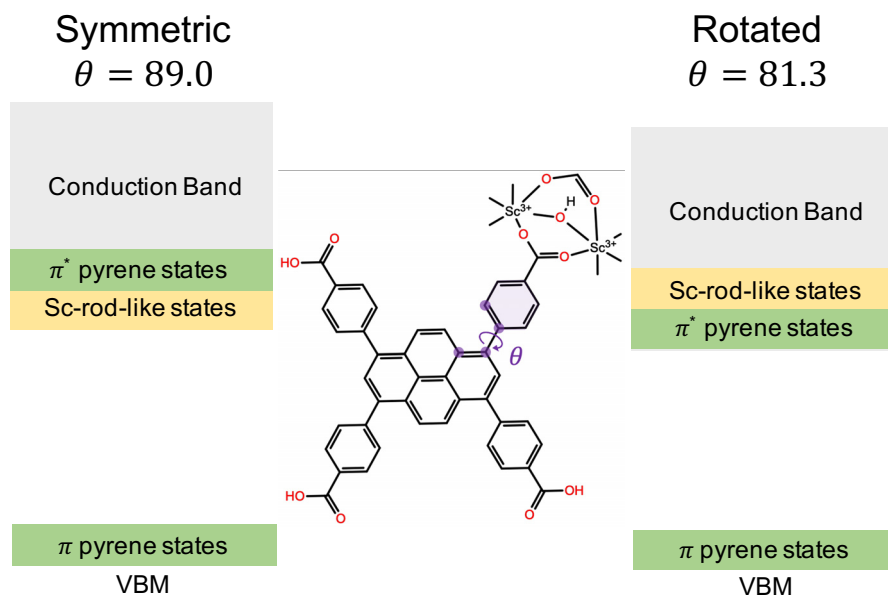


Figure 2.8: Representation of the different character of the VB and CB edges in Sc-TBAPy for the symmetric and rotated structures.

vibration temperature of 48.9 K. To investigate the effect of the rotation of the phenyl groups on the electronic structure, we conducted PBE0 geometrical relaxations calculation on all four M-TBAPys in both the symmetric and the rotated position of the phenyl rings. We refer to these as “symmetrical” and “rotated”, respectively. Sc-TBAPy has a local minimum, with an energy that is slightly higher than the ground state. In this local minimum, the phenyl groups have a rotation angle of 8° (Figure 2.8). The energy barrier between the ground state and this local minimum is relatively low (~ 3.35 meV). Therefore, it can be expected that because of the thermal fluctuations, the phenyl groups can be found in both orientations.

Figures 2.7 and A.7 (see Appendix) show the band structures of the symmetrical and rotated systems, respectively. For Al- and In-TBAPy systems, we see that the rotated case causes the CBM orbital to be at a lower energy. The rotation changes the localization of the pyrene core orbitals, causing the π^* -orbitals to move down, hence we see a small decrease in the band gap. As for Ti-TBAPy, the CBM is dominated by the orbitals on Ti, these rotations of the phenyl group have therefore little impact. In contrast, in the CBM of Sc-TBAPy, there are contributions from both the ligand as well as the metal orbitals. In the rotated case, the CBM is localized on the π^* orbital of the pyrene ligand and the Sc metal orbitals lies above, but in the symmetric case, this description was the opposite (Figure 2.8). This result suggests that the probability of Sc orbital states being occupied in the excited-states dynamics of the Sc-TBAPy system is higher than in the Al- and In- counterparts, given their proximity to the pyrene orbitals.

Table 2.1: Ground state E_{gs} and optical E_{opt} bandgaps including the nature of the E_{opt} transitions orbitals. The calculations are conducted using the symmetrical and phenyl rings rotated structures with PBE0 exchange-correlation functional.

System	Symmetric				Rotated			
	E_{gs} (eV)	E_{opt} (eV)	Orbitals	Transition ^a	E_{gs} (eV)	E_{opt} (eV)	Orbitals	Transition ^a
Al-TBAPy	4.01	3.40	$\pi \rightarrow \pi^*$	LC	3.76	3.18	$\pi \rightarrow \pi^*$	LC
In-TBAPy	4.01	3.41	$\pi \rightarrow \pi^*$	LC	3.72	3.14	$\pi \rightarrow \pi^*$	LC
Sc-TBAPy	3.82	3.40	$\pi \rightarrow \pi^*$	LC	3.77	3.21	$\pi \rightarrow \pi^*$	LC
Ti-TBAPy	2.93	2.86	$\pi \rightarrow d$	LMCT	2.94	2.82	$\pi \rightarrow d$	LMCT

^a LC stands for “Ligand-centered” transition and LMCT stands for “Ligand to Metal Charge Transfer”.

Since Sc-TBAPy CBM contains contributions from both the ligand as well from the Sc orbitals, it is important to establish whether the mechanism of charge transfer is LMCT, LC, or both. For this, we first computed the optical band gap (or the first optical excitation) of the four materials to establish the nature of the optical transition. For these calculations, we used linear-response time-dependent DFT (LR-TDDFT). Table 2.1 shows the values of the ground state and optical band gaps in both the symmetric and rotated cases. It can be seen that in Al-, In- and Sc-TBAPy MOFs the nature of the optical band gap is the $\pi - \pi^*$ optical transition. The rotated cases present smaller optical band gaps than the symmetric cases, keeping the same behavior as the one described before for the ground state band gaps. Although Sc-TBAPy has a CBM with a contribution of the Sc orbitals, the first optical transition is associated with a LC transition, despite the pyrene orbitals being higher in energy. Ortega *et al.* demonstrated that this is a result of the excitonic effects (originated from the electron–hole Coulombic interactions) [82]. On the other hand, Ti-TBAPy’s first excitation is from the pyrene to the Ti orbitals as it was reported as well by Cadiau *et al.* [74].

From our electronic structure calculations we can conclude that Sc-TBAPy and Ti-TBAPy coordination promote a better CBM dispersion. In the case of Ti-TBAPy, LMCT leads to beneficial electronic properties for HER than the ones with Al-TBAPy and In-TBAPy. Sc-TBAPy’s electronic properties are different from the other isorecticular M-TBAPy MOFs due to the presence of the ligand as well as the metal orbitals near the CBM, which leads to a better electron mobility compared to Al- and In-TBAPy.

Investigation of Optical Characteristics

For the photocatalytic activity it is important that the MOFs absorb light at the desired frequencies. The differences between the M-TBAPy MOFs in terms of their light absorption can be seen from the diffuse reflectance ultraviolet-visible (UV-Vis) spectra shown in Figure 2.9(a). The UV-Vis spectra of Al-TBAPy exhibits a broad light absorption ranging from 250 to 475 nm, with two main peaks at 278 and 350 nm. The absorbance maxima are red-shifted for

both In-TBAPy (375 nm) and Sc-TBAPy (415 nm) compared to that of Al-TBAPy at 350 nm. This result shows that Sc-TBAPy absorbs better in the visible light region than the other two MOFs, which contributes to its better HER rate. To determine the experimental optical band gaps, Tauc plots were generated based on the UV-Vis absorption spectra of M-TBAPy MOFs. Optical band gaps are found as 2.58, 2.68, and 2.63 eV for Sc-TBAPy, Al-TBAPy, and In-TBAPy, respectively (Figure 2.9(b)). The optical band gaps values obtained via LR-TDDFT are found to be higher than the experimental values (Table 2.1). It is noteworthy to mention that the experiments are performed at room temperature while our calculations are performed at 0 K. Our calculations do not consider the thermal effects and the quantum motion of the nuclei contributions on the band gap. The inclusion of these effects has shown a decrease in the calculated band gaps and better agreement with experiments [83].

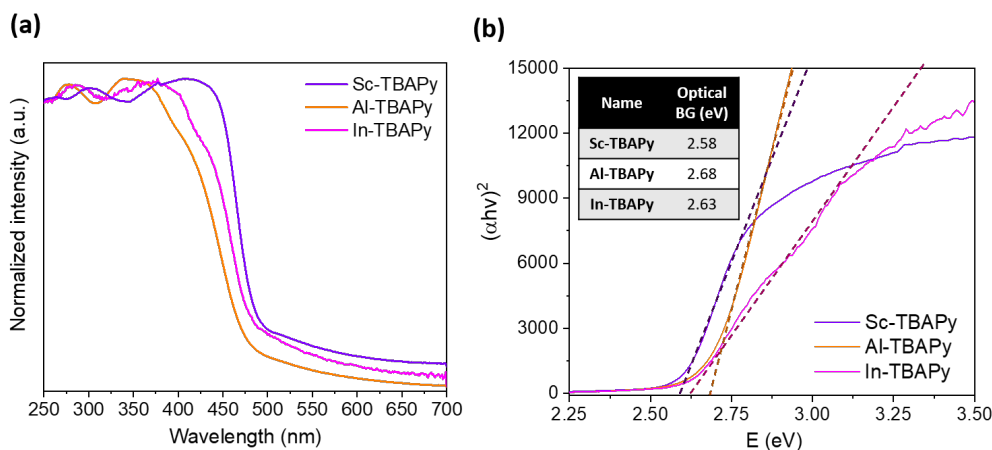


Figure 2.9: (a) UV-Vis spectra of M-TBAPy MOFs. (b) Tauc plots of M-TBAPy MOFs (inset: calculated optical band gaps of M-TBAPy MOFs).

Whereas the absorption spectra gives us information on which photons are absorbed, the apparent quantum yields (AQYs) gives us fraction of absorbed photons arriving on the sample that cause a chemical reaction to take place [84]. The AQYs of Al-TBAPy and Sc-TBAPy were measured by ferrioxalate actinometry at 400 and 450 nm, respectively (Table A.1, Appendix) [85]. While both MOFs showed similar AQY yields at 400 nm irradiation ($\sim 0.076\%$), Sc-TBAPy showed better AQY (0.364%) compared to that of Al-TBAPy (negligible) at 450 nm.

Another important quantity for the analysis of the efficient HER is the lifetime of the photo excited electrons. It is important that electrons in excited state should have long enough lifetime to perform the reduction of water and produce H_2 . We performed time-resolved photoluminescence measurements to record the duration of the decay of the photo excited electrons. The photoluminescence lifetimes of Sc-, Al-, and In-TBAPy show two decay features, with the longer lifetime (t_2) feature corresponding to the decay localized on the pyrene core, and the shorter lifetime (t_1) corresponding to the rotation of the phenyl rings [70]. Table A.2

shows that Sc-TBAPy has a shorter photoluminescence lifetime ($t_1 = 2.40$ and $t_2 = 11.70$ ns) than its Al-TBAPy ($t_1 = 2.72$ and $t_2 = 13.42$) and In-TBAPy ($t_1 = 2.84$ and $t_2 = 12.18$ ns) counterparts. The shorter lifetime of Sc-TBAPy can be attributed to the localization of the CBM around the phenyl rings and Sc rods rather than on the pyrene core, resulting in an overall shorter-lived excited state [70]. Due to the rigidity of the MOF structure the aggregation of the adjacent linkers is unlikely, therefore it can be excluded as a contributing factor to the lifetimes of the M-TBAPy MOFs. Moreover, the overall structures are quite stable since the rotations on the ligand only occur on the phenyl groups. Consequently, we do not expect to see any rearrangement among linkers. These results present an interesting example of the complexity of photocatalytic HER. If we would only consider the photoluminescence lifetime, one would conclude that those MOFs with the long photoluminescence lifetimes are those with an efficient charge separation and are thus often directly linked to better HER performance [74, 86, 87]. The case of Sc-TBAPy, however, demonstrates that different mechanisms can propose different explanations for lifetimes.

To gain further insights in the mechanism that causes these differences in photoluminescence lifetimes, we carried out nanosecond transient absorption spectroscopy (nTAS) analysis. nTAS is a pump-probe technique which is used to measure dynamic changes in the absorption of a photo-excited sample [88]. A broad-spectrum probe light illuminates the sample at nanosecond time intervals, before and after it has been photo-excited by a pump pulse. By plotting the difference in the sample's absorbance before and after photo-excitation as a function of wavelength and time, we gain insights into the dynamics of photo-excited charge carriers. For example, as molecules are promoted to the excited state through the pump pulse, the number of ground-state molecules decreases. Consequently, the ground-state absorption in the excited sample is less than that in the non-excited sample. This creates a negative signal in the absorption spectrum, which is known as ground state bleach (GSB) [88]. Figure 2.10(a-c) shows the GSB of M-TBAPy MOFs at the two absorption bands, around 300 nm and 500 nm. As expected, the shape of the GSB reflects the steady-state UV-Vis absorption spectra of the MOFs, with Sc-TBAPy exhibiting a broad single peak from 450 - 550 nm, and In- and Al-TBAPy exhibiting slightly blue-shifted peak maxima around 425 nm, and as well as a broad shoulder above 450 nm. The GSB recovery of the three MOFs matches their photoluminescence lifetimes, with Sc-TBAPy having the shortest recovery, followed by In-TBAPy and then Al-TBAPy.

A key characteristic of the In- and Al-TBAPy nTAS profiles, in particular, is the clear red-shifting of the principal 425 nm peak with time, indicated by the black arrows in Figure 2.10(b) and (c). Such a red-shift is typically indicative of non-radiative, vibrational losses, from the higher vibrational S_1 energy states to the CBM, that lower the energy of the excited state with time, and are typically seen in photoexcited pyrene [89, 90]. In the case of Al-TBAPy and In-TBAPy MOFs,

the transient red-shift can be seen over a longer timescale than what is typically observed due to vibrational decays [89]. This is likely due to inter-ligand interactions in the Al- and In-TBAPy MOFs. Since the CBM in both these structures is localized on the pyrene core, it is expected that electrons from adjacent pyrene cores will interact in the excited state, to form excimers [70, 91]. The decay of these excimers presumably adds a long lifetime component to the vibrational red-shift of the GSB. We can therefore conjecture that while localization of the CBM on the phenyl rings in Sc-TBAPy results in a shorter lifetime and a single prominent feature in its transient and steady-state absorption spectra, the distribution of charges around the pyrene core in In- and Al-TBAPy accounts for their longer excited-state lifetimes and the distinct vibrational features in their nTAS profiles.

Comparing the UV-Vis absorption of the three MOFs with their respective excitation spectra further supports the hypothesis that Al- and In-TBAPy suffer from more non-radiative, vibrational losses than Sc-TBAPy [70]. As seen in Figure 2.10(d-f), when probing the 500 nm emitting S_1 state, the excitation spectrum of Sc-TBAPy (shaded region) closely follows its UV-Vis absorption spectrum (solid line). This suggests that absorbed photons are efficiently populating on the S_1 excited state of the MOF. This is less evident in In- and Al-TBAPy, where a discrepancy between the absorption profiles and excitation spectra suggests that a portion of photoexcited electrons are undergoing vibrational decay.

Studies of pyrene suggest that the vibrationally unrelaxed state of pyrene molecules tends to be the active state for energy or charge transfer to a nearby acceptor [89, 92]. Therefore, the absence of vibrational features in the Sc-TBAPy spectra implies that its photoexcited electrons are maintained in a vibrationally unrelaxed state, where they are in an energetically favorable position for water reduction. The combination of enhanced absorption, spatial localization of the CBM, and efficient photoexcitation of the active excited state, all contribute to the superior performance of Sc-TBAPy as a photocatalyst. Our optical investigation thus highlights these three critical points: (i) LMCT is not a requisite for MOFs with high rates of HER, (ii) photoluminescence lifetime is not the only decisive parameter for photocatalytic HER and distribution of charges in the MOF structure should be also considered, and (iii) vibrational losses due to the localization of charges in the core of TBAPy may depopulate the active state for water reduction in photocatalytic active pyrene MOFs.

2.2.3 Investigation of Morphological Characteristics

Our findings showed that the combination of its electronic and optical characteristics made Sc-TBAPy favorable toward photocatalytic HER compared to its Al and In counterparts. Nonetheless, it should be kept in mind that the structural characteristics should not be neglected when exploring photocatalytic activity [76, 93]. Sc-TBAPy was selected as the case study and

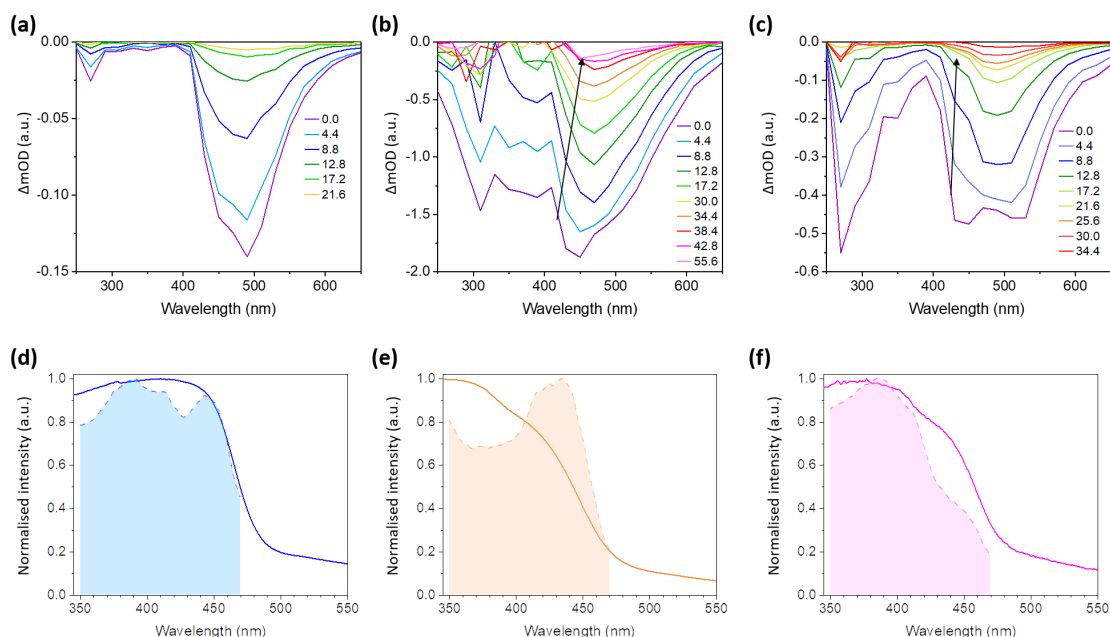


Figure 2.10: Upper panel: nTAS measurements of (a) Sc-TBAPy, (b) Al-TBAPy and (c) In-TBAPy (upon excitation at 420 nm). Lower panel: steady-state UV-Vis absorption spectra (solid lines) and excitation spectra (shaded regions) of (d) Sc-TBAPy, (e) Al-TBAPy, and (f) In-TBAPy.

different synthesis conditions were applied to obtain different morphologies.

A structure-capping surfactant (cetyltrimethylammonium bromide (CTAB)) was used during the syntheses, to allow the formation of different morphological characteristics [76]. When CTAB is added to the synthesis, the surfactant molecules are preferentially adsorbed on a specific facet of the crystal, and thus slowing down the growth of that surface by hindering the reactants to reach. Consequently, the final crystal morphology is determined by the slowest growing surface. It was observed that when the synthesis temperature was increased to 120 °C and the synthesis was performed for 72 h, the spherical particles of Sc-TBAPy were evolved to rectangular rods (named as “Sc-2”, Figure 2.11(a)). When the same synthesis condition for Sc-2 was performed in the absence of the acid modulator (HNO_3), smaller rectangular-shaped crystals were obtained (named as “Sc-3”, Figure 2.11(b)). Previous studies presented similar results that different acids (e.g. acetic acid, benzoic acid, or hydrofluoric acid) can act as “modulators” during the synthesis and alter the shape and/or size of MOF crystals [94, 95]. PXRD patterns showed that Sc-2 and Sc-3 have comparable patterns to that of Sc-TBAPy (Figure 2.11(c)). Light absorption characteristics of Sc-TBAPy samples were investigated by UV-Vis spectroscopy, demonstrating that all 3 materials have similar visible-light absorption (Figure A.5, Appendix).

Sc-2 and Sc-3 samples were investigated as photocatalysts for HER using the same photocat-

alytic conditions as mentioned before. Sc-3 presented the highest H_2 evolution rate ($82.5 \mu\text{mol g}^{-1} \text{h}^{-1}$), followed by Sc-2 ($60.6 \mu\text{mol g}^{-1} \text{h}^{-1}$) and Sc-TBAPy ($32.8 \mu\text{mol g}^{-1} \text{h}^{-1}$) (Figure 2.11(d)). Previous studies on different MOFs showed that the photocatalytic activity of MOFs can be directly related to their particle size [96, 97]. When the size of MOF particles gets smaller, the photocatalytic performance tends to enhance. This can be attributed to the fraction of catalytic sites on edges and corners which mainly determines the electron transfer efficiency. Smaller particles were found to have higher density of these sites [96, 98]. The shape and the facet of MOFs exposed to the catalysis is another important parameter [76, 93, 99]. Therefore, the better performance of Sc-3 might be attributed to the combination of its smallest size among all Sc-TBAPy MOFs, in addition to its exposed facet to the photocatalytic HER.

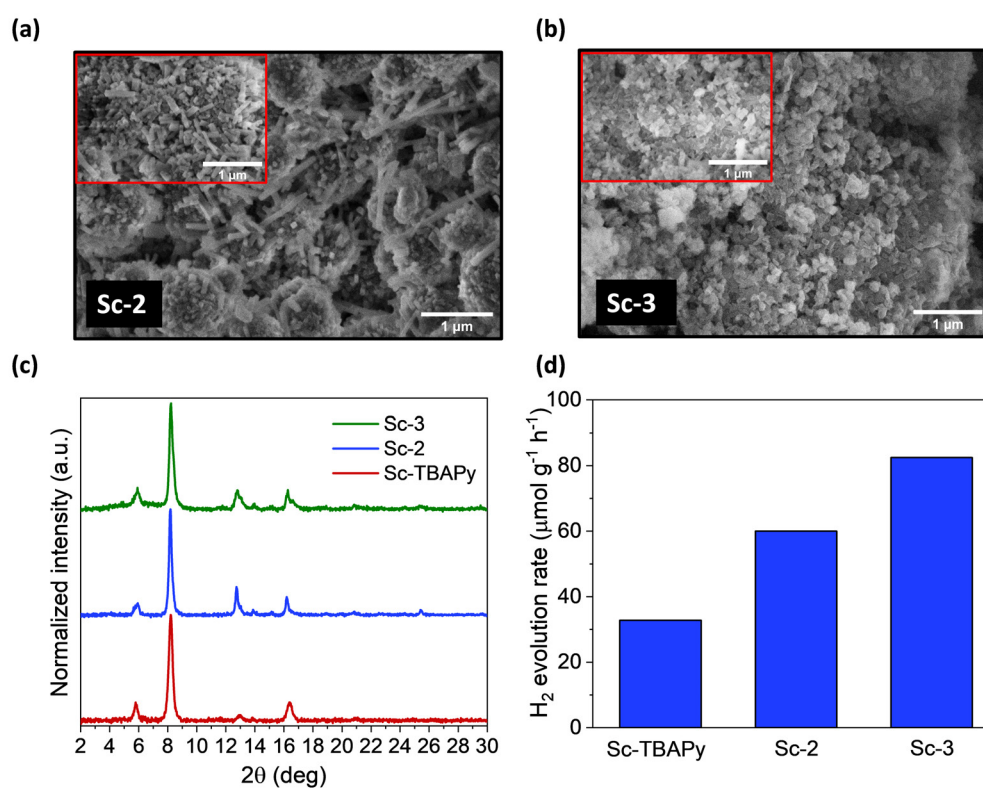


Figure 2.11: SEM images of (a) Sc-2 and (b) Sc-3 MOFs. (c) PXRD patterns of Sc-2 and Sc-3, showing that all 3 samples have the same crystallographical identity. (d) Photocatalytic HER rates of Sc-TBAPy, Sc-2 and Sc-3.

2.3 Summary and Conclusions

In this study, we investigated different aspects of photocatalytic HER by MOFs using the synergy between the computational calculations and experiments. We synthesized a new TBAPy-based MOF with Sc(III) metal centers, which is isostructural to previously reported

Chapter 2. Optimized Photocatalytic Hydrogen Generation with Pyrene-Based MOFs

Al-, In- and Ti-TBAPy MOFs. Our photocatalytic experiments demonstrated that Sc-TBAPy performs a better HER rate ($32.8 \mu\text{mol g}^{-1} \text{h}^{-1}$) compared to its Al and In counterparts (6.3 and $4.7 \mu\text{mol g}^{-1} \text{h}^{-1}$, respectively).

Our ab-initio calculations showed that there are some distinctions in the band alignments and band structures of M-TBAPy MOFs. Sc-rod orbitals are found to be located in the CBM in Sc-TBAPy, unlike the cases of its Al and In counterparts, where the CBM is localized on the pyrene orbitals. Interestingly, it was found that the vibrational rotations of the phenyl groups in TBAPy can modify the nature of the CBM in Sc-TBAPy. Our calculations showed that Sc and Ti metals promote a better electron dispersion around the CBM in the band structure.

Optical investigations demonstrated that Sc-TBAPy has an extended visible light absorption capability compared to Al- and In-TBAPy. nTAS measurements combined with the UV-Vis absorption and the respective excitation spectra of three M-TBAPy MOFs show that Al- and In-TBAPy suffer from more non-radiative, vibrational losses than Sc-TBAPy. The combination of enhanced light absorption, spatial localization of the CBM, and efficient photoexcitation of the active excited state contribute to the superior performance of Sc-TBAPy as a photocatalyst.

Along with the electronic and optical investigation, morphological characteristics of Sc-TBAPy were modified to optimize the photocatalytic HER performance. It was observed that with the optimized synthesis conditions of Sc-3, it is possible to increase the HER rate to $82.5 \mu\text{mol g}^{-1} \text{h}^{-1}$. This increase can be attributed to the size- and facet-dependent photocatalytic activity of MOFs as suggested in the previous studies.

Our study highlights that different chemical and structural factors come together and determine the photocatalytic performances of MOFs. Therefore, we believe that the future design of MOFs to create an ideal candidate for photocatalytic HER should consider all different criteria presented in this study together.

3 Hydrogen Release from Ammonia Borane by Cu-based Mineral

3.1 Introduction

3.1.1 Ammonia Borane as Hydrogen Storage Medium

The safe and efficient storage and release of H_2 are of great importance and still remain challenging tasks to achieve for large-scale utilization of H_2 energy as previously discussed. Among different chemical hydrides, boron-nitrogen-based (B-N) compounds, such as ammonia borane (AB, NH_3BH_3), have drawn attention due to their capability of storing and releasing significant quantities of H_2 [100]. AB, being the simplest B-N chemical hydride, is composed of nitrogen, hydrogen and boron. It was first prepared by Shore and Parry in 1955 as a white crystalline powder [101]. AB has high H_2 content (19.5 wt%), low molecular weight (30.9 g mol^{-1}), non-toxic nature, and enough thermal stability at ambient temperature to be transported and stored. The structural representation of AB is shown in Figure 3.1(a). It has particularly high stability in both aqueous solutions and air, making it more advantageous compared to the most B-N based compounds (e.g. hydrazine borane ($N_2H_4BH_3$)) or metal borohydrides (e.g. sodium borohydride ($NaBH_4$) and lithium borohydride ($LiBH_4$)), which suffer from self-hydrolysis in water [102]. AB exceeds many different storage systems in terms of H_2 capacity as shown in Figure 3.1(b); therefore, it is today a very promising boron hydride for H_2 -related applications.

The release of H_2 from AB can be achieved by either thermolysis or solvolysis; the latter can be

It should be noted that our publication “**Kinik, F. P.**, Nguyen, T. N., Oveisi, E., Valizadeh, B., Ebrahim, F. M., Gładysiak, A., Mensi, M. and Stylianou, K. C., 2019. Discovery of a self-healing catalyst for the hydrolytic dehydrogenation of ammonia borane. *Journal of Materials Chemistry A*, 7, 23830-23837” has been reused for this thesis chapter. F. P. K. synthesized the materials, designed and performed the experiments, analyzed the data, and wrote the manuscript with contribution from all authors.

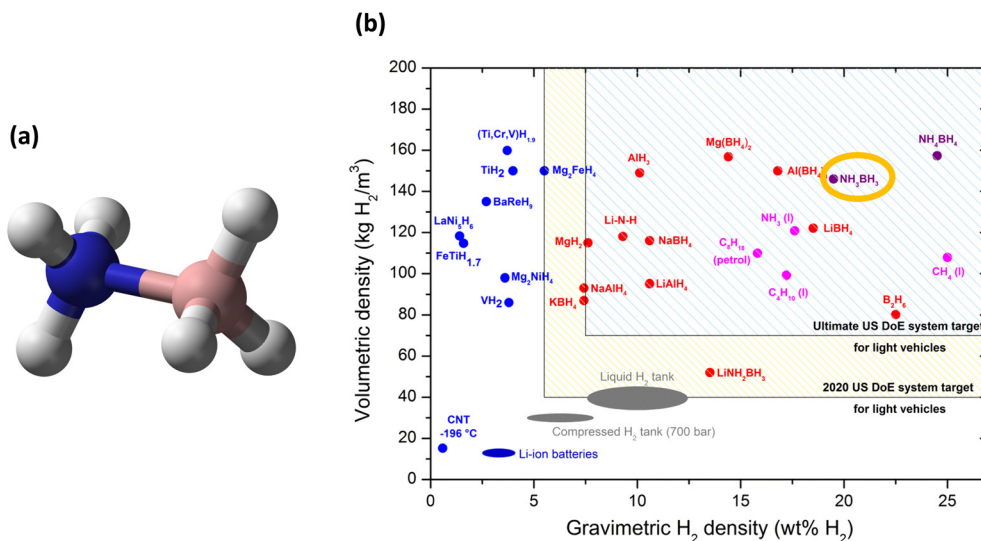
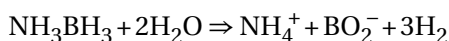


Figure 3.1: (a) Molecular structure of AB (color code: N: blue, B: light pink, H: grey). (b) Volumetric and gravimetric H₂ density of AB compared to some other H₂ storage materials, showing its potential to be used as storage medium. Reproduced from [103].

further classified into hydrolysis and methanolysis, in which the dehydrogenation reaction occurs in water or methanol, respectively. In thermolysis, high temperatures for the release of H₂ may be required or unwanted by-products such as borazine (B₃N₃H₆) might be produced during the dehydrogenation reaction [102]. In methanolysis, a lower H₂ capacity compared to other methods is obtained [104]. Hydrolysis is an attractive method for obtaining H₂ from AB because: (i) it can be performed at room temperature, (ii) it can proceed rapidly with various catalysts, and (iii) it can be controlled or stopped by means of removing catalyst from the solution [105]. Therefore, hydrolysis has been a benign method to obtain all 3 equivalents of H₂ from 1 equivalent of AB based on the following equation,



without the need of elevated temperature or toxic solvent, although a catalyst is often required [106]. Transition metals have been explored as catalysts for the hydrolysis of AB. It was demonstrated that the catalysis takes place on the metal catalyst surface. Due to the interaction between the NH₃BH₃ molecule and the catalyst surface, the active complexes are formed and the H₂O molecule attacks the B–N bonds to dissociate them. As a result, ammonium ion (NH₄⁺) and borate product (BO₂⁻) are formed along with the H₂ release [105]. The possible H₂ release mechanism from AB is demonstrated in Figure 3.2.

So far, the hydrolytic dehydrogenation of AB has been catalyzed by a wide range of catalysts;

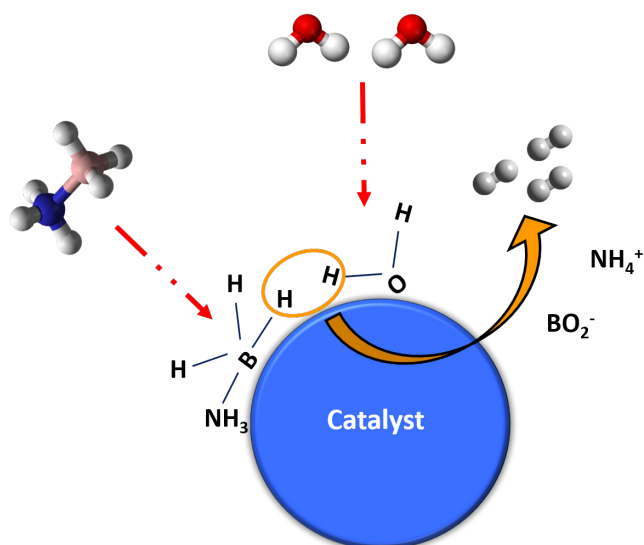


Figure 3.2: The plausible mechanism of AB hydrolysis on a catalyst. AB interacts with the surface of the catalyst to form an active complex, followed by its interaction with H₂O molecule, leading to the dissociation of the B–N bonds. At the end, ammonium (NH₄⁺) and borate (BO₂⁻) ions are produced along with the release of H₂. Color code: O: red, B: light pink, N: blue, H: light grey. H atoms are omitted for the clarity.

including: (i) monometallic noble metal NPs such as Ru [107], Rh [108], Pt [109], Ag [110], and Pd NPs [111], (ii) monometallic earth-abundant transition metal NPs such as Cu [112], Ni [113], Co [114], and Fe NPs [115], (iii) bimetallic/multimetallic NPs such as RuRh [116], RuCo [117], and RuCuCo NPs [118], (iv) NPs of transition metal oxides such as Cu₂O [119], (v) phosphides such as Ni₂P [120] and CoP [121], and (vi) transition metal complexes such as the iridium pincer complex [122].

3.1.2 Cu⁰ NPs for AB Hydrolysis: A Stability Issue to Consider

Cu⁰ NPs are reported to be among the most active catalysts for a wide range of catalytic reactions, including hydrogenations and dehydrogenations [45, 123], water-gas shift [124], organic transformations [125] and cross coupling [126], as well as photocatalytic reactions [127]. They are attractive catalysts not only because of their activity but also due to being earth-abundant and inexpensive. Despite the versatility of catalytic reactions with Cu⁰ NPs, their low stability has been a great challenge.

Cu⁰ NPs are prone to be deactivated due to many different mechanisms; such as sintering and aggregation, oxidation, deposition of reactants or products covering the surface, or poisoning of the catalyst. Many strategies have been developed to stabilize Cu⁰ NPs; such as the employment of capping agents (e.g., polymers and surfactants) [128, 129, 130] and supports (e.g.,

oxides, polymers and zeolites) [131, 132, 133], or the generation of core-shell structures with other metals (e.g., Ag, Ni, and Pd) [134, 135, 136]. These strategies, however, often only address one of the issues mentioned above and they are short term solutions. For example, using capping agents can effectively prevent the aggregation of Cu⁰ NPs; however, they can also act as “poison” and limit the accessibility of reactants to the catalytically active sites. Moreover, they can be detached from the NPs under some reaction conditions, which might have a detrimental effect on the stability of Cu⁰ NPs over several catalytic cycles [137]. In case of using supporting matrices, obtaining a uniform distribution of the Cu⁰ NPs is challenging, and the aggregation of NPs might still occur before or during the catalytic cycles [131, 132, 133]. Similarly, creating core-shell structures of Cu⁰ NPs with other metals might not prevent the catalytic deactivation [138].

Similar problems have been encountered when Cu⁰ NPs were used as catalysts for AB hydrolysis. Zahmakiran *et al.* [133] confined Cu⁰ NPs within the framework of Zeolite-Y for the hydrolysis of AB. The resulting material could release the H₂ completely (3.0 mol H₂/mol AB) within 2 h. However, zeolite confined Cu⁰ NPs could retain 53% of their initial catalytic activity at the 5th cycle of the reaction, which was attributed to their aggregation in zeolite framework. Wang *et al.* [139] synthesized Cu@MoCo core-shell catalyst to promote the catalytic activity of Cu toward AB hydrolysis. Although the core-shell catalyst performed a higher AB hydrolysis rate than most of reported Cu-based catalysts, its catalytic activity diminished to 60% and 40% of its initial rate at the end of 2nd and 4th cycles, respectively. The reasons were given as agglomeration of the catalyst, increase in the particle size, and surface oxidation during repeated experiments. A similar result was observed by Meng *et al.* [138] where the catalytic activity of graphene-supported trimetallic core-shell Cu@CoNi NPs was almost halved at the end of 5th cycle. These examples clearly show that different approaches applied for the protection of the activity of Cu⁰ NPs might remain insufficient.

Recyclability of the catalysts is highly important for practical applications since the long-term catalyst activity is vital for economic viability [140, 141]. The regeneration/replacement of the catalyst requires the shutdown of the process and the disruption of the production, which is highly costly for the industry [142]. Therefore, a fundamentally different strategy is needed to address the stability challenges that Cu⁰ NPs encounter. The “*in-situ*” regeneration of the catalysts counts as a highly desired property from economical point of view, and has been drawing attention by the researchers in heterogeneous catalysis field [143].

In this study, we explored an approach in which we aim to develop materials that can act as a reservoir for Cu⁰ NPs and generate them *in-situ* when needed. If these materials can be regenerated when the reaction cycle is over, Cu⁰ NPs can be formed freshly only when they are needed, which helps protecting them from deactivation mechanisms.

3.2 In-Situ Generation of Cu⁰ NPs for AB Hydrolysis

This chapter presents the catalytic activity of a naturally occurring copper-rich mineral toward H₂ release from AB by hydrolysis. Jacquesdietrichite mineral (which will be referred as to “synthetic mineral” in the following sections) with the chemical formula of Cu₂[(BO)(OH)₂](OH)₃ can generate Cu⁰ NPs *in-situ* as an integral part of the hydrolytic dehydrogenation of AB, which also acts as a reducing agent. In this section, firstly, the synthesis and characterization of the synthetic mineral will be explained. Then, its activity toward the hydrolytic dehydrogenation of AB and its capability for *in-situ* generation of Cu⁰ NPs will be demonstrated. Finally, we will discuss the efficiency of the regeneration of the synthetic mineral after each cycle, and propose that it can be a promising approach for efficient AB hydrolysis reaction without any deactivation of Cu⁰ NPs.

3.2.1 Synthesis and Characterization

Jacquesdietrichite mineral was discovered first in Morocco by the French geologist and mineralogist Jacques Emile Dietrich in 1999 [144]. The crystal structure of the mineral is given in Figure 3.3. The formation of the synthetic mineral was achieved by the reaction of as-synthesized Cu⁰ NPs with AB dissolved in water (see Appendix for details). For the synthesis, the AB solution with Cu⁰ NPs was exposed to open atmosphere and stirred gently overnight at room temperature under ambient conditions. Our hypothesis is that, since Cu⁰ NPs are active toward AB hydrolysis, first the dehydrogenation reaction occurs. Then, during overnight stirring, the Cu⁰ NPs are oxidized in solution under air, and combined with the BO₂⁻ ions in the reaction solution, forming the synthetic mineral. It was reported that Jacquesdietrichite mineral is the only known mineral containing BO(OH)₂⁻ group (named “dihydrogen borate” anion) and its structure is not closely related to that of any other known borate mineral [144]. The synthetic mineral can be obtained under ambient conditions in a large-scale without the need of high temperature or pressure. This synthetic advantage highlights the adequacy of the mineral for practical catalytic applications.

Powder X-ray diffraction (PXRD) analysis and Le Bail refinement revealed that synthetic mineral exhibits a pattern comparable to that of the Jacquesdietrichite mineral, with the chemical formula of Cu₂[(BO)(OH)₂](OH)₃ (Figure 3.4(a) and (b)). Mineral structure exhibited stability up to 250 °C without any change in the structural identity according to thermogravimetric analysis (TGA) and variable temperature PXRD analysis. (Figure A.9(a)-(b), Appendix). N₂ adsorption isotherm of synthetic mineral demonstrated that the material has a Brunauer–Emmett–Teller (BET) surface area of 39.24 m² g⁻¹ (Figure A.9(c), Appendix). The structural identity of synthetic mineral was further confirmed by Fourier transform infrared (FTIR) spectroscopy (Figure A.9(d), Appendix), by comparing the pattern of lab-synthesized

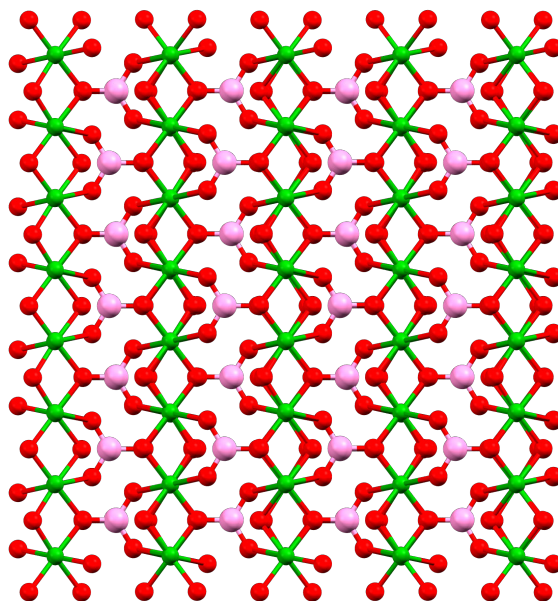


Figure 3.3: The structure of Jacquesdietrichite mineral [144] viewed along c-axis. CuO_6 octahedra are connected with triangular $\text{BO}(\text{OH})_2$ groups. Color code: Cu: green, O: red, B: light pink. H atoms are omitted for the clarity.

material with that of reported structure. Cu 2p XPS spectrum revealed that the bulk synthetic mineral powder consisted of mostly Cu(II) ions (> 95%), confirming that Cu^0 NPs used in the synthesis are almost quantitatively oxidized to form the synthetic mineral (Figure 3.4(c)). The SEM and TEM images collected on the synthetic mineral demonstrated the emergence of mineral consisting of cuboid shaped single crystals (Figure 3.4(d) and Figure A.10, Appendix). The concentrations of Cu and B obtained from inductively coupled plasma optical emission spectroscopy (ICP-OES) analysis matched well with the calculated concentrations from the molecular formula, proving the successful formation of synthetic mineral (Figure A.11, Appendix).

3.2.2 AB Hydrolysis

The synthetic mineral was investigated as a reservoir for *in-situ* generation of Cu^0 NPs with simultaneous AB hydrolysis. AB is not only a H_2 storage medium but also an efficient reducing agent, therefore it is expected to reduce the mineral structure to Cu^0 NPs. To optimize the amount of synthetic mineral for this reaction, different molar ratios of mineral/AB were tested by changing the amount of synthetic mineral while the AB amount (0.1944 mmol) was kept constant (Figure 3.5). For the best performance mixture with the molar ratio of mineral/AB = 0.27 (where synthetic mineral = 0.052 mmol), ~3 equivalents of H_2 were obtained after

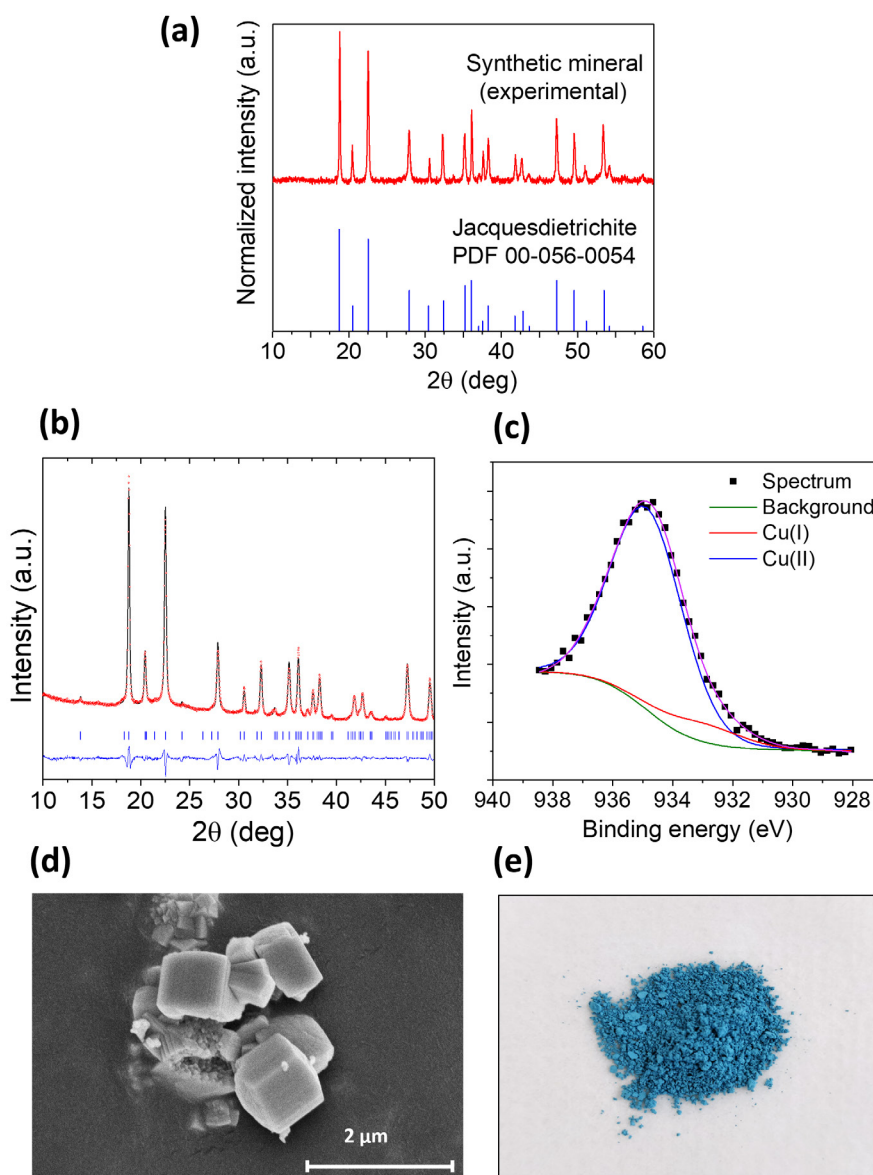


Figure 3.4: (a) Comparison of the simulated PXRD pattern of Jacquesdietrichite with the experimental PXRD pattern of the synthetic mineral. (b) Le Bail refinement of synthetic mineral: space group *Pnma*: $R_p = 4.73\%$, $R_{wp} = 6.07\%$, $a = 9.4607(7) \text{ \AA}$, $b = 5.8514(3) \text{ \AA}$, $c = 8.7001(6) \text{ \AA}$; $\lambda = 1.54187 \text{ \AA}$ (experimental data: red dots, refined Le Bail profiles: solid black lines, and difference between them: solid blue line). (c) Cu 2p XPS spectrum of as-synthesized mineral, revealing that the majority of the structure consists of Cu(II) ions. (d) SEM image of the synthetic mineral, demonstrating the formation of cuboid crystals. (e) The blue powder of the as-synthesized synthetic mineral.

45 minutes of reaction at 25 °C, giving a turnover frequency (TOF) of 1.85 min^{-1} (with a H₂ generation rate of $463.2 \text{ mmol gcat}^{-1} \text{ h}^{-1}$ at < 20% conversion). These values are higher than those reported for other Cu-based catalysts (used with no support); such as the commercial

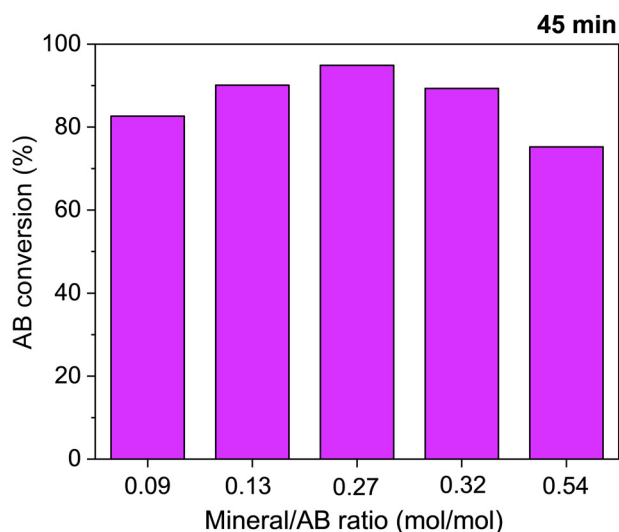


Figure 3.5: Optimization of the amount of synthetic mineral toward AB hydrolysis. The optimized amount ($\text{mol}_{\text{mineral}}/\text{mol}_{\text{AB}} = 0.27$) is used for all reactions performed in this study.

Cu^0 NPs (0.06 min^{-1}) [145] and Cu_2O (0.18 min^{-1}) [145], and some Cu-based catalysts grown or deposited on supports such as $\text{Cu}^0/\gamma\text{-Al}_2\text{O}_3$ (0.27 min^{-1}) [146] (Table A.3, Appendix).

During the AB hydrolysis, it was observed that synthetic mineral changed color and turned into a brown/black powder with time. After the reaction, the powder was collected and PXRD analysis was performed. Figure 3.6(a) suggests that the majority of Cu(II) ions in synthetic mineral were reduced to Cu^0 NPs, which means that *in-situ* generation of Cu^0 NPs from the synthetic mineral occurred. To confirm that, XPS data was collected on *in-situ* generated Cu^0 NPs after the hydrolysis reaction (Figure 3.6(b)). XPS data show two components with binding energies at 932.5 and 934.5 eV corresponding to the Cu 2p_{3/2} core level, which can be assigned to Cu(0) and/or Cu(I) (932.5 eV), and Cu(II) (934.5 eV), respectively [147]. The observation of Cu(I) and Cu(II) is expected because of the surface oxidation of Cu^0 NPs due to the exposure of sample to air during the sample preparation. XPS analysis also showed no noticeable B peak in the B 1s spectrum of Cu^0 NPs (Figure 3.6(c)).

Based on the observations explained above, the AB hydrolysis mechanism by the use of synthetic mineral can be summarized as follows:

- (1) The synthetic mineral is used for the *in-situ* generation of Cu^0 NPs in water. Upon the reduction by AB (which is a reducing agent), Cu^0 NPs are generated.
- (2) AB is also used as the storage medium for H_2 .
- (3) Therefore, the hydrolytic dehydrogenation of AB is catalyzed by *in-situ* generated Cu^0 NPs simultaneously, and hydrogen is released into the reaction solution.

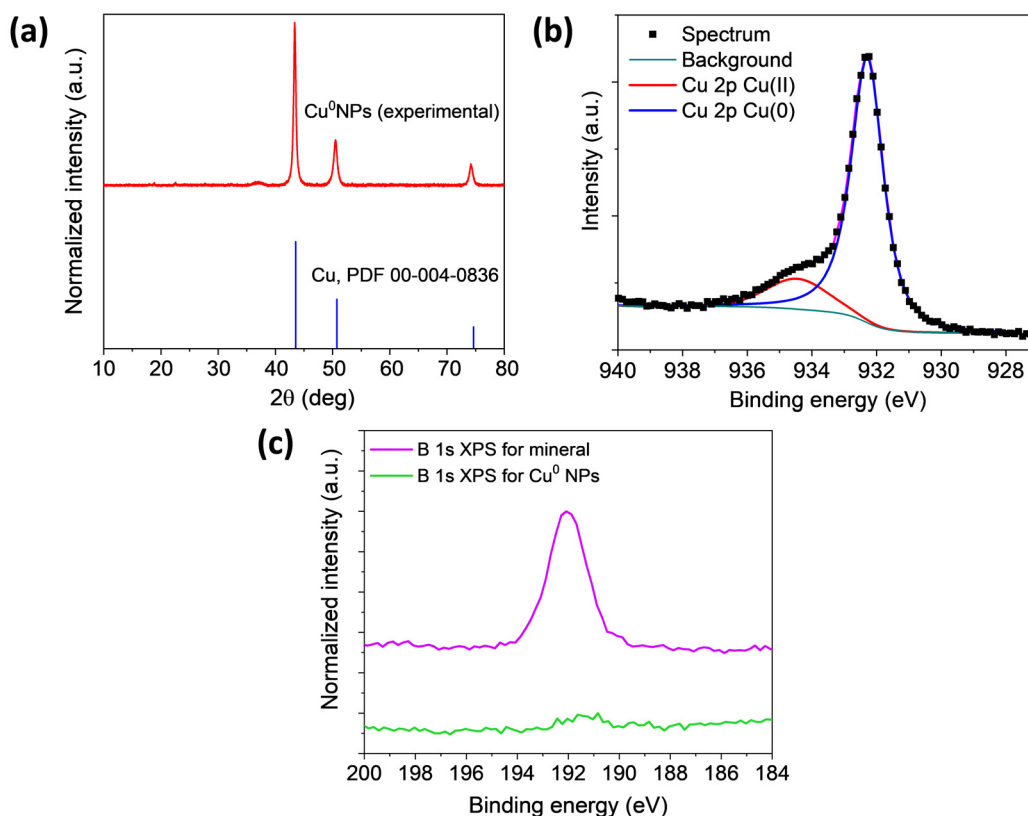


Figure 3.6: (a) Comparison of the simulated PXRD pattern of Cu⁰ NPs, with the PXRD pattern of *in-situ* generated Cu⁰ NPs collected after the dehydrogenation reaction. (b) Cu 2p XPS spectra of *in-situ* generated Cu⁰ NPs. (c) B 1s XPS peaks for as-synthesized mineral (purple) and Cu⁰ NPs derived from the synthetic mineral during AB hydrolysis (green).

The *in-situ* evolution of Cu⁰ NPs is demonstrated in Figure 3.7. With the curiosity of exploring the regenerability of the synthetic mineral, *in-situ* generated Cu⁰ NPs were remained in the catalytic reaction solution overnight and exposed in air under stirring, at room temperature. At the end of overnight stirring, the blue powder was recovered, and Cu-based synthetic mineral was re-formed as proved by PXRD in a quantitative yield (Figure 3.8(a)). This observation suggests that the fresh synthetic mineral can be continuously regenerated after the end of each cycle. The newly obtained synthetic mineral exhibited the same catalytic activity toward the hydrolytic dehydrogenation of AB. In fact, 10 cycles of AB hydrolysis (each cycle is for 45 mins) and synthetic mineral regeneration were performed, and the structural identity and catalytic activity of the synthetic mineral remained unchanged (Figure 3.8(b)). The small differences in AB conversions between the cycles might be arising from the instrument and human errors since the injection of H₂ into the gas chromatography (GC) was manually performed.

ICP-OES analysis confirmed that negligible amount of Cu(II) (0.0017 mol per mol of synthetic

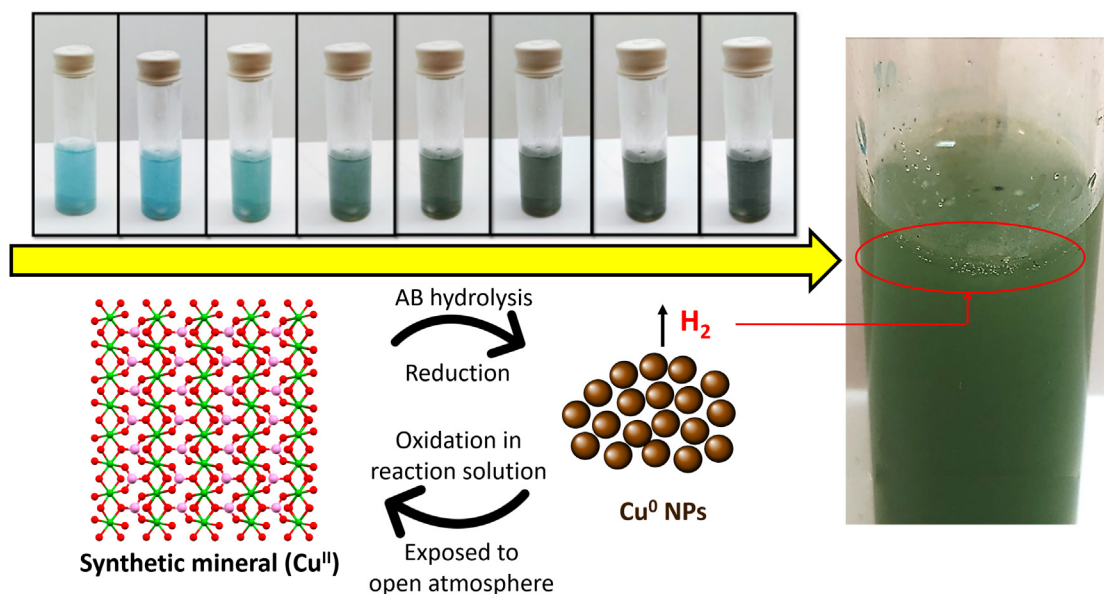


Figure 3.7: Schematic representation of the AB hydrolysis reaction: start – synthetic mineral (blue solution) and end – Cu^0 NPs (brown/black solution) of the reaction. The enlarged image shows the production of H_2 bubbles by the Cu^0 NPs.

mineral) is lost into the solution during the regeneration (Figure 3.8(c)), which corresponds to 95.75% regeneration after 50 cycles. The catalyst can be used and regenerated for many cycles without losing performance and material; this is a key characteristic for large-scale processes where the main issue lies in catalyst deactivation over time. After the regeneration of synthetic mineral from Cu^0 NPs, which occurs at the end of the cycle, the same solution can be kept and fresh AB solution can be fed to restart the hydrolysis. This can eliminate the solid-liquid separation and any “off” period during the reaction. The reformation of synthetic mineral also provides an easy handling of the active catalyst – Cu^0 NPs, since their oxidation under open atmosphere can be eliminated without using any capping agent or support materials. Our Cu-based synthetic mineral is regenerated in air without the need of any extra energy input.

We additionally studied the kinetics of the hydrolysis reaction varying the amount of AB while the amount of synthetic mineral was kept constant (optimized amount, 12.5 mg). The observed sigmoidal kinetic curves are characteristic of a pre-catalyst turning into the active catalyst: from synthetic mineral to Cu^0 NPs (Figure A.12(a) and (b), Appendix). The H_2 evolution rate was then calculated and showed 0.62- and 0.70-order dependences as a function of AB and synthetic mineral concentrations, respectively. The hydrolysis reaction with respect to AB concentration does not follow the zero-order kinetics, which might be attributed to the competitive interaction between water and AB molecules with the catalyst surface [148, 149]. The temperature dependence (298-318 K) of the AB hydrolysis was also studied in order to determine the activation energy (E_a) of the reaction. E_a is the minimum amount of energy

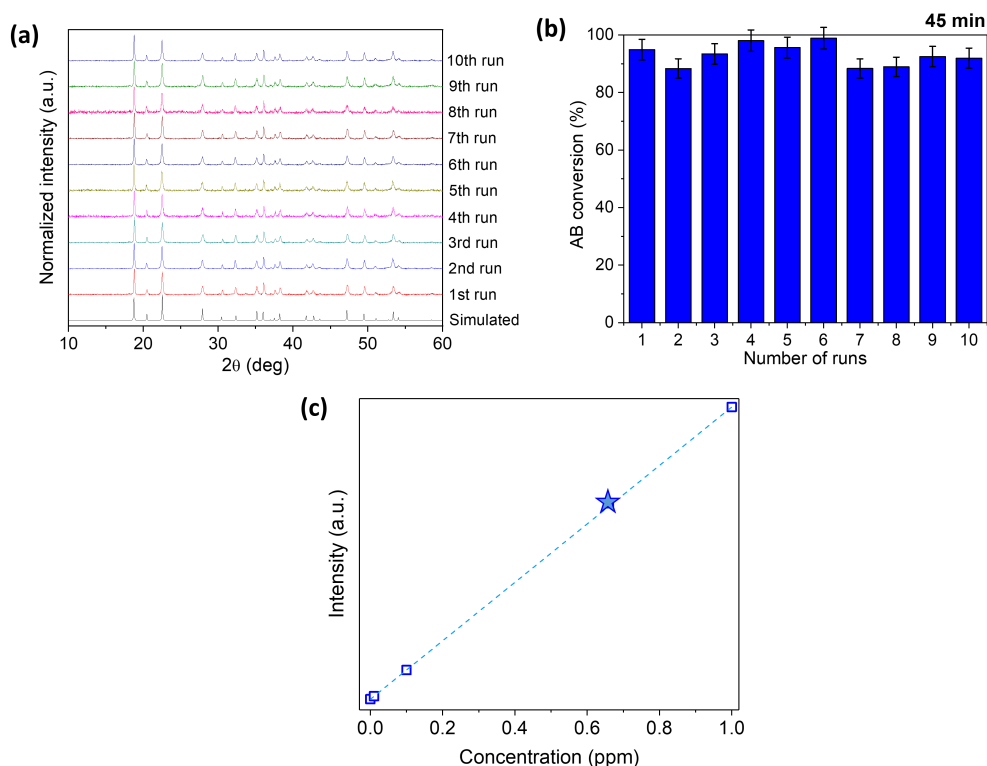


Figure 3.8: (a) PXRD patterns of synthetic mineral collected after each AB hydrolysis cycle, showing the stability of the catalyst during the regeneration process. (b) Reusability of synthetic mineral for the hydrolysis of AB for at least 10 cycles. (c) ICP-OES analysis of the negligible amount of Cu lost in the solution during the regeneration of synthetic mineral.

that is required for a chemical reaction to occur and the use of a catalyst is expected to reduce this energy. For determining E_a , the values of the rate constant k at different temperatures were calculated from the slope of the nearly linear part of each plot (Figure A.12(c), Appendix). From the Arrhenius plot (Figure A.12(c), Appendix), the activation energy for the hydrolytic dehydrogenation of AB was calculated to be 22.3 kJ mol^{-1} , which is lower than most of Cu-based catalysts for AB hydrolysis, including noble catalysts such as RuCu/graphene (30.4 kJ mol^{-1}) [150], and supported catalysts such as Cu@SiO₂ (36 kJ mol^{-1}) [151] and Cu/RGO (38.2 kJ mol^{-1}) [152]. It can be concluded that *in-situ* generated Cu⁰ NPs require less energy to reach the transition state compared to other Cu-based catalysts. This can be observed by the completion of reaction at shorter times even with a slight increase in the temperature.

3.3 Summary and Conclusions

Metal NPs, which are active species for catalytic reactions, tend to lose their activity with time due to different deactivation mechanisms. Due to the limited lifetime of the catalysts, the regeneration is required at some point of the catalytic cycles. However, this might require the

interruption of the industrial process and result in high expenses. Therefore, new approaches should be considered for the longer life time of the catalysts. In this chapter, we summarized our attempts for the *in-situ* generation of Cu⁰ NPs, which are active catalysts for the H₂ release from AB. AB has been suggested as a promising H₂ storage medium due to its high gravimetric and volumetric density of H₂. We demonstrated that the synthetic version of Jacquesdietrichite mineral can efficiently release ~ 3 equivalents of H₂ from 1 equivalent of AB thanks to the simultaneous *in-situ* generation of Cu⁰ NPs. The mineral can be easily synthesized at ambient conditions, can be efficiently regenerated, and the H₂ release activity is not decreased or disabled for at least 10 cycles of reaction. We propose that the mineral acts as a reservoir for Cu⁰ NPs; therefore, Cu⁰ NPs can be freshly generated during the reaction. When the reaction is over, Cu can be stored within the mineral structure without any deactivation problem until the next cycle.

The investigation of synthetic mineral introduces a conceptually new and unique system for H₂ release from AB, which addresses the catalyst deactivation and storage problems in a simple, inexpensive and efficient way. This work highlights that natural minerals, which appear to be benign, under the right conditions, could be transformed into active catalysts that can play a key role in energy-related applications.

4 Hydrogenation of Nitroarenes to Anilines by Ammonia Borane Hydrolysis

4.1 Introduction

Anilines are key intermediates in the chemical industry for the production of polymers, dyes, pharmaceuticals, and fragrances. The majority of anilines (85% of global production) are produced by the catalytic hydrogenation of nitrobenzenes [153]. Although hydrogenation of nitrobenzenes to anilines has been performed since mid-1850s, different catalytic systems have still been under development to increase the efficiency of the reactions, as well as to tackle with the product selectivity problems where different functional groups (e.g., $-\text{OH}$, $-\text{Cl}$, $-\text{C}=\text{O}$) are present on the nitrobenzene molecule [45, 47]. Nitrobenzene compounds have been hydrogenated in the presence of a variety of metal-catalysts by the use of H_2 gas for many years [47, 154, 155]. However, the utilization of H_2 gas requires high temperature and pressure reaction conditions. For example, the hydrogenation of nitrobenzene to aniline has been conducted in industry by the use of H_2 gas in the presence of copper or nickel catalysts, where the high temperatures of 553–573 K and pressures of H_2 of 0.1–0.5 MPa were required [156]. The high pressure of H_2 gas is necessary due to its low solubility in most solvents, which creates safety concerns and problematic handling of high-pressure H_2 gas.

Since sufficient interaction between the H_2 and nitro compounds is required to boost the reaction efficiency, different approaches have been investigated to generate H_2 *in-situ*. There has been an increasing research on tandem reactions where H_2 is produced *in-situ* from different H_2 sources and followed by a subsequent hydrogenation reaction. By this way, H_2 can

It should be noted that our publication “**Kinik, F. P.**, Nguyen, T. N., Mensi, M., Ireland, C. P., Stylianou, K. C. and Smit, B., 2020. Sustainable Hydrogenation of Nitroarenes to Anilines with Highly Active in-situ Generated Copper Nanoparticles. *ChemCatChem*, 12, 2833–2839” has been reused for this thesis chapter. F. P. K. synthesized the materials, designed and performed the experiments, analyzed the data, and wrote the manuscript with contribution from all authors.

be in contact with the catalyst surface closely and mass-transfer limitations can be eliminated [157]. Moreover, the time of selective hydrogenation reactions can be shortened and the possibility of over-hydrogenation can be avoided. Elimination of high H₂ gas pressure and long reaction times are significant from the industrial safety point of view [157]. For the simultaneous dehydrogenation and hydrogenation reactions, chemical hydrides as H₂ sources have been suggested as alternatives for gaseous H₂ [158].

In the literature, it has been shown that AB has been used for the hydrogenation of a diverse range of unsaturated compounds; including alkenes [159], alkynes [160], nitriles [161] and imines [162]. Therefore, the combination of its dehydrogenation with the hydrogenation of nitrobenzene can propose a mild route for the synthesis of aniline molecules. There are several studies in the literature where AB was proved to be a promising H₂ source for the hydrogenation of nitrobenzenes to anilines catalyzed by different materials, which can be mainly grouped as metal NPs [163, 164, 165], alloy NPs [50, 166], and supported metal NPs [167, 168, 169]. Lately, the research has been more focused on the earth-abundant catalysts for making hydrogenation reactions sustainable.

4.2 Hydrogenation of Nitroarenes by *in-situ* Generated Cu⁰ NPs

As mentioned previously, Cu has been an active catalyst for the hydrogenation of nitrobenzene to aniline in the industrial scale. However, Cu catalysts are exposed to a comparatively fast deactivation, and reactivation is required after a certain amount of time under the industrial conditions [170]. In the literature, other noble and non-noble metal NPs have been also investigated for the hydrogenation of nitroarene compounds. Since copper is an earth-abundant and one of the cheapest non-noble metals, Cu⁰ NPs have been an attractive alternative for this catalytic process. In our study, we propose a strategy to protect Cu⁰ NPs during the hydrogenation of nitrobenzenes to their corresponding anilines from the most common catalyst deactivation problems such as agglomeration and oxidation, without using any other metal, capping agent or support material.

In this study, our particular interest of the nitro compounds are two drug molecules, flutamide (a nonsteroidal antiandrogen drug which is used primarily to treat prostate cancer) [171] and nimesulide (a nonsteroidal anti-inflammatory drug for pain medication and fever reducing) [172], where the hydrogenation has been carried out to make these drug molecules more compatible with the body [172, 173, 174]. For the hydrogenation of these molecules, Jagadeesh *et al.* [175] developed an earth-abundant catalyst, Fe₂O₃, which performs the reaction at 120 °C with a H₂ pressure of 50 bar in 15 hours. In pharmaceutical industry, H₂ gas is often used with a flammable organic solvent, which increases the safety risk within the manufacturing facility. Moreover, H₂ gas has a limited solubility in solvents (especially in water) and therefore

there is a need for high pressure for its utilization in hydrogenation reactions [176]. Therefore, one would expect that the introduction of active Cu⁰ NPs and the use of AB as the *in-situ* H₂ source at ambient conditions would allow these reactions to be performed at milder conditions efficiently.

Herein, we present that the approach discussed in Chapter 2 for the *in-situ* generation of Cu⁰ NPs from the synthetic mineral can be applied to hydrogenation reactions as demonstrated in Figure 4.1. First, we will demonstrate the activity of *in-situ* generated Cu⁰ NPs toward the hydrogenation of nitroarene compounds to their corresponding anilines, by utilizing the *in-situ* generated H₂ from AB. We will illustrate the versatility of our strategy by the efficient reduction of a wide range of nitro substrates, including drug molecules flutamide and nimesulide. The catalytic activity and the integrity of the Cu⁰ NPs, as well as reformation of fresh synthetic mineral at the end of each cycle will be presented.

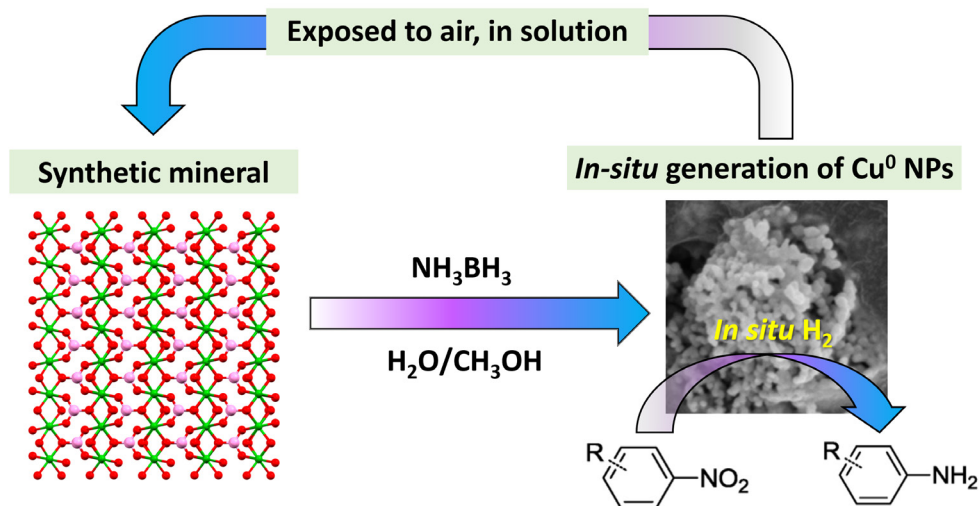


Figure 4.1: Schematic illustration of *in-situ* generation of Cu⁰ NPs from the synthetic mineral using AB as the reducing agent, with the simultaneous conversion of nitroarenes to anilines by *in-situ* hydrogenation. Fresh synthetic mineral can be regenerated at the end of the reaction upon the exposure of reaction solution to air, resulting in the formation of fresh Cu⁰ NPs for the next cycle. Color code for synthetic mineral: Cu: green, O: red, B: light pink.

4.2.1 Hydrogenation of Nitroarenes to Anilines

To demonstrate the applicability of our strategy in hydrogenation reactions, we first investigated the catalytic activity of *in-situ* generated Cu⁰ NPs toward the reduction of nitrobenzene to aniline. This reaction was chosen as the starting point due to nitrobenzene being the simplest molecule among different nitroarene molecules. The hydrogenation experiments were performed at room temperature under vigorous mixing. The molar ratios between the

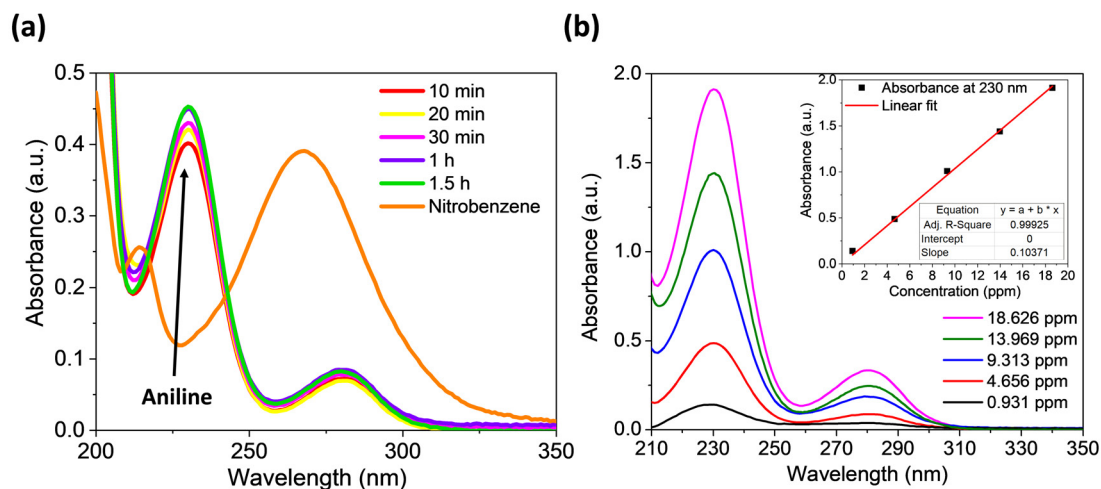


Figure 4.2: (a) UV-Vis spectrum of aniline obtained from the reduction of nitrobenzene at different times of reaction. The samples that were taken for UV-Vis analysis were diluted 200 times. (b) Calibration curve constructed for the determination of aniline yield using the aniline standard from Sigma Aldrich. Inset: the absorbances of calibration solutions at different concentrations of aniline.

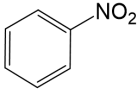
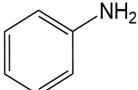
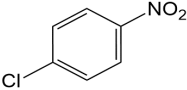
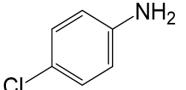
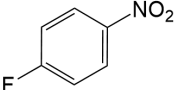
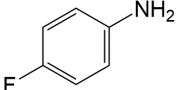
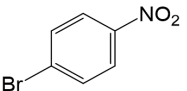
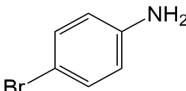
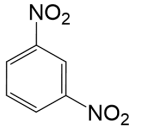
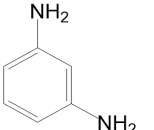
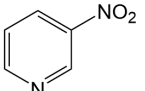
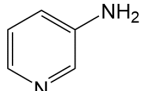
synthetic mineral, nitrobenzene and AB compounds were optimized (mineral/nitroarene/AB = 0.086/0.172/1) and used for the further reactions (Figure A.13, Appendix).

Nitrobenzene and aniline have distinctive light absorption spectra. While the main absorption peak of nitrobenzene occurs at ~ 268 nm, it occurs at ~ 230 nm for aniline. Therefore, the conversion of nitrobenzene can be monitored by UV-Vis spectroscopy, which has been a common technique used in the literature [149, 177, 178, 179]. The hydrogenation of nitrobenzene was conducted for 1.5 h and several measurements were taken at different times of the reaction as shown in Figure 4.2(a). UV-Vis spectra show that at the end of 10 mins of reaction, all nitrobenzene molecules in reaction solution were converted. In order to calculate the aniline yield at different durations of the reaction, calibration curve was constructed using different concentrations of commercial aniline standard (Figure 4.2(b)). While the aniline yield was calculated as 84% at the end of 10 mins, it reached to 94% at the end of 1 h and did not change when the reaction duration was extended to 1.5 h. The purity of the aniline product obtained at the end of the reaction was demonstrated by ^1H NMR measurements, showing that the selectivity toward aniline is 100% as there is no other peak for an intermediate or another product (Figure A.19, Appendix). In the absence of catalyst, no conversion was observed, indicating that the presence of synthetic mineral in the reaction solution plays a key role for the hydrogenation reaction.

After the hydrogenation of nitrobenzene to aniline was successful (Table 4.1, entry 1), the efficiency of our reaction system toward other nitroarene molecules was investigated. The

selected nitroarenes represent different classes and each of these classes is used for the production of different intermediates. The halogenated anilines (Table 4.1, entries 2, 3 and 4) are commonly used intermediates in the manufacture of herbicides, drugs and laboratory reagents [180] and 1,3-diaminobenzene (Table 4.1, entry 5) is used in the manufacture of azo dyes [181]. 3-aminopyridine is an important building blocks in pharmaceuticals and agrochemicals (Table 4.1, entry 6) [182]. All reactions were carried out at room temperature using the optimized conditions. After combining all constituents of the reaction, the solution was sampled after 1 or 2 hours depending on the completion of the reaction. The yield and the selectivity of the products were determined by UV-Vis spectroscopy (Figure A.14 - A.18) and ¹H NMR analysis (Figure A.19 - A.24). In the absence of the catalyst, no conversion was observed for any of the nitroarene molecules. As shown in Table 4.1, except from 1-bromo-4-nitrobenzene and 3-nitropyridine, all investigated nitroarene compounds were converted within 1 hour with > 90% yield and > 99% selectivity. For 3-nitropyridine, we achieved a similar yield at the end of 2 hours while for 1-bromo-4-nitrobenzene, we obtained 40% yield after 2 hours also with 100% selectivity. The presence of the electron-withdrawing Cl⁻ and F⁻ groups does not affect the reaction and the aniline products were obtained in quantitative yields (Table 4.1, entries 2-3). In case of Br⁻ analogue (Table 4.1, entry 4), the yield is 40%, which might probably be due to the lower electronegativity of Br compared to Cl and F; therefore, the nitro group is less electron deficient. The reduction of the nitro group is not affected by the presence of another nitro group, as shown for the case of 1,3-dinitrobenzene. In fact, both nitro groups were efficiently reduced to amines with 100% yield. Dell'Anna *et al.* [183] reported similar findings, where the hydrogenation rate of 1-bromo-4-nitrobenzene is slower (61% yield in 6 hours) than that of 1,3-dinitrobenzene (96% yield in 6 hours). In that study, mono-amino products were observed only in negligible quantities during the reaction. Similarly, in our case, no mono-amino product was observed at the end of 1-hour reaction as indicated by ¹H NMR analysis (Figure A.24). Therefore, it can be interpreted that the reduction of the intermediate product is fast in the case of 1,3-dinitrobenzene, whereas electronegativity difference makes the reaction rate slower in the case of 1-bromo-4-nitrobenzene.

As the stability and recyclability of the catalyst are highly crucial for practical applications, the integrity and catalytic performance of *in-situ* generated Cu⁰ NPs were investigated. Figure 4.3(a) shows the recyclability of the catalyst during five consecutive runs for nitrobenzene to aniline reduction. Within the accuracy of UV-Vis instrument, aniline yield higher than 90% for each of the runs was observed without any catalyst deactivation. As shown in Figure 4.3(b), there is no significant change in the PXRD pattern of the regenerated synthetic mineral after each reaction cycle, which indicates that the original synthetic mineral is fully recovered. Hence, each of the catalytic cycle is carried out with a fresh material and no loss of catalytic activity is observed. This finding is highly important since Cu-based catalysts might gradually lose their initial catalytic activity during the hydrogenation reaction, even when

Entry	Substrate	Product	Yield (%)	Selectivity (%)	Time
1			>90	>99	<1 h
2			>99	>99	<1 h
3			>99	>99	<1 h
4			~40	>99	<2 h
5			>99	>99	<1 h
6			~83 (100)	>99	<1 h (<2 h)

Reaction conditions: 0.1 mmol nitro compound, 0.583 mmol AB, 12 mg catalyst, 1 ml MeOH, 9 ml H₂O, 25 °C.

Table 4.1: Hydrogenation of various nitroarenes to anilines by the simultaneous in-situ formation of Cu⁰ NPs and dehydrogenation of NH₃BH₃.

they are combined with other metals or supported on porous media. For example, Yu *et al.* [184] prepared as-synthesized CuNi NPs and tert-butylamine-treated CuNi NPs supported on graphene for the hydrogenation of aromatic nitro compounds by the methanolysis of AB. As-synthesized CuNi NPs could retain less than 40% of their initial activity at the end of the 5th cycle, and even after the treatment with tert-butylamine and use of graphene as the support, the catalytic activity decreased to the 80% of the initial activity at the end of the 10th cycle, which is due to the weakened interaction between graphene and NPs through the cycles. In another example, Madasu *et al.* [163] prepared polyhedral Cu crystals from Cu₂O cubes by using AB as the reducing agent, then performed simultaneous nitroarene hydrogenation at 30 °C. The hydrogenation of 4-nitroaniline to benzene-1,4-diamine was obtained with 100% conversion in the 1st cycle, but 88% conversion was observed for the 2nd cycle due to the catalyst deactivation.

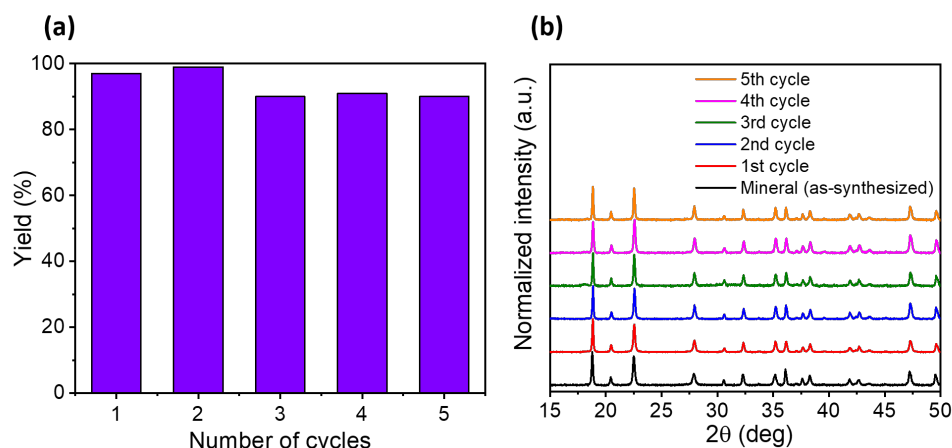


Figure 4.3: (a) Recycling experiments for the hydrogenation of nitrobenzene to aniline, showing the stability of the hydrogenation performance. (b) PXRD patterns of regenerated synthetic mineral at the end of each reaction cycle.

4.2.2 Hydrogenation of Drug Molecules

The hydrogenation of drug molecules, flutamide and nimesulide, was studied using the same methodology as for the other nitroarenes to generalize our concept with different molecules. The only difference is that deuterated methanol and deuterated water were used in the reaction system to facilitate the determination of the purity, yield, and selectivity by ¹H NMR analysis. The yields of the reduced drugs were determined by ¹H NMR analysis, using tetrahydrofuran (THF) at a known concentration as the internal standard (Figure A.26 - A.27). The catalytic performance of Cu⁰ NPs was found to be outstanding; >99% selectivity toward the hydrogenation of -NO₂ to -NH₂ with high yield was observed, at room temperature, within 1 hour and ambient pressure. In general, the reduction of nitro groups to their corresponding amines is challenging when other reducible groups (such as carbonyl, aldehyde, or alkene) are present in the structure. Moreover, the reduction of aromatic nitro compounds tends to stop at an intermediate stage, resulting in hydroxylamines, hydrazines and azoarenes [185]. Although there are functional groups in drug molecules (e.g. carbonyl group in flutamide) that can also be reduced with H₂, only the -NO₂ to -NH₂ reduction was observed, without the formation of any intermediate product. The ¹H NMR spectrum (Figure 4.4) shows that after the hydrogenation of flutamide, all chemical shifts are assigned to the corresponding amino-derivative compound, without showing any additional peak appearing due to the reduction of C=O group. The decrease in the ¹H chemical shifts after the replacement of -NO₂ group with -NH₂ is due to the increasing electron density in the ring, resulting from the lower electronegativity of -NH₂ compared to -NO₂. Moreover, for the reductions of both drug molecules, pure and fresh synthetic mineral could be recovered at the end of the cycle, and therefore no loss in catalytic activity is observed. One therefore would expect that the intro-

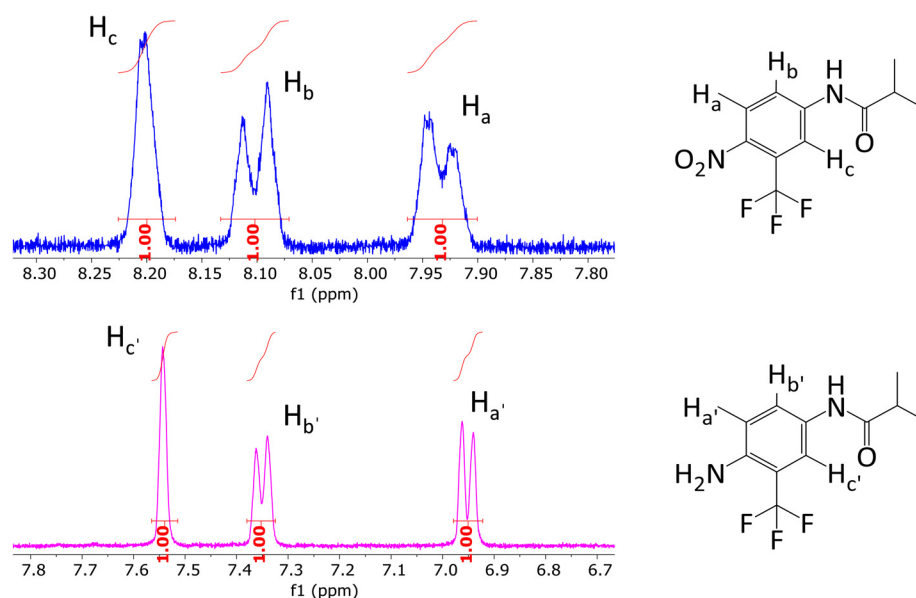


Figure 4.4: ¹H NMR spectra of commercial flutamide (top, blue) and hydrogenated flutamide (bottom, pink) and the assignments of the peaks. The spectra of aromatic rings in commercial flutamide and hydrogenated flutamide are demonstrated to show the chemical shifts after the conversion of -nitro to -amino. The reaction was performed in a mixture of deuterated methanol and deuterated water ($V_{\text{MeOH-d}_4} : V_{\text{D}_2\text{O}} = 1:9$). The decrease in the ¹H chemical shifts after the replacement of -NO₂ group with -NH₂ is due to the increasing electron density in the ring, resulting from the lower electronegativity of -NH₂ compared to -NO₂.

duction of active Cu⁰ NPs, and the use of AB as the H₂ source, would allow the hydrogenation reactions in pharmaceuticals to be performed at safer conditions (at room temperature and under ambient pressure) efficiently.

4.3 Summary and Conclusions

In summary, the *in-situ* generation of Cu⁰ NPs from the synthetic Jacquesdietrichite mineral was successfully applied for the reduction of nitroarene compounds to their corresponding anilines with high yields. The catalytic activity and integrity of the catalyst remained unaffected for at least 5 cycles of reaction, which is due to the reformation of the fresh synthetic mineral at the end of each cycle. Of particular importance is the hydrogenation of the drug molecules “flutamide” and “nimesulide” at room temperature and pressure with the use of AB as the H₂ source. The superiority of *in-situ* generated Cu⁰ NPs compared to other Cu-based catalysts is that Cu⁰ NPs can be formed as fresh when needed, preventing any possible aggregation or oxidation problem during reaction cycles or the storage of the catalyst. This work paves the way for the solution of common deactivation challenges of earth-abundant catalysts.

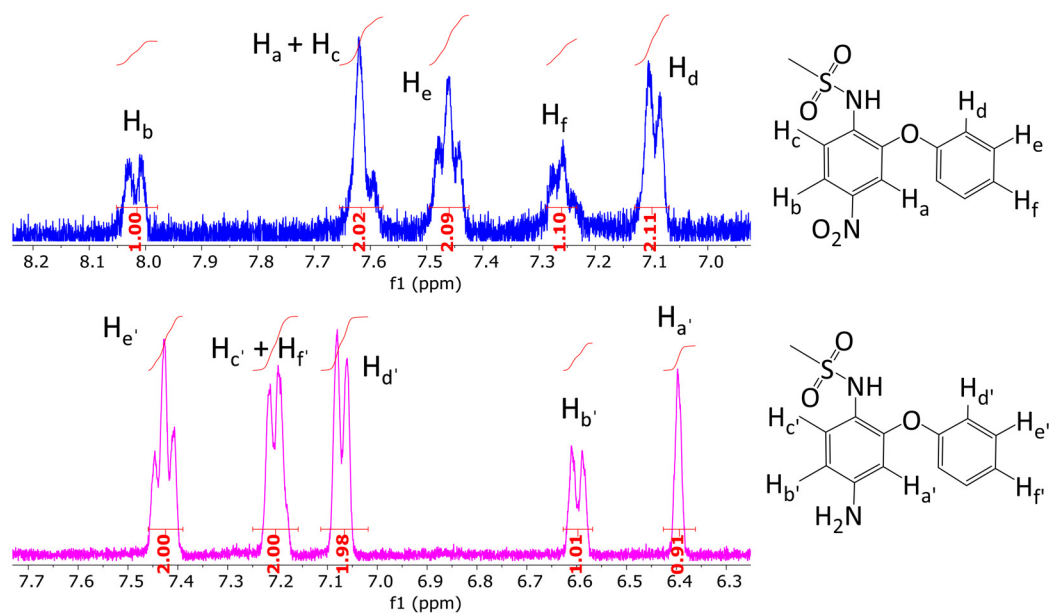


Figure 4.5: ^1H NMR spectra of commercial nimesulide (top, blue) and hydrogenated nimesulide (bottom, pink) and the assignments of the peaks. The spectra of aromatic rings in commercial nimesulide and hydrogenated nimesulide are demonstrated to show the chemical shifts after the conversion of -nitro to -amino. The reaction was performed in a mixture of deuterated methanol and deuterated water ($V_{\text{MeOH-d}_4} : V_{\text{D}_2\text{O}} = 1:9$). The decrease in the ^1H chemical shifts after the replacement of $-\text{NO}_2$ group with $-\text{NH}_2$ is due to the increasing electron density in the ring, resulting from the lower electronegativity of $-\text{NH}_2$ compared to $-\text{NO}_2$.

5 Conclusions and Outlook

5.1 Summary

With the increasing importance of H₂ energy in present days, different approaches for its efficient generation, safe release after storage, and versatile utilization have been under investigation with a tremendous interest. In order to achieve all these targets, the choice of the catalyst has been of importance for high efficiency, long-lasting stability and sustainability. In this thesis, we focused on different aspects of H₂ energy considering the application of inorganic and metal-organic heterogeneous catalysts. While we studied the photocatalytic generation of H₂ from water by using MOFs as photocatalysts, we presented the efficient employment of an earth-abundant mineral as the inorganic catalyst for H₂ release from AB, followed by its use for important industrial hydrogenation reactions.

In Chapter 2, we investigated different factors that can be relevant for the optimum photocatalytic activity of MOFs toward H₂ generation from water. The most common understanding of MOFs as photocatalysts is that, having proper band alignment, suitable band gap, and efficient light absorption make them promising candidates to catalyze water and generate H₂. This insight is indeed accurate; yet there are many more aspects to consider. In our study, the synergy between the experiments and computations on pyrene-based MOFs showed that it is possible to suggest efficient photocatalysts by studying different factors all together. This work demonstrated that the electronic and optical characteristics should be investigated jointly with the morphological characteristics to reach the optimum catalytic activity.

In Chapter 3 and 4, we explored a novel approach for efficient H₂ release from AB as promising storage medium, and the utilization of generated H₂ in hydrogenation reactions. AB has been extensively studied due to its promising H₂ capacity and requirement for mild reaction conditions, and proposed as a future H₂ storage medium for mobile and stationary applications. Our approach suggests the *in-situ* generation of the active catalyst (Cu⁰ NPs) from

a host structure (synthetic Jacquesdietrichite mineral) during the hydrolysis reaction, and the reformation of host material at the end of the reaction. This way, we could propound an efficient way to eliminate the catalyst deactivation problems by generating the active catalyst freshly during each reaction step.

5.2 Future Work

The main focus of this thesis was to develop better understanding about metal-organic photocatalysts for H_2 generation from water, as well as to suggest sustainable catalytic approaches for the storage, release and utilization of H_2 energy. We believe that our studies discussed in the previous chapters can be expended.

In Chapter 2, although the outcomes of our study were rewarding to widen our understanding about photocatalytic HER with MOFs, there is still a lot of room for improvement. The MOF photocatalysis literature is mainly dominated by Ti-based materials, due to the empty d-orbitals of Ti promoting charge separation efficiency. However, the combination of other metals with the optically and electronically favorable ligands can end up with photocatalytically active MOFs. Therefore, theoretical screening studies of MOFs with different metals focusing on the investigation of electronic and optical characteristics can suggest promising candidates for photocatalytic HER. Another important aspect is the detailed understanding of the effect of reaction elements. For example, sacrificial electron donors are mostly crucial for photocatalytic HER. However, their efficiency and oxidation mechanisms are not well understood yet. Therefore, we believe that a detailed study for understanding the role of sacrificial reagents in photocatalytic HER would be worthwhile. The last but not the least, co-catalysts are important constituents of photocatalytic HER with MOFs. Although it is well-known that co-catalysts tend to increase photocatalytic HER efficiency, they have a lack of detailed investigation. We believe that controlling the growth and dispersion of co-catalysts on MOFs, as well as analyzing the interactions between them is highly important. We envision that combining this understanding with the methodological investigation that we present in this thesis can pave the way for the researchers.

In Chapter 3 and 4, we could propose encouraging solutions for the sustainability of Cu^0 NPs for AB hydrolysis. However, AB still needs more improvement to be implemented as H_2 storage material in industrial applications since its cost-effective synthesis and regeneration from the residues remained as challenges. There are studies in the literature providing innovative solutions to close the H_2 cycle with the regeneration of AB after its use. However, these are still far away from being applicable in industrial setups. We believe that there should be more research interest towards tackling these issues, as well as scaling up the production of AB. Hydrolysis of AB has not been performed in a prototype yet, which is an important step for its

industrialization. The effective gravimetric H₂ storage capacity of AB should be studied further on a demonstrator, considering the effect of water amount used in the reactions. Following the consideration of all these issues, AB can be a promising H₂ storage medium for both mobile and stationary applications.

A Appendices

A.1 Materials

All chemicals were purchased from commercial suppliers and used without any further purification: $\text{Sc}(\text{NO}_3)_3 \cdot x\text{H}_2\text{O}$ (Sigma Aldrich, 99.9%), $\text{Al}(\text{NO}_3)_3 \cdot 9\text{H}_2\text{O}$ (Sigma Aldrich, $\geq 98\%$), $\text{In}(\text{NO}_3)_3 \cdot x\text{H}_2\text{O}$ (Alfa Aesar, 99.99%), dimethylformamide (DMF) (Carl Roth, $\geq 99\%$), acetonitrile (CH_3CN) (Sigma Aldrich, $\geq 99.5\%$), triethylamine (TEA) (Sigma Aldrich, $\geq 99\%$), cetyltrimethylammonium bromide (CTAB) (Sigma Aldrich, $\geq 98\%$), copper (II) sulfate pentahydrate ($\text{CuSO}_4 \cdot 5\text{H}_2\text{O}$, Sigma-Aldrich, 98%), NaBH_4 (Sigma-Aldrich, 99%) NH_3BH_3 (Sigma-Aldrich, 90%), copper (II) sulfate pentahydrate ($\text{CuSO}_4 \cdot 5\text{H}_2\text{O}$, Sigma-Aldrich, 98%), NaBH_4 (Sigma-Aldrich, 99%), NH_3BH_3 Sigma-Aldrich, 90%), methanol (Fisher Chemical, $\geq 99.9\%$), nitrobenzene (Sigma-Aldrich, 99%), 1-chloro-4-nitrobenzene (Sigma-Aldrich, 99%), 1-fluoro-4-nitrobenzene (Sigma-Aldrich, 99%), 1-bromo-4-nitrobenzene (Sigma-Aldrich, 99%), 1,3-dinitrobenzene (Sigma-Aldrich, 97%), 3-nitropyridine (Sigma-Aldrich), aniline (Acros Organics, 99.8%), 4-chloroaniline (Alfa Aesar, 98%), 4-fluoroaniline (Sigma-Aldrich, 99%), 4-bromoaniline (Apollo Scientific), 1,3-diaminobenzene (Sigma-Aldrich, 99%), 3-aminopyridine (Sigma-Aldrich, 99%), flutamide (Sigma-Aldrich), nimesulide (Sigma-Aldrich), deuterium oxide (Sigma-Aldrich), methanol-d4 (Sigma-Aldrich).

A.2 Experimental Methods

PXRD data on all samples were collected on a Bruker D8 Advance diffractometer at ambient temperature using monochromated Cu K α radiation ($\lambda = 1.5418 \text{ \AA}$), with a 2θ step of 0.02° with

It should be noted that the sections "A.1 Materials" and "A.2 Experimental Methods" in Appendices include the information for all chapters in this thesis.

different 2θ ranges. Simulated PXRD patterns were generated from the corresponding crystal structures using Mercury 3.0. FTIR measurements were performed with the Spectrum Two FTIR spectrometer (Perkin Elmer) in the transmittance mode from 400 to 4000 cm^{-1} . The N_2 adsorption isotherm measurements were performed at 77 K by using BELSORP Mini (BEL Japan, Inc.). Prior to measurements, samples were activated at 170 °C (M-TBAPy samples) or at 120 °C (synthetic mineral) for 12 h under vacuum. A part of the nitrogen adsorption isotherm in the p/p_0 range 0.06 - 0.25 was fitted to the BET equation to estimate the surface areas of the samples. The morphological characteristics were investigated by SEM on the FEI Teneo SEM instrument. For SEM measurements, all samples were deposited on a carbon tape. Conventional TEM images were collected on the FEI Tecnai Spirit instrument at 120 kV acceleration voltage. A PerkinElmer Thermogravimetry Analyzer was used to determine the decomposition temperature of the samples. All measurements were performed under air flow up to 600 °C. ICP-OES measurements were performed using a NexIon 350 (Perkin Elmer) spectrometer. XPS analysis was performed using PHI 5000 Versaprobe-II instrument from Physical Electronics. Samples were deposited on an insulating double sided, vacuum compatible, tape, and charge neutralization was applied during the XPS measurements. The binding energy scale was then corrected with the C-C bond of the C1s photoelectron peak located at 284.6 eV. Peak fitting of the Cu 2p_{3/2} photoelectron peak, along with the kinetic energy of the Cu L3M45M45 peak, were used to evaluate the chemical state of copper. ^1H NMR analyses were performed on a Varian 400 MHz NMR spectrometer.

The UV-Vis absorbance spectra were obtained with a PerkinElmer UV-Vis Spectrometer. Photoluminescence spectra and excitation spectra were measured with a Fluorescence Spectrometer LS 55 (PerkinElmer). For photoluminescence measurements, the excitation wavelength was 420 nm. Excitation spectra were probed for the 500 nm emission by exciting between 350 and 470 nm. Both measurements were performed on suspensions of 1.7 mg of the MOFs in 1.7 mL of acetonitrile. Photoluminescence lifetimes were measured on a Horiba Jobin Vyon Fluorolog-3 instrument equipped with a photomultiplier for detection. The samples were excited with a 355 nm pulsed LED laser and a 420 nm pulsed LED laser to determine the photoluminescence lifetimes. The excitation wavelength had no effect on the average lifetimes of the samples. nTAS data were recorded using a LP980 laser flash spectrometer from Edinburgh Instruments. The samples were excited by 5 ns laser pulses at 420 nm (nanosecond tunable Ekspla NT340 laser with 5 Hz repetition rate), and transient absorption spectra were recorded between 250 and 650 nm with a 20 nm interval.

A.3 Supporting Information for Chapter 2

A.3.1 Material Synthesis

The synthesis of TBAPy ligand was performed based on the previously reported procedure [186]. Al-TBAPy and In-TBAPy were synthesized according to the synthesis methods reported previously [78, 64]. They were obtained in powder form with ~30% and ~56% yield, respectively. Single crystal XRD (SCXRD) data for In-TBAPy was reported in the original study [64]. The cell parameters of In-TBAPy obtained from SCXRD data ($a = 30.748(18) \text{ \AA}$, $b = 7.120(4) \text{ \AA}$, $c = 15.932(9) \text{ \AA}$) were used for the confirmation of isostructural characteristics of M-TBAPy MOFs.

The synthesis for Sc-TBAPy was performed in 12 mL Pyrex reactor, where TBAPy (0.015 mmol, 10 mg) and $\text{Sc}(\text{NO}_3)_3 \cdot x\text{H}_2\text{O}$ (0.03 mmol, 6.9 mg) were added to 4 mL of DMF/dioxane/ H_2O mixture (2:1:1) followed by adding 10 μL of concentrated HNO_3 . The suspension was sonicated for 15 minutes for the complete dissolution of ligand. The reaction mixture was heated at 85 $^\circ\text{C}$ for 12 h, with a heating rate of 2 $^\circ\text{C min}^{-1}$ and then cooled to room temperature at a rate of 0.2 $^\circ\text{C min}^{-1}$. The solid was recovered by centrifuge, and washed with DMF in order to remove any recrystallized TBAPy ligand. After drying, the as-made Sc-TBAPy MOF was obtained as a yellow solid powder with ~50% yield. The peak indexation of Sc-TBAPy showed that the MOF has an orthorhombic unit cell with experimental cell parameters of $a = 30.25(8) \text{ \AA}$, $b = 7.13(1) \text{ \AA}$, $c = 15.32(4) \text{ \AA}$, which are in agreement with the reported cell parameters of Ti-TBAPy and In-TBAPy [64, 74]. Le Bail analysis of the collected powder pattern was carried out using TOPAS5 software [187]. The profile fits confirmed that Sc-TBAPy is isostructural to the other M-TBAPy MOFs, with the space group of *Cmmm* (no.65) (Figure A.1).

For the synthesis of Sc-2, the same amount of TBAPy (0.015 mmol, 10 mg) and $\text{Sc}(\text{NO}_3)_3 \cdot x\text{H}_2\text{O}$ (0.03 mmol, 6.9 mg) were added to 4 mL of DMF/dioxane/ H_2O mixture (2:1:1), followed by adding 10 μL of concentrated HNO_3 and 4.38 mg of CTAB. In the case of Sc-3, all the amounts remained the same except from the modulator (HNO_3), which is excluded from the synthesis. The suspensions were sonicated for 15 minutes for the complete dissolution of ligand. The reaction mixtures were heated at 120 $^\circ\text{C}$ for 72 h, with a heating rate of 2 $^\circ\text{C min}^{-1}$ and then cooled to room temperature at a rate of 0.2 $^\circ\text{C min}^{-1}$. Yellow powder samples were recovered by centrifuge, and washed with DMF in order to remove any recrystallized TBAPy ligand.

A.3.2 Photocatalytic Experiments

The photocatalytic H_2 evolution experiments were performed in a 25 mL Pyrex glass reactor at room temperature, under continuous visible light irradiation from a 300 W Xe lamp equipped with a UV cut-off filter ($\lambda \geq 420 \text{ nm}$). For the photocatalytic experiment, 17 mg of M-TBAPy sample was immersed in 17 mL of photocatalytic solution, which is composed of acetonitrile,

TEA and Millipore water in a volumetric ratio of 50:10:1, respectively. The suspension was first sonicated for 15 minutes, and then purged with nitrogen gas for another 15 minutes under stirring, in order to eliminate any dissolved oxygen in the reaction environment. When the reaction is complete, 200 μL of the gaseous product was taken from the head space of the reactor to be analyzed by gas chromatography (PerkinElmer Clarus 480 GC, N_2 carrier gas), equipped with a thermal conductivity detector and a molecular sieve 5 \AA column.

A.3.3 Computational Details

The periodic structures of M-TBAPy (M = Al, In, Sc and Ti) MOFs were optimized using the 65 space group (*Cmmm*) symmetry in CRYSTAL17 code[188]. All the structures were optimized using the PBE0 XC functional along with D3BJ dispersion corrections. Likewise, we further optimized the atomic coordinates of the structures considering the rotation of the benzene groups in the MOFs. Double- ζ basis set pob-DZVP was used to described the organic atoms, while triple- ζ pop-TZVP basis was used to described the metal atoms. The shrinking factors for the diagonalization of the Kohn-Sham matrix in the reciprocal space has been set to 4 for the Monkhorst-Pack and 4 for the Gilat nets. Bandstructures calculations were computing using the reciprocal space path within the first Brillouin zone in the primitive cell using the Seek-path package [189] using the primitive cell.

The study of the optical excitations in the periodic structures was performed in the CP2K code [190]. All structures were optimized initially with the PBE functional followed by second optimization using the PBE0 exchange and correlation (XC) functional with the D3BJ dispersion correction in both cases. The double- ζ polarization MOLOPT basis sets were used to describe organic atoms, while a triple- ζ was used for metal atoms. The PBE0 calculations used the auxiliary MOLOPT-ADMM basis functions: cFIT8 for Al, cFIT12 for In, Sc and Ti, and pFIT3 for non-metal atoms. The Truncated Coulomb operator with a long-range correction was employed for the Hartree-Fock exchange of hybrid calculations. Both symmetric and rotated phenyl structures were considered as well using a 1x3x1 super cell of the conventional cell and a 4x1x1 of the primitive cell, respectively. The use of 2x2x2 Monkhorst-Pack scheme in the initial PBE optimization guarantees the symmetrical orientation of the phenyl groups as an starting point for the PBE0 optimizations. On the other hand, the starting configuration of the rotated structure for the PBE0 optimization is obtained by rotating the phenyl groups and without the use of K-points during the PBE optimization. The truncation radius is half of the smallest edge of the unit cell (7.5 \AA), and the long-range part of the exchange is computed using the PBE exchange. All calculations conducted with PBE0 used the orbital transformation (OT) method. The LR-TDDFT scheme including the Tamm-Dancoff approximation was used to predict the optical bandgap of the systems. To align the conduction and valence band energies with vacuum, the methodology proposed by Butler *et al.* [191] was used to calculate

the vacuum level in the periodic systems. This method consists of evaluating the average potential within a small sphere at the pore centre.

A.3.4 Structural and Optical Characterization

Thermogravimetric analysis (TGA) reveals that all M-TBAPy MOFs are stable up to 500 °C (Figure A.2). Nitrogen adsorption-desorption analysis at 77 K showed that Sc-TBAPy has a BET surface area of 1197 m² g⁻¹ (Figure A.2(b)), which is close to those of Ti-TBAPy (1212 m² g⁻¹) [74] and In-TBAPy (1189 m² g⁻¹) [64].

A.3.5 Calculation of Apparent Quantum Yield

Calculation of the number of photons emitted by Xenon lamp

To calculate the apparent quantum yield for M-TBAPy samples, first the moles of photons emitted by the Xenon lamp were calculated by using ferrioxalate actinometry [85]. This method involves the reduction of potassium ferrioxalate (K₃Fe(C₂O₄)₃ · 3H₂O) in the presence of light, and the resulting Fe²⁺ ions are quantified by the complexation with 1,10-phenanthroline. Standard values for the quantum yield of Fe²⁺ formation can be used for the calculation of the apparent quantum yield of a specific photocatalytic reaction.

The conditions for the preparation of solutions, and for the reaction (the formation of Fe²⁺) were taken from the literature [85]. The moles of Fe²⁺ were calculated by using the formula:

$$n_{\text{Fe}^{2+}} = \frac{V_1 \cdot V_3 \cdot A}{10^3 \cdot V_2 \cdot L \cdot \epsilon}$$

V₁: irradiation volume (17 mL), V₂: sample taken (0.5 mL), V₃: final volume (5 mL), L: optical path-length (1 cm), A: absorbance difference at 510 nm (3.2589 at 400 nm irradiation, and 3.3297 at 450 nm irradiation), ε: absorbance coefficient (11100 L mol⁻¹ cm⁻¹).

n_{Fe²⁺} were found as 4.991 * 10⁻⁵ mol and 5.099 * 10⁻⁵ mol at 400 and 450 nm radiation, respectively.

Then, the number of photons can be calculated based on the formula below:

$$\frac{n_{\text{photons}}}{n_{\text{min}}} = \frac{n_{\text{Fe(II)}}}{\phi_{\lambda} \cdot t \cdot F}$$

φ_λ: quantum yield for iron production at wavelength λ (1.14 at ~ 405 nm and 1.11 at ~ 450 nm), t: time (46 min), F: mean fraction of light absorbed (1).

Appendix A. Appendices

Based on these calculations, $n_{\text{photons}} / n_{\text{min}}$ at 400 nm and 450 nm were obtained as $9.518 * 10^{-7}$ mol and $9.987 * 10^{-7}$ mol, respectively.

Apparent quantum yield (AQY) determination

To calculate AQY values, first the photocatalytic reactions were carried out using the same photocatalytic solution and setup which was mentioned previously. The H_2 evolution was investigated under 400 and 450 nm radiation by using relative band pass filters with the 300 W Xenon lamp. Below, the moles of H_2 generated for each sample (in 3 hours) are given:

Table A.1: HER rates of M-TBAPy MOFs irradiated at 400 and 450 nm.

H_2 generation in 3 hours (mol)		
MOF Name	400 nm	450 nm
In-TBAPy	negligible	negligible
Al-TBAPy	negligible	$6.450 * 10^{-8}$
Sc-TBAPy	$6.550 * 10^{-8}$	$3.270 * 10^{-7}$

AQY values were calculated based on the formula below:

$$AQY(\%) = 2 * \frac{\frac{n_{\text{rate}}}{\text{min}}}{\frac{n_{\text{photons}}}{\text{min}}} * 100$$

AQY values for Sc-TBAPy and Al-TBAPy can be found as:

- AQY for Sc-TBAPy at 400 nm = 0.076%
- AQY for Al-TBAPy at 400 nm = 0.076%
- AQY for Sc-TBAPy at 450 nm = 0.364%
- AQY for Al-TBAPy at 450 nm = negligible

Table A.2: Photoluminescence lifetimes (t_1) and (t_2) of M-TBAPy MOFs recorded at 500 nm wavelength, based on the photoluminescence emission peaks of the MOFs.

MOF	t_1 (ns)	t_2 (ns)
Al-TBAPy	2.72	13.42
In-TBAPy	2.84	12.18
Sc-TBAPy	2.40	11.70

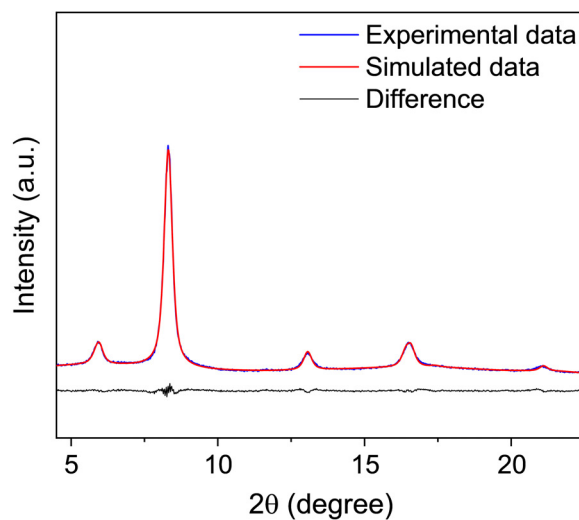


Figure A.1: Le Bail fit obtained from the PXRD data of Sc-TBAPy MOF. Orthorhombic space group *Cmmm* (no. 65), $a = 30.25(8) \text{ \AA}$, $b = 7.13(1) \text{ \AA}$, $c = 15.32(4) \text{ \AA}$, $V = 3305(14) \text{ \AA}^3$. GOF parameters: $wRp = 0.024$, $Rp = 0.019$.

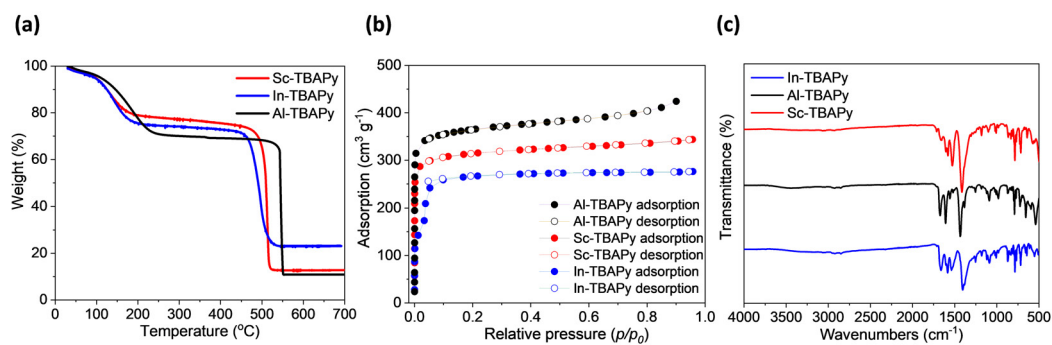


Figure A.2: (a) TGA curves, (b) N_2 adsorption and desorption isotherms (at 77 K), and (c) FTIR spectra of Sc-TBAPy, In-TBAPy and Al-TBAPy.

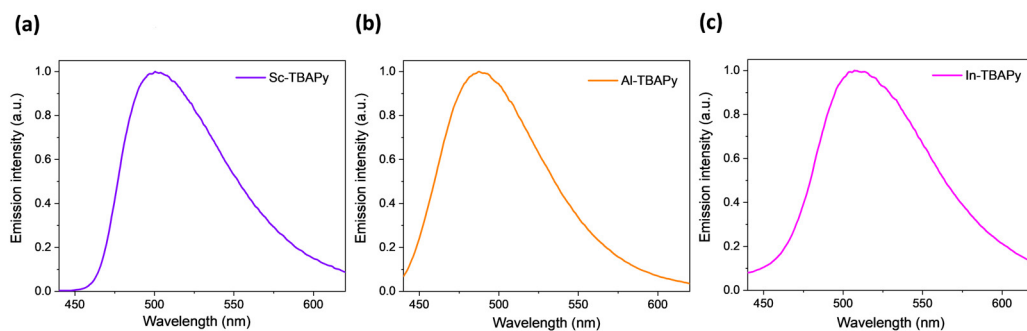


Figure A.3: Photoluminescence spectra of (a) Sc-TBAPy, (b) Al-TBAPy, and (c) In-TBAPy. MOFs were suspended in acetonitrile and excited at 420 nm.

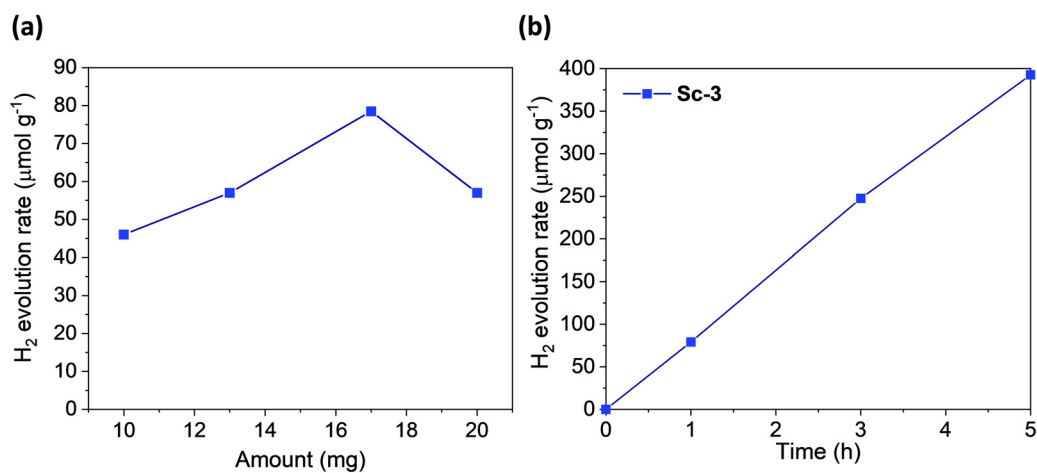


Figure A.4: (a) Optimization of the amount of Sc-3 used in HER, upon visible light exposure ($\lambda \geq 420$ nm). Reaction conditions: 13.93 mL acetonitrile, 2.79 mL TEA and 0.279 mL H_2O . The experiment duration was 5 h. The optimized amount (17 mg) was used for all other M-TBAPy MOFs. (b) The HER rate of Sc-3 for 5 h of photocatalytic reaction.

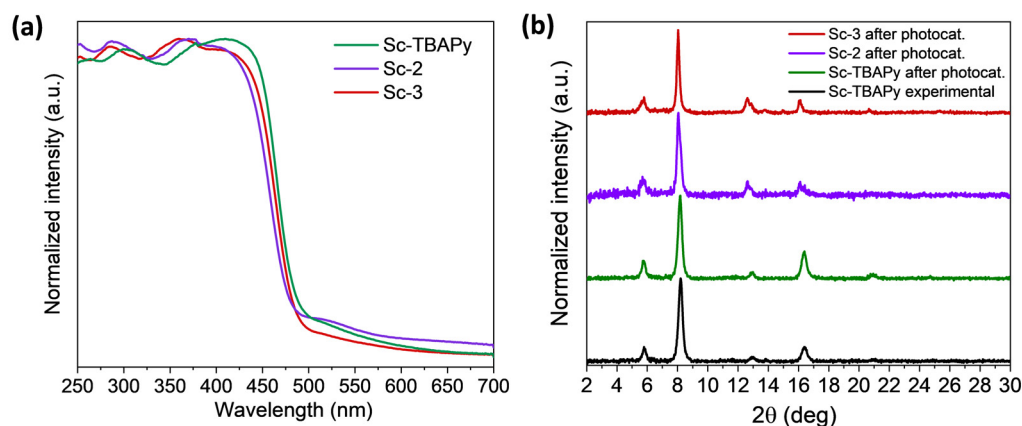


Figure A.5: (a) UV-Vis spectra of Sc-TBAPy, Sc-2 and Sc-3 samples, showing their similar light absorption capability. (b) PXRD patterns of Sc-TBAPy, Sc-2, and Sc-3 samples after photocatalysis, showing that all Sc-MOFs are stable after the HER.

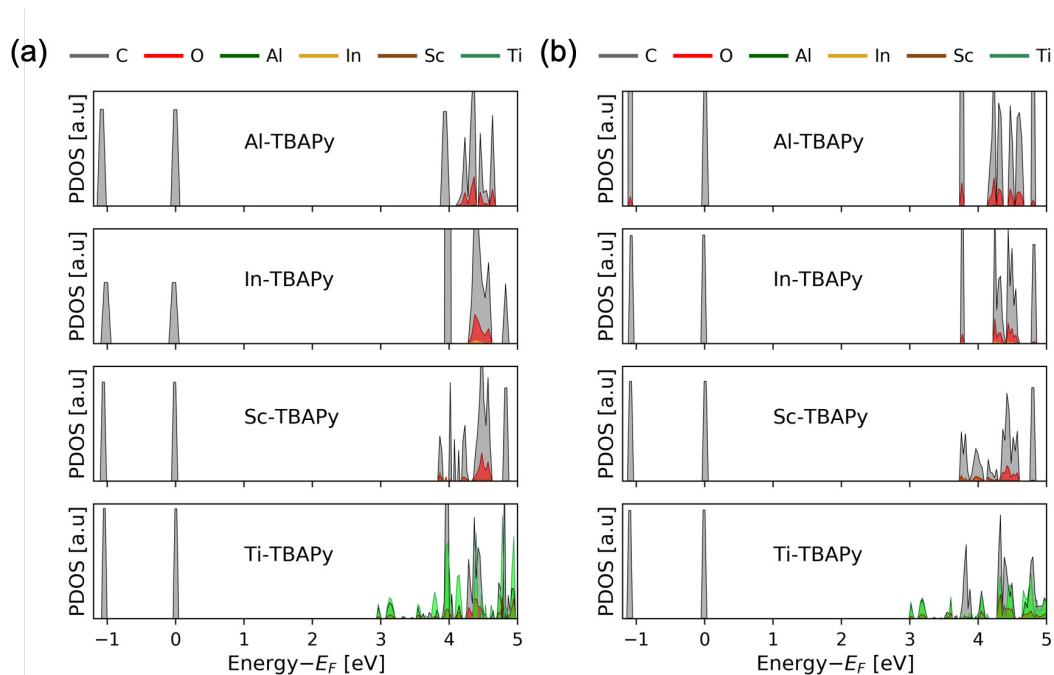


Figure A.6: Projected density of states of (a) the high-symmetry structure, and (b) the phenyl rotated structures of Al-TBAPy, In-TBAPy, Sc-TBAPy, and Ti-TBAPy with PBE0 functional, CRYSTAL17 calculations.

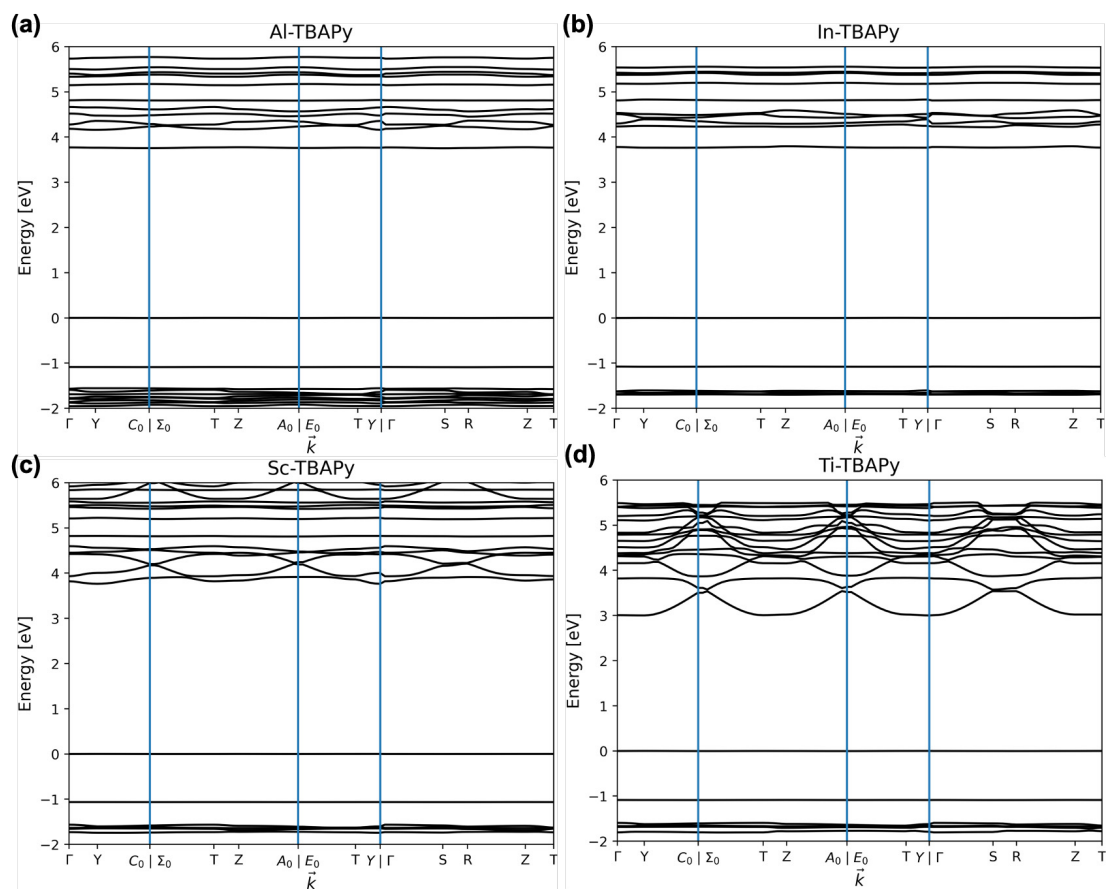


Figure A.7: Band structure calculations of the pyrene-based MOFs using PBE0 functional (CRYSTAL17) with phenyl rings rotated structure. (a) Al-TBAPy, (b) In-TBAPy, (c) Sc-TBAPy, and (d) Ti-TBAPy.

A.4 Supporting Information for Chapter 3

Synthesis of Synthetic Mineral

For the formation of our synthetic form of Jacquesdietrichite, first 250 mg $\text{CuSO}_4 \cdot 5\text{H}_2\text{O}$ dissolved in 25 mL H_2O and 123 mg NaBH_4 dissolved in 25 mL H_2O were mixed together at room temperature for 30 minutes to synthesize Cu^0 NPs. The as-synthesized Cu^0 NPs were washed with deionized water, then 20 mg of NPs were dispersed in AB water solution (10 mg AB dissolved in 10 mL H_2O). The solution was exposed to open atmosphere and stirred gently overnight at room temperature under ambient conditions, resulting in the formation of the synthetic form of Jacquesdietrichite mineral ($\text{Cu}_2[(\text{BO})(\text{OH})_2](\text{OH})_3$). The blue solid was collected and washed with Millipore water and acetone several times, then dried under air at room temperature.

AB Hydrolysis by Synthetic Mineral

The hydrolysis experiments were performed in a 25 mL Pyrex glass reactor, at room temperature under vigorous mixing. In a typical experiment, a molar ratio between the mineral and AB (the optimum conditions = 0.27) was determined and the catalyst was suspended in 9.0 mL of Millipore water. Then, the suspension was sonicated and purged with nitrogen for 20 min under gentle stirring, to remove the dissolved oxygen. In a separate vial, 6 mg of AB was dissolved in 1 mL of Millipore water and injected in the reaction solution. During the reaction, the solution was continuously stirred at a stirring speed of 750 rpm in order to eliminate any mass transfer limitation effects. When the reaction is complete, 200 μL of the gaseous product was abstracted from the head-space and analyzed by gas chromatography (PerkinElmer Clarus 480 GC, N_2 carrier gas), equipped with a thermal conductivity detector and a molecular sieve 5 Å column. The catalytic setup used for AB hydrolysis is demonstrated in Figure A.8.

Recycling experiments were performed for the synthetic mineral using the optimized molar ratio of mineral/AB = 0.27, which involved 10 catalytic runs, each for ~ 45 minutes. At the end of each cycle, the septum was first removed from the Pyrex glass reactor to remove the generated H_2 from the previous run. Then, the reactor was exposed to the open atmosphere overnight under vigorous mixing to enable the transformation of Cu^0 NPs into the synthetic mineral. To ensure the formation of the mineral at the end of each run, the blue powder occurred in the solution was collected and dried, and its PXRD pattern was recorded. The obtained mineral was again suspended into the Millipore water, purged with N_2 , then fresh AB solution was added to the reactor and the H_2 evolution was recorded.

A.4.1 Characterization Experiments

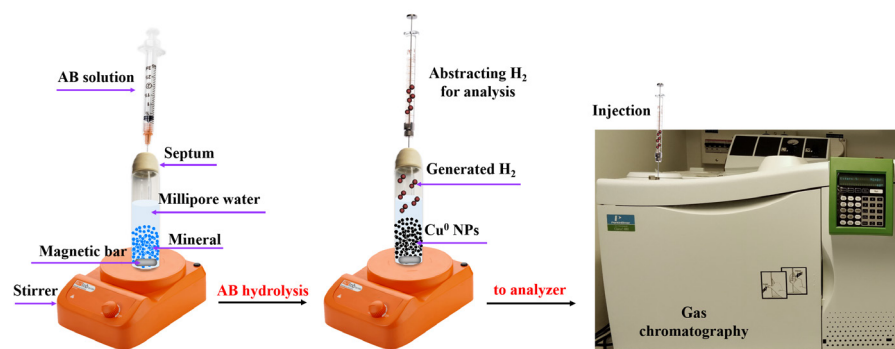


Figure A.8: The catalytic setup for AB hydrolysis.

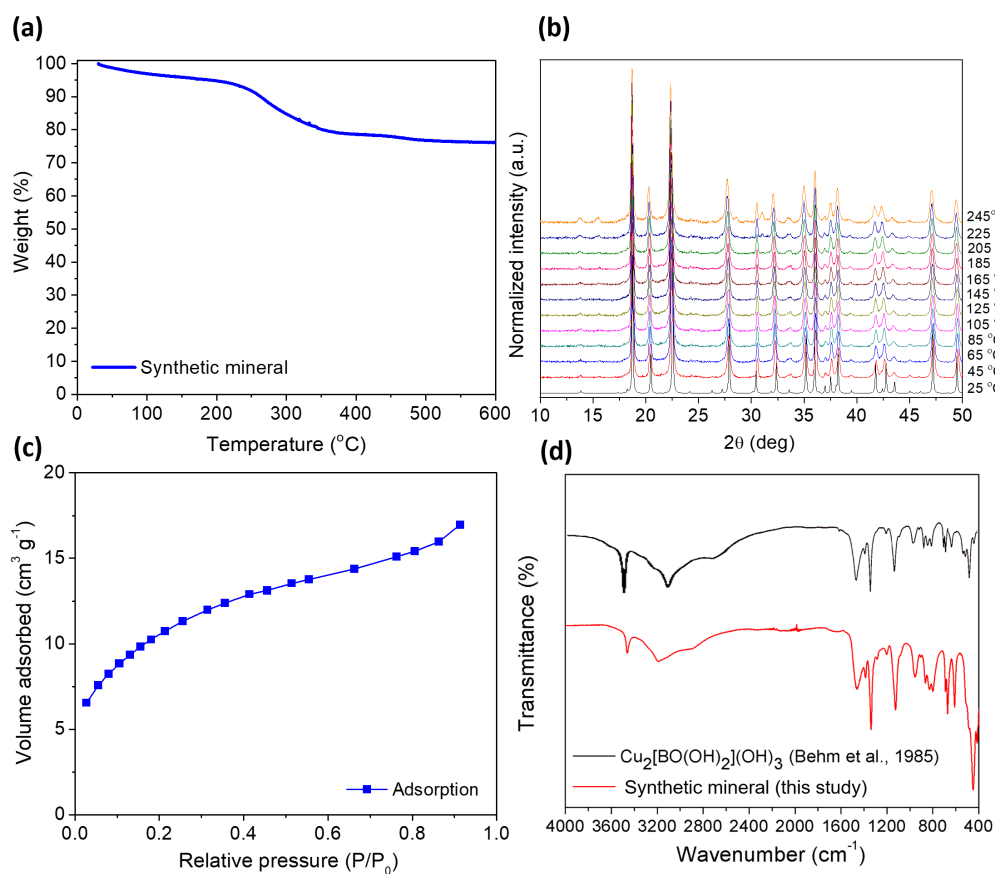


Figure A.9: (a) TGA of synthetic mineral, which shows that the structure is stable up to 245 °C. (b) Variable temperature PXRD pattern of synthetic mineral up to 245 °C. (c) N₂ adsorption isotherm of synthetic mineral, demonstrating a BET surface area of 39.24 m² g⁻¹. (d) FTIR spectra confirming the formation of the synthetic version of Jacquesdietrichite mineral.

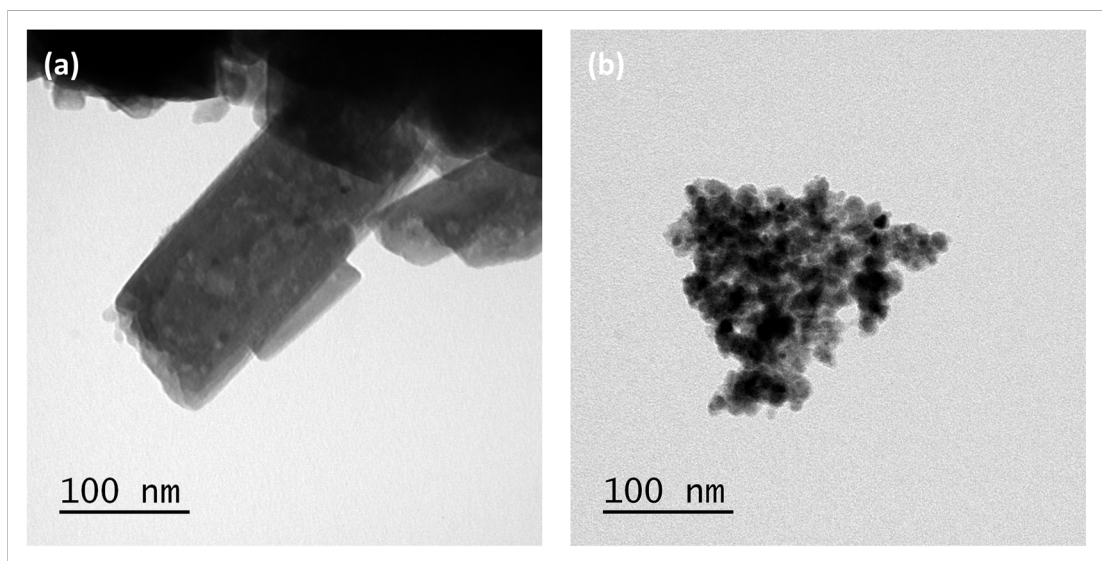
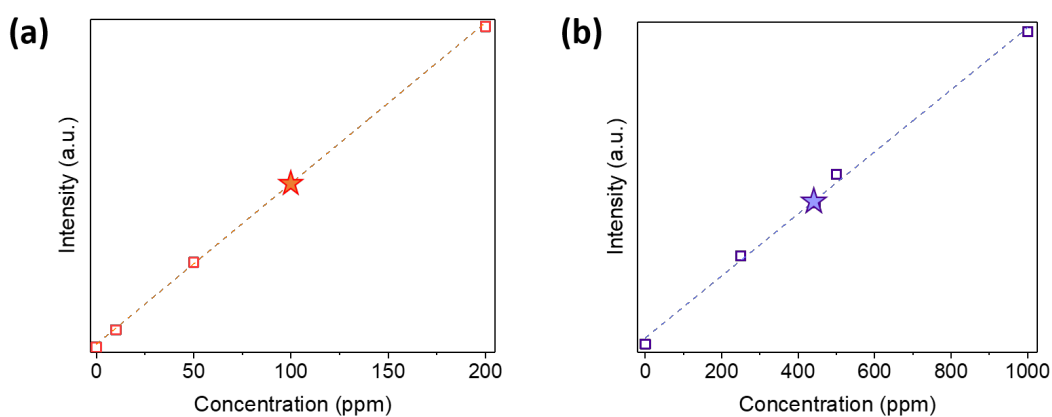


Figure A.10: (a) Bright-field TEM image of the as-synthesized synthetic mineral, showing that the mineral is composed of crystals with cuboid shapes. (b) Bright-field TEM image of *in-situ* generated Cu^0 NPs after the reaction.



	Cu in mineral (calculated)	Cu in mineral (found)	B in mineral (calculated)	B in mineral (found)
Concentration (ppm)	100	100.8	500	443.6

Figure A.11: Concentrations of (a) copper and (b) boron determined by ICP-OES measurements by analyzing synthetic mineral digested in acid. For Cu analysis, a solution was prepared by dissolving 1.88 mg synthetic mineral in dilute HNO_3 , giving a concentration of 100 ppm. For B analysis, a solution was prepared by dissolving 55.24 mg mineral in a mixture of concentrated HNO_3 and Millipore water, giving a concentration of 500 ppm. Table summarizes the calculated and experimentally obtained concentrations of Cu and B in mineral.

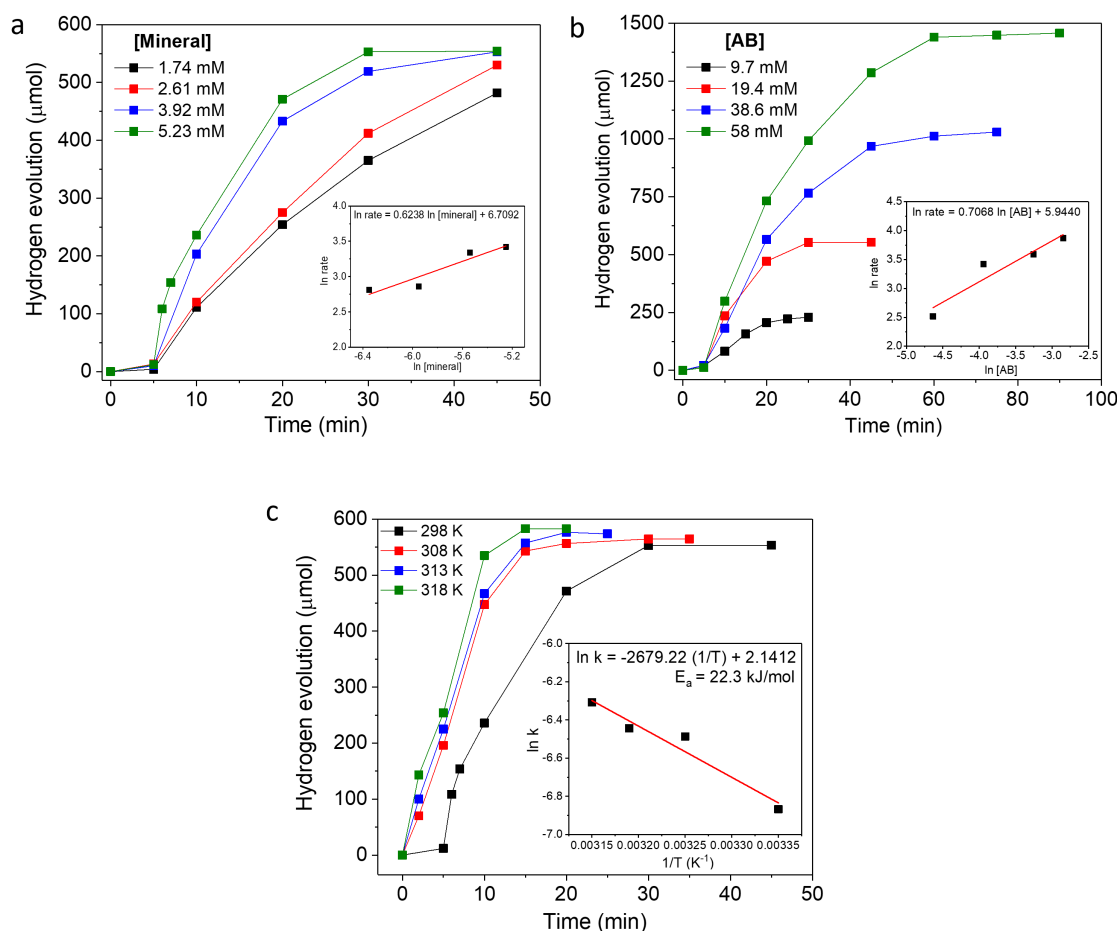


Figure A.12: H_2 evolution from AB in aqueous solution (10 mL) at 298 K containing a) fixed amount of AB (0.1944 mmol) at various mineral amounts (inset: logarithmic plots of H_2 evolution rate vs catalyst concentration), and b) fixed amount of mineral (0.052 mmol) at various AB concentrations (inset: logarithmic plots of H_2 evolution rate vs AB concentration). c) H_2 evolution rate of AB hydrolysis catalyzed by mineral at different temperatures containing fixed amount of AB and mineral (inset: Arrhenius plot ($\ln k$ vs $1/T$)).

Table A.3: Catalytic activity of some Cu-based catalysts for AB hydrolysis.

Catalyst	TOF (min^{-1})	Retained activity at reuse	Ref.
Cu/zeolite	0.78	53% at 5th use	[133]
$\text{Cu}_{0.2}\text{@Co}_{0.8}/\text{rGO}$	8.36	78% at 3th use	[192]
p(AMPS)-Cu	0.72	93% at 4th use	[193]
Annealed-RGO- $\text{Cu}_{75}\text{Pd}_{25}$	29.90	70% at 3rd run	[194]
$\text{Cu}(\text{OH})_2\text{@Co}_2\text{CO}_3(\text{OH})_2/\text{CF}$	39.72	80% at 7th run	[195]
$\text{Cu}_{0.33}\text{Fe}_{0.67}$	-	40% at 10th use	[196]
$\text{Cu}_{0.2}\text{Co}_{0.8}/\text{HPC}$	-	40% at 4th use	[197]
CoNi/RGO	19.54	68% at 5th run	[198]
$\text{Cu}_{0.3}\text{@Fe}_{0.1}\text{Co}_{0.6}$	10.50	40% at 4th use	[199]
Cu/RGO	3.61	95% at 4th use	[152]
$\text{Cu}_{0.2}\text{Ni}_{0.8}/\text{MCM-41}$	10.00	30% at 10th use	[200]
Cu@CoNi core-shell	-	35% at 5th use	[201]
Cu@ SiO_2	3.24	90% at 10th use	[151]
$\text{Cu}_{0.4}\text{@Fe}_{0.1}\text{Ni}_{0.5}$	-	90% at 5th use	[113]
CuCo_2O_4 NPs	10.90	67% at 8th use	[202]
Cu@FeCoNi/graphene	20.93	43% at 5th run	[203]
RuCu/graphene	15.90	65% at 5th use	[150]
NiCu nanorods@C nanofibers	-	100% at 6th use	[204]
$\text{Cu}_{0.5}\text{Co}_{0.5}\text{@SiO}_2$	-	90% at 10th use	[205]
Cu/h-BN	0.32	40% at 5th use	[206]
$\text{Cu}_{0.81}\text{@Mo}_{0.09}\text{Co}_{0.10}$	49.61	42% at 4th run	[139]
Cu NPs	0.06	-	[145]
Cu_2O NPs	0.18	-	[145]
Cu@ Cu_2O	0.25	90% at 9th use	[145]
CuO	0.16	30% at 2nd use	[207]
Cu NPs@ TiO_2	0.18	-	[112]
CuCl_2	0.23	-	[208]
Cu/ $\gamma\text{-Al}_2\text{O}_3$	0.27	-	[146]
Synthetic mineral	1.85	92% at 10th use	This work

A.5 Supporting Information for Chapter 4

Hydrogenation of Nitrobenzene Compounds

The hydrogenation experiments were performed in a 25.0 mL Pyrex glass reactor, at room temperature under vigorous mixing. In a typical experiment, a molar ratio between the mineral, nitroarene and AB compounds (the molar ratio for the optimized conditions: mineral/nitroarene/AB = 0.086/0.172/1, exceptionally for nimesulide, the molar ratio: mineral/nimesulide/AB = 0.086/0.051/1) was determined. First, the nitroarene and mineral were suspended in the mixture of 9 mL methanol/Millipore water solution and the glass reactor was sealed with septum. Then, the suspension was sonicated, and purged with nitrogen for 20 minutes under gentle stirring to remove the dissolved oxygen. In a separate vial, 18 mg AB was dissolved in 1 mL of Millipore water and injected in the reaction solution, resulting in 10 mL of total reaction solution ($V_{\text{methanol}} : V_{\text{H}_2\text{O}} = 1:9$ for all reactions except from nitrobenzene to aniline conversion, where $V_{\text{methanol}} : V_{\text{H}_2\text{O}} = 1:100$). A stirring speed of 750 rpm was employed during the reaction in order to eliminate any mass transfer limitation effects.

Analysis of Aniline Products

When the reaction was complete, in-situ generated Cu^0 NPs were removed from the reaction solution by centrifugation and 50 μL of reaction product was extracted from the top of the supernatant. The extracted solution was further diluted by 200 times using methanol/water solution for UV-Vis analysis. Calibration curves were constructed by preparing methanol/water solutions of each commercial aniline compound at different concentrations, to determine the yields of reaction products. The purity of products was confirmed by ^1H NMR analysis by performing the same reactions in the mixture of methanol- $\text{d}_4/\text{D}_2\text{O}$ solutions. Some part of the reaction solution was extracted and used for the ^1H NMR analysis without further treatment. The yields for the reduced drugs were calculated using ^1H NMR analysis by adding THF as the internal standard. The reaction was performed using the optimized amount of catalyst and AB, and a known amount of reactant (0.1 mmol for flutamide and 0.03 mmol for nimesulide), in 10 mL of methanol- $\text{d}_4/\text{D}_2\text{O}$ solution. After the reaction is complete, 10 μL of THF was added and the solution was stirred for 15 minutes. Then, 1 mL of the reaction solution was extracted and ^1H NMR analysis was performed. The integration of the signal of the internal standard and product was made for the calculations of the product yield. While the integration of each peak for THF represents 4 hydrogens, the peak for the product was selected as it represents 1 hydrogen.

Calibration Curves

For the calibration curves, the commercial amino compounds from Sigma Aldrich were used. Below, the construction of the calibration curve for nitrobenzene to aniline hydrogenation is explained as the example:

0.1 mmol nitrobenzene is reacted \rightarrow 0.1 mmol aniline is produced if the conversion and selectivity are 100%. Therefore, for the ideal reaction: (0.1 mmol aniline / 10.1 mL solution) = 0.0099 M aniline should be expected. Since molecular weight of aniline is 93.13 g/mol \rightarrow 0.0099 M aniline = 922 ppm aniline should be present after the hydrogenation finishes. To calculate the amount of aniline in the reaction solution, calibration curves were prepared based on different concentrations of aniline solutions (0.0002, 0.0001, 0.00005, 0.00001 and 0.000002 M).

A.5.1 UV-Vis and ^1H NMR Spectra

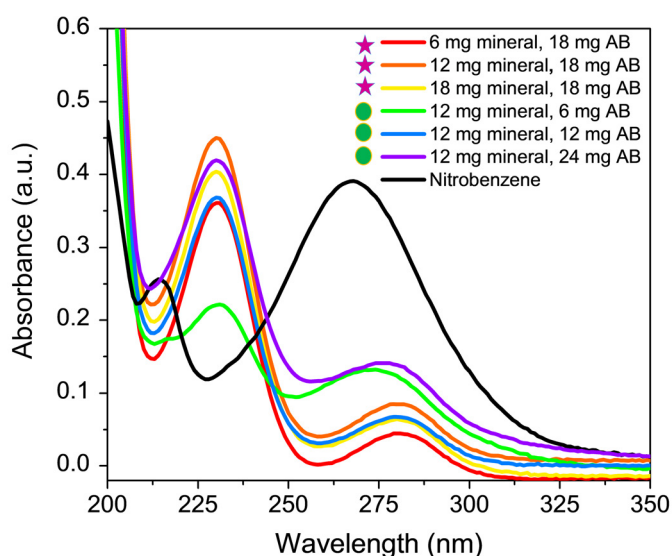


Figure A.13: Optimization of the reaction conditions by UV-Vis spectroscopy analysis. First, the mineral amount was optimized by using the same amount of AB in each set (experiments with stars), then AB amount was optimized for the determined mineral amount (experiments with circles). The yields were calculated using the calibration curves. 12 mg mineral and 18 mg AB were found as the optimum amounts for the highest yield of aniline. For all other hydrogenation reactions, these optimized amounts are used.

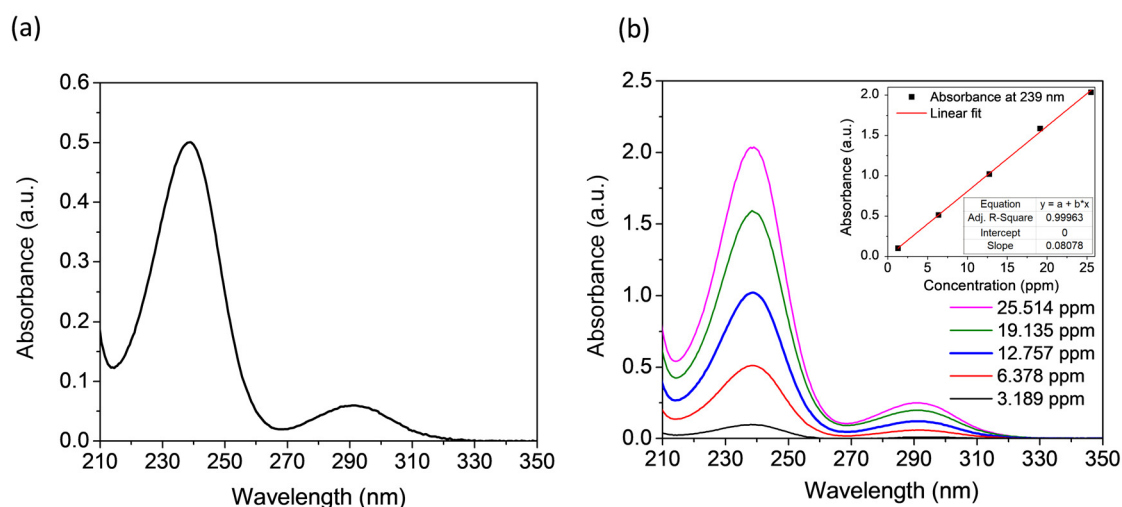


Figure A.14: (a) UV-Vis spectrum of 4-chloroaniline obtained from the reduction of 1-chloro-4-nitrobenzene at the end of 1 hour. (b) Calibration curve constructed for the determination of 4-chloroaniline yield. Inset: the absorbances of calibration solutions at different concentrations of 4-chloroaniline.

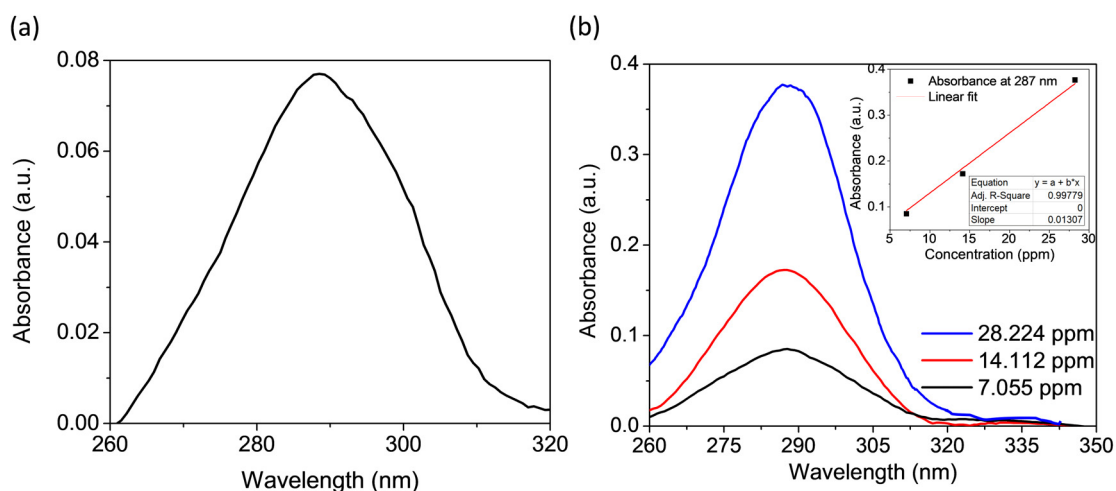


Figure A.15: (a) UV-Vis spectrum of 4-fluoroaniline obtained from the reduction of 1-fluoro-4-nitrobenzene at the end of 1 hour. (b) Calibration curve constructed for the determination of 4-fluoroaniline yield. Inset: the absorbances of calibration solutions at different concentrations of 4-fluoroaniline.

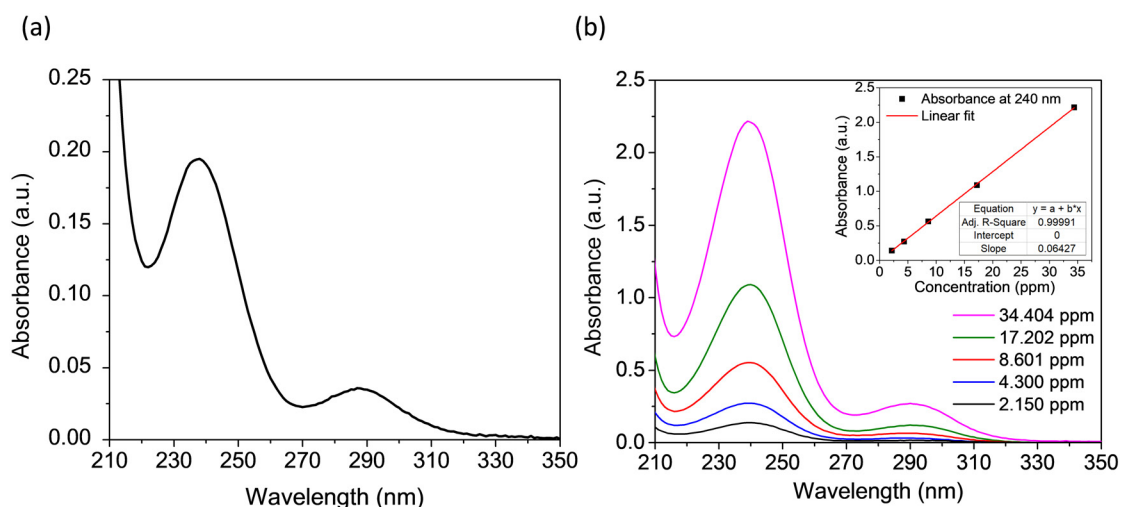


Figure A.16: (a) UV-Vis spectrum of 4-bromoaniline obtained from the reduction of 1-bromo-4-nitrobenzene at the end of 1 hour. (b) Calibration curve constructed for the determination of 4-bromoaniline yield. Inset: the absorbances of calibration solutions at different concentrations of 4-bromoaniline.

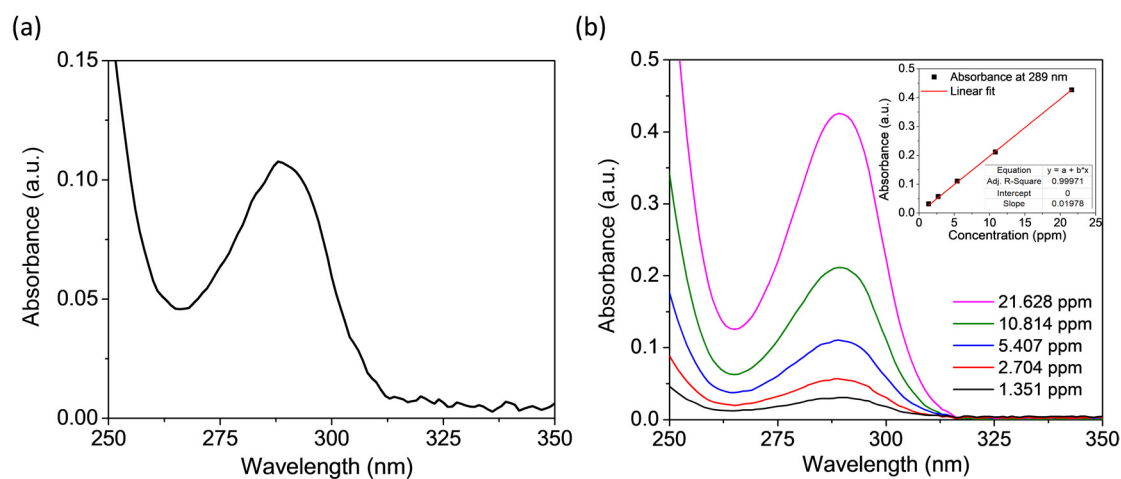


Figure A.17: (a) UV-Vis spectrum of 1,3-diaminobenzene obtained from the reduction of 1,3-dinitrobenzene at the end of 1 hour. (b) Calibration curve constructed for the determination of 1,3-diaminobenzene yield. Inset: the absorbances of calibration solutions at different concentrations of 1,3-diaminobenzene.

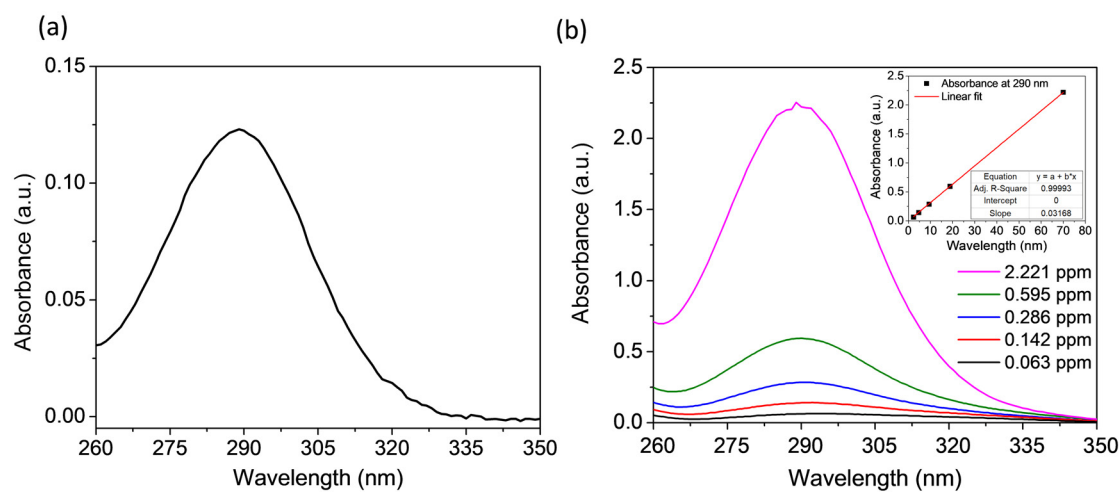


Figure A.18: (a) UV-Vis spectrum of 3-aminopyridine obtained from the reduction of 3-nitropyridine at the end of 1 hour. (b) Calibration curve constructed for the determination of 3-aminopyridine. Inset: the absorbances of calibration solutions at different concentrations of 3-aminopyridine.

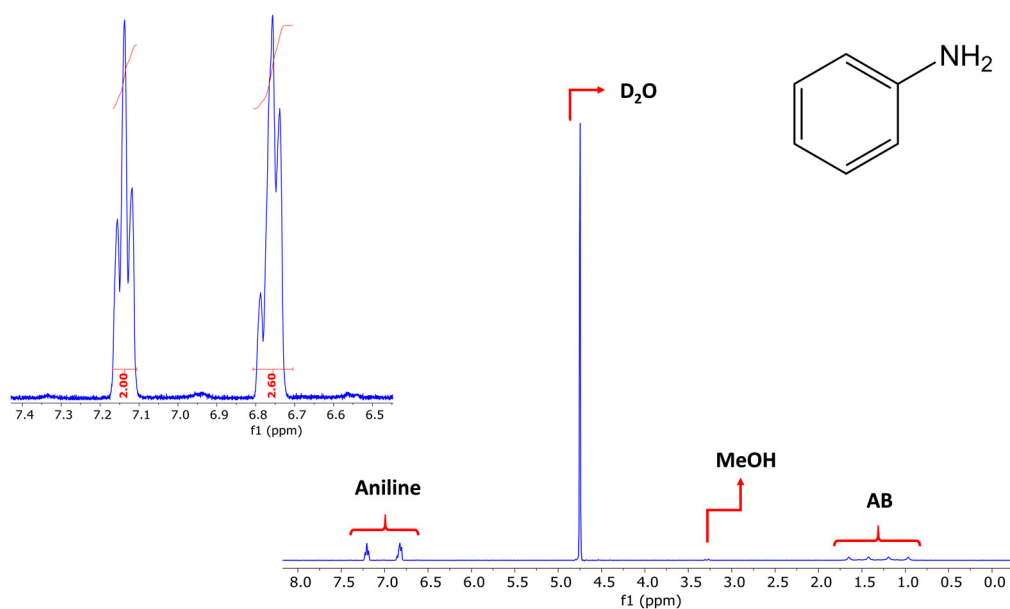


Figure A.19: ^1H NMR spectra of aniline and the assignments of the peaks. Peak assignments show that aniline was selectively observed at the end of hydrogenation reaction.

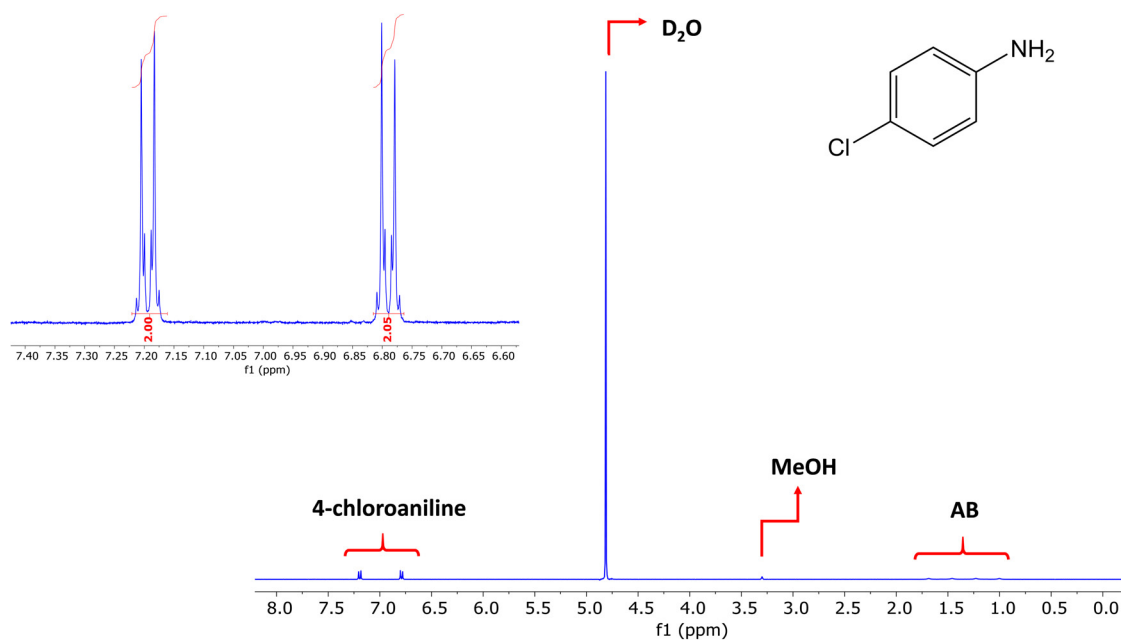


Figure A.20: ¹H NMR spectra of 4-chloroaniline and the assignments of the peaks. Peak assignments show that 4-chloroaniline was selectively observed at the end of hydrogenation reaction.

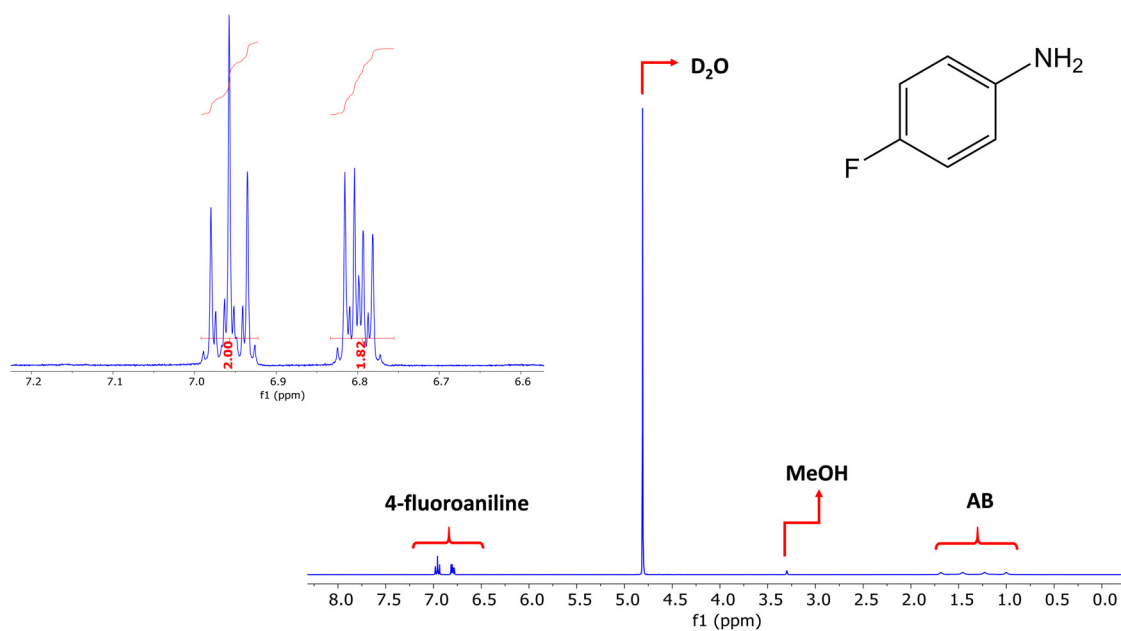


Figure A.21: ¹H NMR spectra of 4-fluoroaniline and the assignments of the peaks. Peak assignments show that 4-fluoroaniline was selectively observed at the end of hydrogenation reaction.

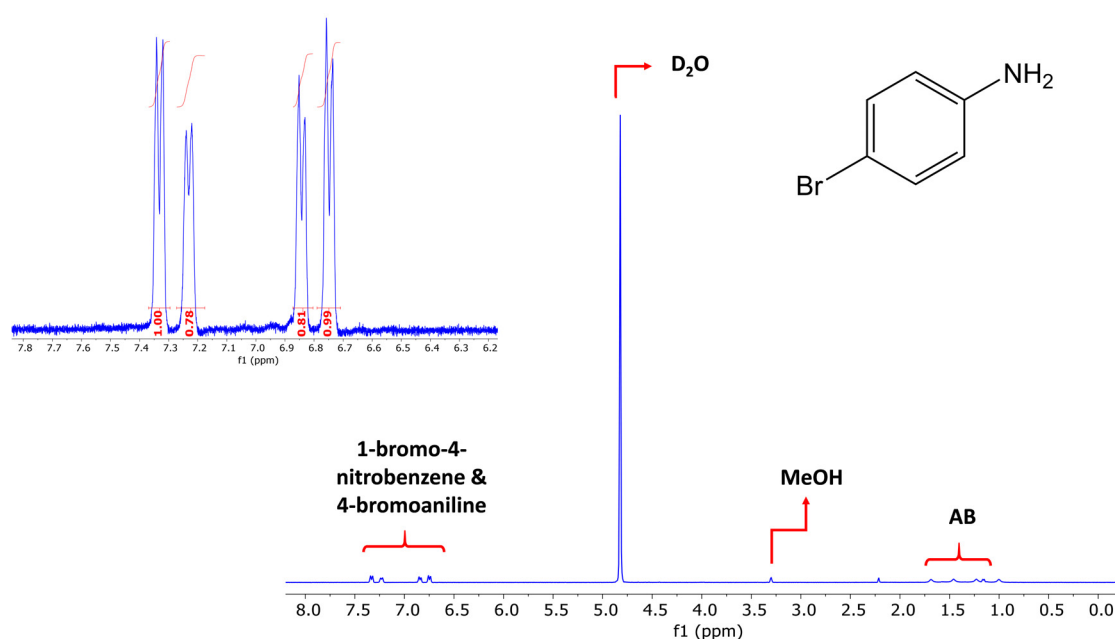


Figure A.22: ^1H NMR spectra of 4-bromoaniline and the assignments of the peaks. Peak assignments show that 4-bromoaniline was selectively observed at the end of hydrogenation reaction; however, the conversion is not complete yet.

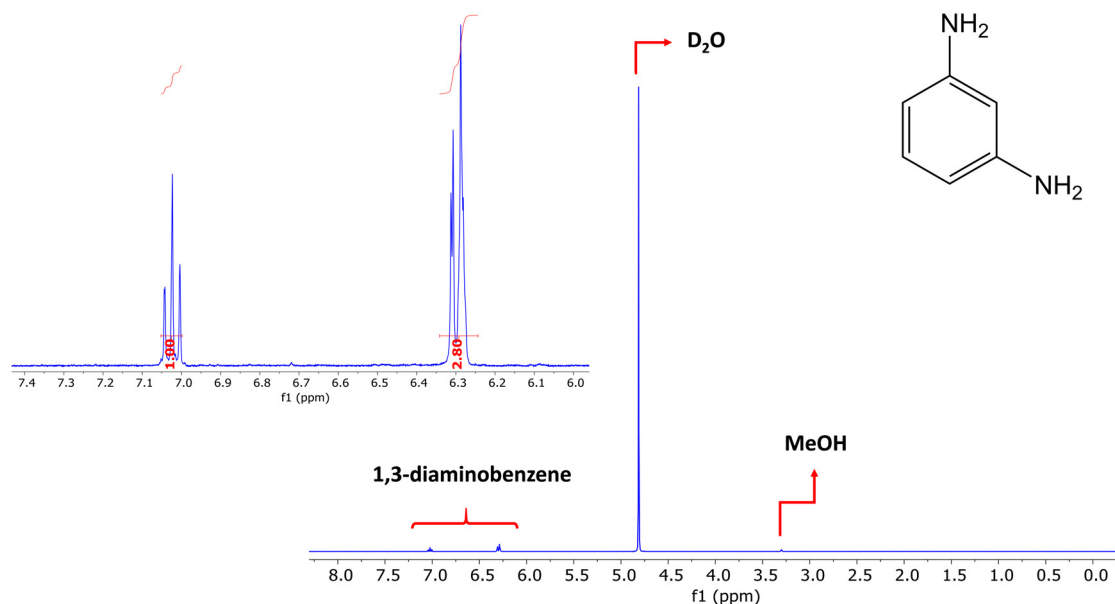


Figure A.23: ^1H NMR spectra of 1,3-diaminobenzene and the assignments of the peaks. Peak assignments show that 1,3-diaminobenzene was selectively observed at the end of hydrogenation reaction.

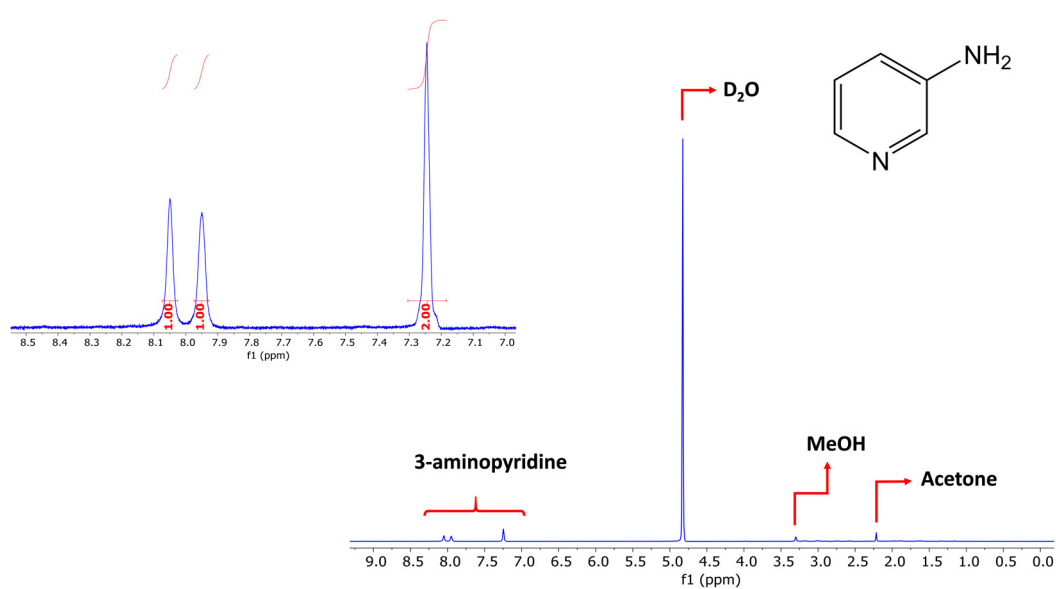


Figure A.24: ^1H NMR spectra of 3-aminopyridine and the assignments of the peaks. Peak assignments show that 3-aminopyridine was selectively observed at the end of hydrogenation reaction.

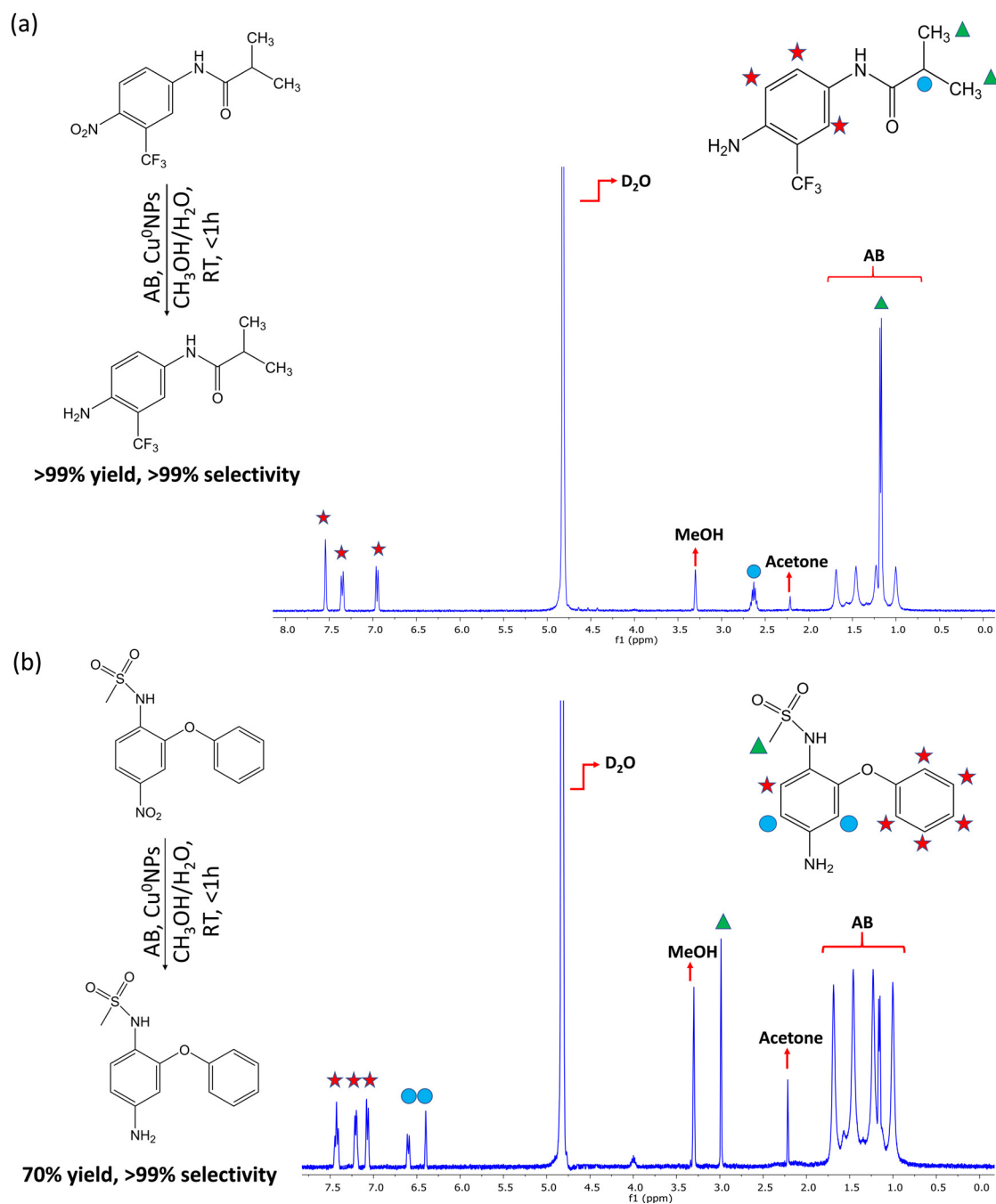


Figure A.25: (a) Hydrogenation of flutamide and the confirmation of the purity of hydrogenated product by ¹H NMR analysis with the assignment of the peaks. (b) Hydrogenation of nimesulide and the confirmation of the purity of hydrogenated product by ¹H NMR analysis with the assignment of the peaks. Acetone is an impurity in both cases, arising from the cleaning of the NMR tubes. The reactions were performed for 1 hour in a mixture of deuterated methanol and deuterated water (V_{MeOH-d4}:V_{D2O} = 1:9) at room temperature.

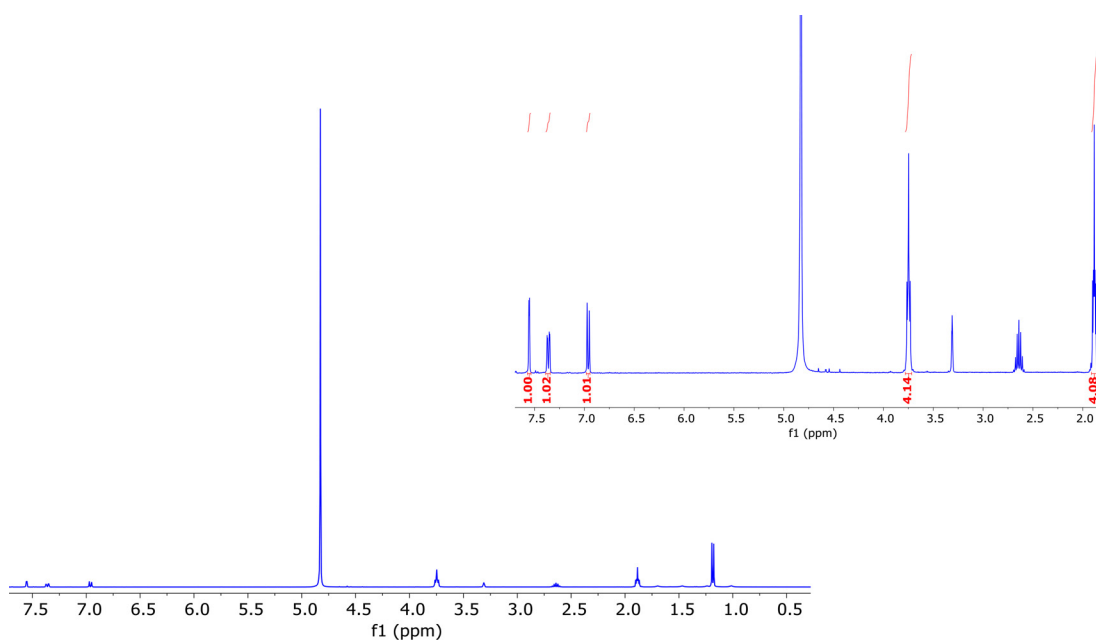


Figure A.26: ^1H NMR analysis performed for the determination of the yield of hydrogenated flutamide. 10 μL of THF was used in 10 mL of reaction solution as the internal standard.

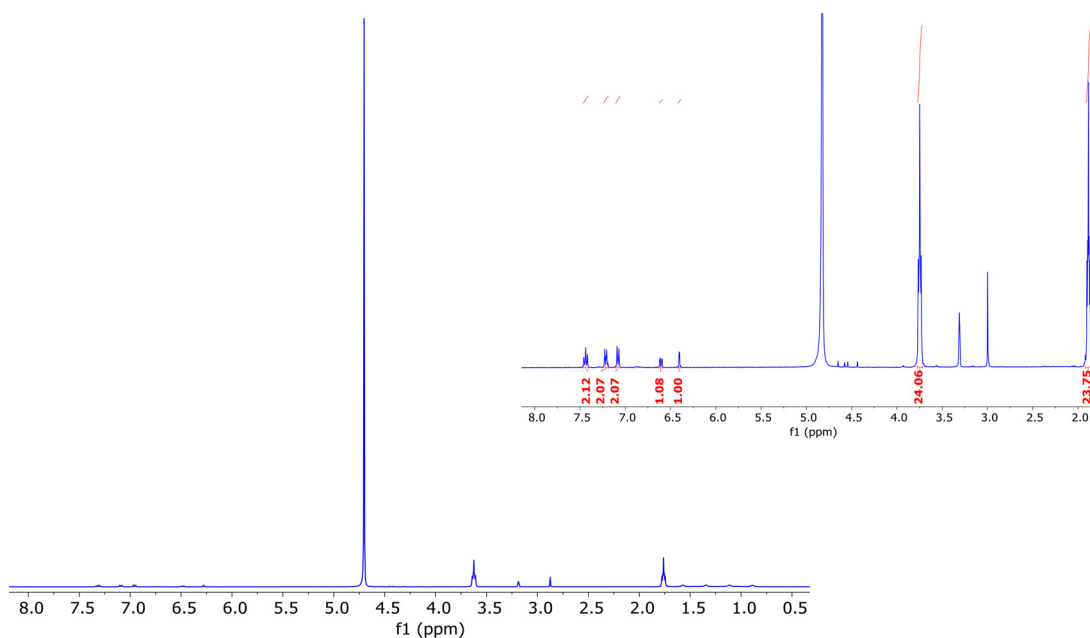


Figure A.27: ^1H NMR analysis performed for the determination of the yield of hydrogenated nimesulide. 10 μL of THF was used in 10 mL of reaction solution as the internal standard.

Appendix A. Appendices

Table A.4: Catalytic activity of some Cu-based catalysts for nitrobenzene hydrogenation.

Catalyst	Source	Time	Yield	Recycling	Ref.
Cu/NCNT	H ₂	2 h	97%	N.A.	[209]
Cu/Al ₂ O ₃	50 bar H ₂	45 min	100%	N.A.	[210]
LaCu _{0.67} Si _{1.33}	30 bar H ₂	9 h	99%	70% activity, 10th run	[211]
Cu NPs	NaBH ₄	5 h	34%	N.A.	[212]
Cu-acetate	NaBH ₄	5 h	12%	N.A.	[212]
CuCl ₂	NaBH ₄	5 h	22%	N.A.	[212]
CuBr ₂	NaBH ₄	5 h	90%	N.A.	[212]
CuI	NaBH ₄	5 h	41%	N.A.	[212]
CuO	NaBH ₄	5 h	0%	N.A.	[212]
Cu ₂ O	NaBH ₄	5 h	68%	N.A.	[212]
Cu-Meso-PANI	NaBH ₄	3 h	52%	N.A.	[213]
CP-Cu	NaBH ₄	1 h	77-86%	86% activity, 6th run	[214]
Cu@Am-Si-Fe ₃ O ₄	NaBH ₄	12 min	97%	N.A.	[215]
Cu/SiO ₂ @NiFe ₂ O ₄	NaBH ₄	1.5 h	>90%	N.A.	[216]
Cu ₂ O-Cu-CuO	NaBH ₄	4 min	100%	N.A.	[217]
Cu NPs	HCOONH ₄	11 h	86%	N.A.	[218]
Cu NPs/zeolite	2-propanol	1 h	98%	79% activity, 7th run	[219]
CuNiAlOx	Glycerol	12 h	85%	N.A.	[220]
G-Cu ₃₆ Ni ₆₄ NPs	NH ₃ BH ₃	30 min	>97%	80% activity, 10th run	[184]
CuNi@MIL-101	NH ₃ BH ₃	4 min	>99%	100% activity, 20th run	[46]
NiFe ₂ O ₄ @Cu NP	NaBH ₄	1 min	>99%	91% activity, 7th run	[221]
Cu@TiO ₂	H ₂ gas	8 h	90%	80% activity, 14 h	[222]
Cu ₂ O cubes	NH ₃ BH ₃	25 min	>99%	88% activity, 2nd run	[163]
CuFe ₂ O ₄ -G	NaBH ₄	30 min	92%	N.A.	[223]
Cu _{6/7} Co _{1/7} /Fe ₂ O ₄	NaBH ₄	25 min	99%	N.A.	[224]
Cu/Fe ₃ O ₄ NPs	NaBH ₄	1.5 h	99%	92% activity, 5th run	[225]
CuO-MnO ₂	NaBH ₄	22 min	100%	N.A.	[226]
In-situ Cu⁰ NPs	NH₃BH₃	<1 h	>90%	90% activity, 5th run	This study

Bibliography

- [1] AT Kuhn. Power for the future. *Journal of Power Sources*, 11(1-2):63–67, 1984.
- [2] John O Abe, API Popoola, Emmanueal Ajenifuja, and OM Popoola. Hydrogen energy, economy and storage: review and recommendation. *International Journal of Hydrogen Energy*, 44(29):15072–15086, 2019.
- [3] Bahman Zohuri. *Hydrogen energy: Challenges and solutions for a cleaner future*. Springer, 2018.
- [4] Puru Jena. Materials for hydrogen storage: past, present, and future. *The Journal of Physical Chemistry Letters*, 2(3):206–211, 2011.
- [5] DJ Durbin and Cecile Malardier-Jugroot. Review of hydrogen storage techniques for on board vehicle applications. *International Journal of Hydrogen Energy*, 38(34):14595–14617, 2013.
- [6] Kaveh Mazloomi and Chandima Gomes. Hydrogen as an energy carrier: Prospects and challenges. *Renewable and Sustainable Energy Reviews*, 16(5):3024–3033, 2012.
- [7] Frano Barbir. Transition to renewable energy systems with hydrogen as an energy carrier. *Energy*, 34(3):308–312, 2009.
- [8] Tiago Sinigaglia, Felipe Lewiski, Mario Eduardo Santos Martins, and Julio Cezar Mairesse Siluk. Production, storage, fuel stations of hydrogen and its utilization in automotive applications - a review. *International Journal of Hydrogen Energy*, 42(39):24597–24611, 2017.
- [9] C Koroneos, Aris Dompros, Goerge Roumbas, and Nicolas Moussiopoulos. Advantages of the use of hydrogen fuel as compared to kerosene. *Resources, Conservation and Recycling*, 44(2):99–113, 2005.
- [10] Kristiana Santos and Laurence Delina. Soaring sustainably: Promoting the uptake of sustainable aviation fuels during and post-pandemic. *Energy Research & Social Science*, 77:102074, 2021.
- [11] D Cecere, E Giacomazzi, and A Ingenito. A review on hydrogen industrial aerospace applications. *International Journal of Hydrogen Energy*, 39(20):10731–10747, 2014.
- [12] Kazunari Sasaki, Hai-Wen Li, Akari Hayashi, Junichiro Yamabe, Teppei Ogura, and Stephen M Lyth. *Hydrogen Energy Engineering*. Springer, 2016.
- [13] Jose Bellosta Von Colbe, Jose-Ramón Ares, Jussara Barale, Marcello Baricco, Craig Buckley, Giovanni Capurso, Noris Gallandat, David M Grant, Matylda N Guzik, Isaac Jacob, et al. Application of hydrides in hydrogen storage and compression: Achievements, outlook and perspectives. *international journal of hydrogen energy*, 44(15):7780–7808, 2019.
- [14] Richa Kothari, D Buddhi, and RL Sawhney. Comparison of environmental and economic aspects of various hydrogen production methods. *Renewable and Sustainable Energy Reviews*, 12(2):553–563, 2008.

Bibliography

- [15] Pavlos Nikolaidis and Andreas Poulikkas. A comparative overview of hydrogen production processes. *Renewable and Sustainable Energy Reviews*, 67:597–611, 2017.
- [16] Andreas Züttel, Arndt Remhof, Andreas Borgschulte, and Oliver Friedrichs. Hydrogen: the future energy carrier. *Philosophical Transactions of the Royal Society A: Mathematical, Physical and Engineering Sciences*, 368(1923):3329–3342, 2010.
- [17] Christopher J Quarton, Olfa Tlili, Lara Welder, Christine Mansilla, Herib Blanco, Heidi Heinrichs, Jonathan Leaver, Nouri J Samsatli, Paul Lucchese, Martin Robinius, et al. The curious case of the conflicting roles of hydrogen in global energy scenarios. *Sustainable Energy & Fuels*, 4(1):80–95, 2020.
- [18] T Bak, J Nowotny, M Rekas, and CC Sorrell. Photo-electrochemical hydrogen generation from water using solar energy. materials-related aspects. *International Journal of Hydrogen Energy*, 27(10):991–1022, 2002.
- [19] Tasneem Abbasi and SA Abbasi. ‘renewable’ hydrogen: prospects and challenges. *Renewable and Sustainable Energy Reviews*, 15(6):3034–3040, 2011.
- [20] Akira Fujishima and Kenichi Honda. Electrochemical photolysis of water at a semiconductor electrode. *Nature*, 238(5358):37–38, 1972.
- [21] Ren Ren, Huilei Zhao, Xiaoyu Sui, Xiaoru Guo, Xingkang Huang, Yale Wang, Qianqian Dong, and Junhong Chen. Exfoliated molybdenum disulfide encapsulated in a metal organic framework for enhanced photocatalytic hydrogen evolution. *Catalysts*, 9(1):89, 2019.
- [22] Akihiko Kudo and Yugo Miseki. Heterogeneous photocatalyst materials for water splitting. *Chemical Society Reviews*, 38(1):253–278, 2009.
- [23] Xiaobo Chen, Shaohua Shen, Liejin Guo, and Samuel S Mao. Semiconductor-based photocatalytic hydrogen generation. *Chemical Reviews*, 110(11):6503–6570, 2010.
- [24] N Serpone and AV Emeline. Semiconductor photocatalysis past, present, and future outlook, 2012.
- [25] B Ohtani. Photocatalysis A to Z — what we know and what we do not know in a scientific sense. *Journal of Photochemistry and Photobiology C*, 11(4):157–178, 2010.
- [26] Kazuhiro Takanabe. Photocatalytic water splitting: quantitative approaches toward photocatalyst by design. *ACS Catalysis*, 7(11):8006–8022, 2017.
- [27] Rengui Li and Can Li. Photocatalytic water splitting on semiconductor-based photocatalysts. *Advances in catalysis*, 60:1–57, 2017.
- [28] Yosuke Moriya, Tsuyoshi Takata, and Kazunari Domen. Recent progress in the development of (oxy) nitride photocatalysts for water splitting under visible-light irradiation. *Coordination Chemistry Reviews*, 257(13-14):1957–1969, 2013.
- [29] Zheng Wang, Can Li, and Kazunari Domen. Recent developments in heterogeneous photocatalysts for solar-driven overall water splitting. *Chemical Society Reviews*, 48(7):2109–2125, 2019.
- [30] K Meyer, Marco Ranocchiari, and Jeroen A van Bokhoven. Metal organic frameworks for photo-catalytic water splitting. *Energy & Environmental Science*, 8(7):1923–1937, 2015.
- [31] Nur Fajrina and Muhammad Tahir. A critical review in strategies to improve photocatalytic water splitting towards hydrogen production. *International Journal of Hydrogen Energy*, 44(2):540–577, 2019.

- [32] Vignesh Kumaravel, Muhammad Danyal Imam, Ahmed Badreldin, Rama Krishna Chava, Jeong Yeon Do, Misook Kang, and Ahmed Abdel-Wahab. Photocatalytic hydrogen production: role of sacrificial reagents on the activity of oxide, carbon, and sulfide catalysts. *Catalysts*, 9(3):276, 2019.
- [33] Mingjie Wang, Shuling Shen, Long Li, Zhihong Tang, and Junhe Yang. Effects of sacrificial reagents on photocatalytic hydrogen evolution over different photocatalysts. *Journal of Materials Science*, 52(9):5155–5164, 2017.
- [34] Sherif A Younis, Eilhann E Kwon, Muhammad Qasim, Ki-Hyun Kim, Taejin Kim, Deepak Kukkar, Xiaomin Dou, and Imran Ali. Metal-organic framework as a photocatalyst: Progress in modulation strategies and environmental/energy applications. *Progress in Energy and Combustion Science*, 81:100870, 2020.
- [35] Evangelos Tzimas, C Filiou, SD Peteves, and JB Veyret. Hydrogen storage: state-of-the-art and future perspective. *EU Commission, JRC Petten, EUR 20995EN*, 2003.
- [36] Mengxiao Li, Yunfeng Bai, Caizhi Zhang, Yuxi Song, Shangfeng Jiang, Didier Grouset, and Mingjun Zhang. Review on the research of hydrogen storage system fast refueling in fuel cell vehicle. *International Journal of Hydrogen Energy*, 44(21):10677–10693, 2019.
- [37] Dervis Emre Demirocak. Hydrogen storage technologies. In *Nanostructured Materials for Next-Generation Energy Storage and Conversion*, pages 117–142. Springer, 2017.
- [38] US Department of Energy. Doe technical targets for onboard hydrogen storage for light-duty vehicles, 2017.
- [39] Henrietta W Langmi, Jianwei Ren, Brian North, Mkhulu Mathe, and Dmitri Bessarabov. Hydrogen storage in metal-organic frameworks: a review. *Electrochimica Acta*, 128:368–392, 2014.
- [40] Jianwei Ren, Nicholas M Musyoka, Henrietta W Langmi, Mkhulu Mathe, and Shijun Liao. Current research trends and perspectives on materials-based hydrogen storage solutions: a critical review. *International Journal of Hydrogen Energy*, 42(1):289–311, 2017.
- [41] Andrew F Dalebrook, Weijia Gan, Martin Grasemann, Séverine Moret, and Gábor Laurenczy. Hydrogen storage: beyond conventional methods. *Chemical Communications*, 49(78):8735–8751, 2013.
- [42] Zhang-Hui Lu and Qiang Xu. Recent progress in boron-and nitrogen-based chemical hydrogen storage. *Functional Materials Letters*, 5(01):1230001, 2012.
- [43] Ram Ramachandran and Raghu K Menon. An overview of industrial uses of hydrogen. *International Journal of Hydrogen Energy*, 23(7):593–598, 1998.
- [44] Juan Su and Jie-Sheng Chen. Synthetic porous materials applied in hydrogenation reactions. *Microporous and Mesoporous Materials*, 237:246–259, 2017.
- [45] Dario Formenti, Francesco Ferretti, Florian Korbinian Scharnagl, and Matthias Beller. Reduction of nitro compounds using 3D-non-noble metal catalysts. *Chemical Reviews*, 119(4):2611–2680, 2018.
- [46] Ying-Hua Zhou, Qihao Yang, Yu-Zhen Chen, and Hai-Long Jiang. Low-cost CuNi@MIL-101 as an excellent catalyst toward cascade reaction: integration of ammonia borane dehydrogenation with nitroarene hydrogenation. *Chemical Communications*, 53(91):12361–12364, 2017.
- [47] Jiajia Song, Zhen-Feng Huang, Lun Pan, Ke Li, Xiangwen Zhang, Li Wang, and Ji-Jun Zou. Review on selective hydrogenation of nitroarene by catalytic, photocatalytic and electrocatalytic reactions. *Applied Catalysis B: Environmental*, 227:386–408, 2018.

- [48] Qiming Sun, Ning Wang, Tianjun Zhang, Risheng Bai, Alvaro Mayoral, Peng Zhang, Qinghong Zhang, Osamu Terasaki, and Jihong Yu. Zeolite-encaged single-atom rhodium catalysts: Highly-efficient hydrogen generation and shape-selective tandem hydrogenation of nitroarenes. *Angewandte Chemie International Edition*, 58(51):18570–18576, 2019.
- [49] Chin-Chang Yang, Miao-Sheng Chen, and Yu-Wen Chen. Hydrogen generation by hydrolysis of sodium borohydride on CoB/SiO₂ catalyst. *International Journal of Hydrogen Energy*, 36(2):1418–1423, 2011.
- [50] Haydar Göksu, Sally Fae Ho, Önder Metin, Katip Korkmaz, Adriana Mendoza Garcia, Mehmet Serdar Gültekin, and Shouheng Sun. Tandem dehydrogenation of ammonia borane and hydrogenation of nitro/nitrile compounds catalyzed by graphene-supported nipld alloy nanoparticles. *ACS Catalysis*, 4(6):1777–1782, 2014.
- [51] Jialei Du, Jie Chen, Hehuan Xia, Yiwei Zhao, Fang Wang, Hong Liu, Weijia Zhou, and Bin Wang. Commercially available CuO catalyzed hydrogenation of nitroarenes using ammonia borane as a hydrogen source. *ChemCatChem*, 2020.
- [52] F Pelin Kinik, Stavroula Kampouri, Fatmah Mish Ebrahim, Bardiya Valizadeh, and Kyriakos C Stylianou. Porous metal-organic frameworks for advanced applications. 2020.
- [53] Agnieszka Kuc, Andrey Enyashin, and G Seifert. Metal- organic frameworks: structural, energetic, electronic, and mechanical properties. *The Journal of Physical Chemistry B*, 111(28):8179–8186, 2007.
- [54] Chi-Kai Lin, Dan Zhao, Wen-Yang Gao, Zhenzhen Yang, Jingyun Ye, Tao Xu, Qingfeng Ge, Shengqian Ma, and Di-Jia Liu. Tunability of band gaps in metal–organic frameworks. *Inorganic Chemistry*, 51(16):9039–9044, 2012.
- [55] Shengjun Liu, Cheng Zhang, Yudie Sun, Qian Chen, Lifang He, Kui Zhang, Jian Zhang, Bo Liu, and Li-Feng Chen. Design of metal-organic framework-based photocatalysts for hydrogen generation. *Coordination Chemistry Reviews*, 413:213266, 2020.
- [56] Le Zeng, Xiangyang Guo, Cheng He, and Chunying Duan. Metal–organic frameworks: versatile materials for heterogeneous photocatalysis. *ACS Catalysis*, 6(11):7935–7947, 2016.
- [57] Maria Fumanal, Andres Ortega-Guerrero, Kevin Maik Jablonka, Berend Smit, and Ivano Tavernelli. Charge separation and charge carrier mobility in photocatalytic metal-organic frameworks. *Advanced Functional Materials*, 30(49):2003792, 2020.
- [58] Rong Li, Shuai-Hua Wang, Zhi-Fa Liu, Xu-Xing Chen, Yu Xiao, Fa-Kun Zheng, and Guo-Cong Guo. An azole-based metal–organic framework toward direct white-light emissions by the synergism of ligand-centered charge transfer and interligand π – π interactions. *Crystal Growth & Design*, 16(7):3969–3975, 2016.
- [59] Xing Feng, Jian-Yong Hu, Carl Redshaw, and Takehiko Yamato. Functionalization of pyrene to prepare luminescent materials—typical examples of synthetic methodology. *Chemistry - A European Journal*, 22:11898–11916, 2016.
- [60] Ritesh Haldar, Lars Heinke, and Christof Wöll. Advanced Photoresponsive Materials Using the Metal–Organic Framework Approach. *Advanced Materials*, 32(20):1905227, 2020.
- [61] A Laurent. Pyrene from coal tar. *Ann. Chim. Phys*, 66:136–137, 1837.
- [62] Teresa M Figueira-Duarte and Klaus Mullen. Pyrene-based materials for organic electronics. *Chemical Reviews*, 111:7260–7314, 2011.

- [63] Dawid Zych. Non-K Region Disubstituted Pyrenes (1, 3-, 1, 6-and 1, 8-) by (Hetero) Aryl Groups. *Molecules*, 24(14):2551, 2019.
- [64] Kyriakos C Stylianou, Romain Heck, Samantha Y Chong, John Bacsá, James TA Jones, Yaroslav Z Khimyak, Darren Bradshaw, and Matthew J Rosseinsky. A guest-responsive fluorescent 3D microporous metal-organic framework derived from a long-lifetime pyrene core. *Journal of the American Chemical Society*, 132(12):4119–4130, 2010.
- [65] F Pelin Kinik, Andres Ortega-Guerrero, Daniele Ongari, Christopher P Ireland, and Berend Smit. Pyrene-based metal organic frameworks: from synthesis to applications. *Chemical Society Reviews*, 2021.
- [66] Ashlee J Howarth, Marek B Majewski, and Michael O Wolf. Photophysical properties and applications of coordination complexes incorporating pyrene. *Coordination Chemistry Reviews*, 282:139–149, 2015.
- [67] Aaron W. Peters, Zhanyong Li, Omar K. Farha, and Joseph T. Hupp. Toward inexpensive photocatalytic hydrogen evolution: A nickel sulfide catalyst supported on a high-stability metal–organic framework. *ACS Applied Materials Interfaces*, 8(32):20675–20681, 2016. PMID: 27487409.
- [68] Xinlin Li, Jierui Yu, David J. Gosztola, H. Christopher Fry, and Pravas Deria. Wavelength-dependent energy and charge transfer in MOF: A step toward artificial porous light-harvesting system. *The Journal of American Chemical Society*, 141(42):16849–16857, 2019. PMID: 31566956.
- [69] Jierui Yu, JaeHong Park, Andrea Van Wyk, Garry Rumbles, and Pravas Deria. Excited-state electronic properties in Zr-based metal–organic frameworks as a function of a topological network. *The Journal of American Chemical Society*, 140(33):10488–10496, 2018. PMID: 30040404.
- [70] Elena Caballero-Mancebo, Boiko Cohen, Simon Smolders, Dirk E. De Vos, and Abderrazak Douhal. Unravelling why and to what extent the topology of similar Ce-based MOFs conditions their photodynamic: Relevance to photocatalysis and photonics. *Advanced Science*, 6(19):1901020, 2019.
- [71] Indrani Choudhuri and Donald G. Truhlar. Photogenerated charge separation in a CdSe nanocluster encapsulated in a metal–organic framework for improved photocatalysis. *The Journal of Physical Chemistry C*, 124(16):8504–8513, 2020.
- [72] Yejun Xiao, Yu Qi, Xiuli Wang, Xiaoyu Wang, Fuxiang Zhang, and Can Li. Visible-light-responsive 2D cadmium–organic framework single crystals with dual functions of water reduction and oxidation. *Advanced Materials*, 30(44):1803401, 2018.
- [73] Yejun Xiao, Xiangyang Guo, Junxue Liu, Lifang Liu, Fuxiang Zhang, and Can Li. Development of a bismuth-based metal-organic framework for photocatalytic hydrogen production. *Chinese Journal of Catalysis*, 40(9):1339 – 1344, 2019.
- [74] Amandine Cadiau, Nikita Kolobov, Sivaranjani Srinivasan, Maarten G Goesten, Henrik Haspel, Anastasiya V Bavykina, Mohamed R Tchalala, Partha Maity, Andrey Goryachev, Artem S Poryvaev, Mohamed Eddaoudi, Matvey V. Fedin, Omar F Mohammed, and Jorge Gascon. A titanium metal–organic framework with visible-light-responsive photocatalytic activity. *Angewandte Chemie*, 132(32):13570–13574, 2020.
- [75] Wei Wang, Xiaomin Xu, Wei Zhou, and Zongping Shao. Recent progress in metal-organic frameworks for applications in electrocatalytic and photocatalytic water splitting. *Advanced Science*, 4(4):1600371, 2017.
- [76] Fan Guo, Jin-Han Guo, Peng Wang, Yan-Shang Kang, Yi Liu, Jing Zhao, and Wei-Yin Sun. Facet-dependent photocatalytic hydrogen production of metal–organic framework NH₂-MIL-125(Ti). *Chemical Science*, 10(18):4834–4838, 2019.

- [77] Maxim A Nasalevich, Christopher H Hendon, Jara G Santaclara, Katrine Svane, Bart Van Der Linden, Sergey L Veber, Matvey V Fedin, Arjan J Houtepen, Monique A Van Der Veen, Freek Kapteijn, Aron Walsh, and Jorge Gascon. Electronic origins of photocatalytic activity in d^0 metal organic frameworks. *Scientific Reports*, 6(1):1–9, 2016.
- [78] Peter G Boyd, Arunraj Chidambaram, Enrique García-Díez, Christopher P Ireland, Thomas D Daff, Richard Bounds, Andrzej Gładysiak, Pascal Schouwink, Seyed Mohammad Moosavi, M Mercedes Maroto-Valer, Jeffrey A. Reimer, Jorge A. R. Navarro, Tom K. Woo, Susana Garcia, Kyriakos C. Stylianou, and Berend Smit. Data-driven design of metal–organic frameworks for wet flue gas CO_2 capture. *Nature*, 576(7786):253–256, 2019.
- [79] Maria Fumanal, Andres Ortega-Guerrero, Kevin Maik Jablonka, Berend Smit, and Ivano Tavernelli. Charge separation and charge carrier mobility in photocatalytic metal–organic frameworks. *Advanced Functional Materials*, 30(49):2003792, 2020.
- [80] Andres Ortega-Guerrero, Maria Fumanal, Gloria Capano, and Berend Smit. From isolated porphyrin ligands to periodic Al-PMOF: A comparative study of the optical properties using DFT/TDDFT. *The Journal of Physical Chemistry C*, 124(39):21751–21760, 2020.
- [81] Sameer Patwardhan and George C. Schatz. Theoretical investigation of charge transfer in metal organic frameworks for electrochemical device applications. *The Journal of Physical Chemistry C*, 119(43):24238–24247, 2015.
- [82] Andres Ortega-Guerrero, Maria Fumanal, Gloria Capano, Ivano Tavernelli, and Berend Smit. Insights into the electronic properties and charge transfer mechanism of a porphyrin ruthenium-based metal–organic framework. *Chemistry of Materials*, 32(10):4194–4204, 2020.
- [83] Gloria Capano, Francesco Ambrosio, Stavroula Kampouri, Kyriakos C. Stylianou, Alfredo Pasquarello, and Berend Smit. On the electronic and optical properties of metal–organic frameworks: Case study of MIL-125 and MIL-125- NH_2 . *The Journal of Physical Chemistry C*, 124(7):4065–4072, 2020.
- [84] Silvia E Braslavsky. Glossary of terms used in photochemistry, (IUPAC recommendations 2006). *Pure Applied Chemistry*, 79(3):293–465, 2007.
- [85] Stavroula Kampouri, Tu N Nguyen, Christopher P Ireland, Bardiya Valizadeh, Fatmah Mish Ebrahim, Gloria Capano, Daniele Ongari, Amber Mace, Nestor Guijarro, Kevin Sivula, et al. Photocatalytic hydrogen generation from a visible-light responsive metal–organic framework system: the impact of nickel phosphide nanoparticles. *Journal of Materials Chemistry A*, 6(6):2476–2481, 2018.
- [86] Guanzhi Wang, Qilong Sun, Yuanyuan Liu, Baibiao Huang, Ying Dai, Xiaoyang Zhang, and Xiaoyan Qin. A bismuth-based metal–organic framework as an efficient visible-light-driven photocatalyst. *Chemistry - A European Journal*, 21(6):2364–2367, 2015.
- [87] Jijie Zhang, Tianyu Bai, Hui Huang, Mei-Hui Yu, Xiaobin Fan, Ze Chang, and Xian-He Bu. Metal–organic-framework-based photocatalysts optimized by spatially separated cocatalysts for overall water splitting. *Advanced Materials*, 32(49):2004747, 2020.
- [88] Rudi Berera, Rienk van Grondelle, and John TM Kennis. Ultrafast transient absorption spectroscopy: principles and application to photosynthetic systems. *Photosynthesis research*, 101(2):105–118, 2009.
- [89] Hiroshi Miyasaka, Hiroshi Masuhara, and Noboru Mataga. Picosecond absorption spectra and relaxation processes of the excited singlet state of pyrene in solution. *Laser Chemistry*, 1(5):357–386, 1983.

- [90] Paolo Foggi, Luca Pettini, Imre Santa, Roberto Righini, and Salvatore Califano. Transient absorption and vibrational relaxation dynamics of the lowest excited singlet state of pyrene in solution. *The Journal of Physical Chemistry C*, 99(19):7439–7445, 1995.
- [91] Andrzej Gładysiak, Tu N Nguyen, Richard Bounds, Anna Zacharia, Grigorios Itskos, Jeffrey A Reimer, and Kyriakos C Stylianou. Temperature-dependent interchromophoric interaction in a fluorescent pyrene-based metal–organic framework. *Chemical science*, 10(24):6140–6148, 2019.
- [92] Tomomi Kawakami, Masafumi Koga, Hikaru Sotome, and Hiroshi Miyasaka. Ultrafast capture of electrons ejected by photoionization leading to the formation of a charge-separated state at a high energy level. *Physical Chemistry Chemical Physics*, 22(31):17472–17481, 2020.
- [93] Xiao-Mei Cheng, Xiao-Yao Dao, Shi-Qing Wang, Jing Zhao, and Wei-Yin Sun. Enhanced photocatalytic CO₂ reduction activity over NH₂-MIL-125(Ti) by facet regulation. *ACS Catalysis*, 11:650–658, 2020.
- [94] Yitong Han, Min Liu, Keyan Li, Yi Zuo, Yingxu Wei, Shutao Xu, Guoliang Zhang, Chunshan Song, Zongchao Zhang, and Xinwen Guo. Facile synthesis of morphology and size-controlled zirconium metal–organic framework uio-66: the role of hydrofluoric acid in crystallization. *CrystEngComm*, 17(33):6434–6440, 2015.
- [95] Mali H Rosnes, Fredrik S Nesse, Martin Opitz, and Pascal DC Dietzel. Morphology control in modulated synthesis of metal-organic framework cpo-27. *Microporous and Mesoporous Materials*, 275:207–213, 2019.
- [96] Fan Guo, Sizhuo Yang, Yi Liu, Peng Wang, Jier Huang, and Wei-Yin Sun. Size engineering of metal–organic framework MIL-101(Cr)–Ag hybrids for photocatalytic CO₂ reduction. *ACS Catalysis*, 9(9):8464–8470, 2019.
- [97] Lin Liu, Zheng-Bo Han, Shi-Ming Wang, Da-Qiang Yuan, and Seik Weng Ng. Robust molecular bowl-based metal–organic frameworks with open metal sites: Size modulation to increase the catalytic activity. *Inorganic Chemistry*, 54(8):3719–3721, 2015.
- [98] Wei-Ning Wang, Woo-Jin An, Balavinayagam Ramalingam, Somik Mukherjee, Dariusz M Niedzwiedzki, Shubhra Gangopadhyay, and Pratim Biswas. Size and structure matter: enhanced CO₂ photoreduction efficiency by size-resolved ultrafine Pt nanoparticles on TiO₂ single crystals. *J. Am. Chem. Soc.*, 134(27):11276–11281, 2012.
- [99] Yali Liu, Pengfei Gao, Chengzhi Huang, and Yuanfang Li. Shape-and size-dependent catalysis activities of iron-terephthalic acid metal-organic frameworks. *Science China Chemistry*, 58(10):1553–1560, 2015.
- [100] Tetsuo Umegaki, Jun-Min Yan, Xin-Bo Zhang, Hiroshi Shioyama, Nobuhiro Kuriyama, and Qiang Xu. Boron-and nitrogen-based chemical hydrogen storage materials. *International Journal of Hydrogen Energy*, 34(5):2303–2311, 2009.
- [101] Sheldon G Shore and Robert W Parry. The crystalline compound ammonia-borane, H₃NBH₃. *Journal of the American Chemical Society*, 77(22):6084–6085, 1955.
- [102] Umit B Demirci. About the technological readiness of the H₂ generation by hydrolysis of B(-N)-H compounds. *Energy Technology*, 6(3):470–486, 2018.
- [103] Kasper T Møller, Torben R Jensen, Etsuo Akiba, and Hai-wen Li. Hydrogen - a sustainable energy carrier. *Progress in Natural Science: Materials International*, 27(1):34–40, 2017.
- [104] Wen-Wen Zhan, Qi-Long Zhu, and Qiang Xu. Dehydrogenation of ammonia borane by metal nanoparticle catalysts. *ACS Catalysis*, 6(10):6892–6905, 2016.

Bibliography

- [105] Ceren Yüksel Alpaydın, Senem Karahan Gülbay, and C Ozgur Colpan. A review on the catalysts used for hydrogen production from ammonia borane. *International Journal of Hydrogen Energy*, 45(5):3414–3434, 2020.
- [106] Qilu Yao, Zhang-Hui Lu, Wei Huang, Xiangshu Chen, and Jia Zhu. High Pt-like activity of the Ni–Mo/graphene catalyst for hydrogen evolution from hydrolysis of ammonia borane. *Journal of Materials Chemistry A*, 4(22):8579–8583, 2016.
- [107] Cheng Du, Qiang Ao, Nan Cao, Lan Yang, Wei Luo, and Gongzhen Cheng. Facile synthesis of monodisperse ruthenium nanoparticles supported on graphene for hydrogen generation from hydrolysis of ammonia borane. *International Journal of Hydrogen Energy*, 40(18):6180–6187, 2015.
- [108] Qilu Yao, Zhang-Hui Lu, Yushuai Jia, Xiangshu Chen, and Xin Liu. In situ facile synthesis of Rh nanoparticles supported on carbon nanotubes as highly active catalysts for H₂ generation from NH₃BH₃ hydrolysis. *International Journal of Hydrogen Energy*, 40(5):2207–2215, 2015.
- [109] Wenyao Chen, Jian Ji, Xuezhi Duan, Gang Qian, Ping Li, Xinggui Zhou, De Chen, and Weikang Yuan. Unique reactivity in Pt/CNT catalyzed hydrolytic dehydrogenation of ammonia borane. *Chemical Communications*, 50(17):2142–2144, 2014.
- [110] Jianmin Chen, Zhang-Hui Lu, Yuqing Wang, Xiangshu Chen, and Lei Zhang. Magnetically recyclable ag/SiO₂–CoFe₂O₄ nanocomposite as a highly active and reusable catalyst for H₂ production. *International Journal of Hydrogen Energy*, 40(14):4777–4785, 2015.
- [111] Yalçın Tonbul, Serdar Akbayrak, and Saim Özkar. Palladium (0) nanoparticles supported on ceria: highly active and reusable catalyst in hydrogen generation from the hydrolysis of ammonia borane. *International Journal of Hydrogen Energy*, 41(26):11154–11162, 2016.
- [112] Murat Kaya, Mehmet Zahmakiran, Saim Ozkar, and Murvet Volkan. Copper(0) nanoparticles supported on silica-coated cobalt ferrite magnetic particles: cost effective catalyst in the hydrolysis of ammonia-borane with an exceptional reusability performance. *ACS Applied Materials & Interfaces*, 4(8):3866–3873, 2012.
- [113] Hong-Li Wang, Jun-Min Yan, Zhi-Li Wang, and Qing Jiang. One-step synthesis of Cu@FeNi core-shell nanoparticles: Highly active catalyst for hydrolytic dehydrogenation of ammonia borane. *International Journal of Hydrogen Energy*, 37(13):10229–10235, 2012.
- [114] Zhi-Li Wang, Jun-Min Yan, Hong-Li Wang, and Qing Jiang. Self-protective cobalt nanocatalyst for long-time recycle application on hydrogen generation by its free metal-ion conversion. *Journal of Power Sources*, 243:431–435, 2013.
- [115] Jun-Min Yan, Xin-Bo Zhang, Song Han, Hiroshi Shioyama, and Qiang Xu. Iron-nanoparticle-catalyzed hydrolytic dehydrogenation of ammonia borane for chemical hydrogen storage. *Angewandte Chemie*, 120(12):2319–2321, 2008.
- [116] Murat Rakap. PVP-stabilized Ru–Rh nanoparticles as highly efficient catalysts for hydrogen generation from hydrolysis of ammonia borane. *Journal of Alloys and Compounds*, 649:1025–1030, 2015.
- [117] Xiaojing Li, Chunmei Zeng, and Guangyin Fan. Magnetic RuCo nanoparticles supported on two-dimensional titanium carbide as highly active catalysts for the hydrolysis of ammonia borane. *International Journal of Hydrogen Energy*, 40(30):9217–9224, 2015.
- [118] Kunzhou Yang, Liqun Zhou, Xing Xiong, Menglin Ye, Ling Li, and Qinghua Xia. Ru–CuCo nanoparticles supported on MIL-101 as a novel highly efficient catalysts for the hydrolysis of ammonia borane. *Microporous and Mesoporous Materials*, 225:1–8, 2016.

- [119] Yusuke Yamada, Kentaro Yano, and Shunichi Fukuzumi. Catalytic application of shape-controlled Cu_2O particles protected by Co_3O_4 nanoparticles for hydrogen evolution from ammonia borane. *Energy & Environmental Science*, 5(1):5356–5363, 2012.
- [120] Cheng-Yun Peng, Lei Kang, Shuang Cao, Yong Chen, Zhe-Shuai Lin, and Wen-Fu Fu. Nanostructured Ni_2P as a robust catalyst for the hydrolytic dehydrogenation of ammonia–borane. *Angewandte Chemie*, 127(52):15951–15955, 2015.
- [121] Zi-Cheng Fu, Yong Xu, Sharon Lai-Fung Chan, Wei-Wei Wang, Fang Li, Fei Liang, Yong Chen, Zhe-Shuai Lin, Wen-Fu Fu, and Chi-Ming Che. Highly efficient hydrolysis of ammonia borane by anion ($-\text{OH}$, F^- , Cl^-)-tuned interactions between reactant molecules and cop nanoparticles. *Chemical Communications*, 53(4):705–708, 2017.
- [122] Melanie C Denney, Vincent Pons, Travis J Hebden, D Michael Heinekey, and Karen I Goldberg. Efficient catalysis of ammonia borane dehydrogenation. *Journal of the American Chemical Society*, 128(37):12048–12049, 2006.
- [123] Kenta Yoshida, Camino Gonzalez-Arellano, Rafael Luque, and Pratibha L Gai. Efficient hydrogenation of carbonyl compounds using low-loaded supported copper nanoparticles under microwave irradiation. *Applied Catalysis A: General*, 379(1-2):38–44, 2010.
- [124] Jose A Rodriguez, Jaime Evans, Jesús Graciani, Joon-Bum Park, Ping Liu, Jan Hrbeek, and Javier Fdez Sanz. High water-gas shift activity in TiO_2 (110) supported Cu and Au nanoparticles: role of the oxide and metal particle size. *The Journal of Physical Chemistry C*, 113(17):7364–7370, 2009.
- [125] Bibek Jyoti Borah, Dipanka Dutta, Partha Pratim Saikia, Nabin Chandra Barua, and Dipak Kumar Dutta. Stabilization of Cu(0)-nanoparticles into the nanopores of modified montmorillonite: An implication on the catalytic approach for “click” reaction between azides and terminal alkynes. *Green Chemistry*, 13(12):3453–3460, 2011.
- [126] Ju Hyun Kim and Young Keun Chung. Copper nanoparticle-catalyzed cross-coupling of alkyl halides with Grignard reagents. *Chemical Communications*, 49(94):11101–11103, 2013.
- [127] Xiaoning Guo, Caihong Hao, Guoqiang Jin, Huai-Yong Zhu, and Xiang-Yun Guo. Copper nanoparticles on graphene support: an efficient photocatalyst for coupling of nitroaromatics in visible light. *Angewandte Chemie International Edition*, 53(7):1973–1977, 2014.
- [128] Derrick Mott, Jeffrey Galkowski, Lingyan Wang, Jin Luo, and Chuan-Jian Zhong. Synthesis of size-controlled and shaped copper nanoparticles. *Langmuir*, 23(10):5740–5745, 2007.
- [129] Yanfei Wang, Ankush V Biradar, Gang Wang, Krishna K Sharma, Cole T Duncan, Sylvie Rangan, and Tewodros Asefa. Controlled synthesis of water-dispersible faceted crystalline copper nanoparticles and their catalytic properties. *Chemistry—A European Journal*, 16(35):10735–10743, 2010.
- [130] Mingshang Jin, Guannan He, Hui Zhang, Jie Zeng, Zhaoxiong Xie, and Younan Xia. Shape-controlled synthesis of copper nanocrystals in an aqueous solution with glucose as a reducing agent and hexadecylamine as a capping agent. *Angewandte Chemie International Edition*, 50(45):10560–10564, 2011.
- [131] M Lakshmi Kantam, V Swarna Jaya, M Jaya Lakshmi, B Ramachandra Reddy, BM Choudary, and SK Bhargava. Alumina supported copper nanoparticles for aziridination and cyclopropanation reactions. *Catalysis Communications*, 8(12):1963–1968, 2007.
- [132] Pillaiyar Puthiaraj and Wha-Seung Ahn. Synthesis of copper nanoparticles supported on a microporous covalent triazine polymer: an efficient and reusable catalyst for o-arylation reaction. *Catalysis Science & Technology*, 6(6):1701–1709, 2016.

Bibliography

- [133] Mehmet Zahmakıran, Feyyaz Durap, and Saim Özkır. Zeolite confined copper (0) nanoclusters as cost-effective and reusable catalyst in hydrogen generation from the hydrolysis of ammonia-borane. *International Journal of Hydrogen Energy*, 35(1):187–197, 2010.
- [134] Michael Grouchko, Alexander Kamyshny, and Shlomo Magdassi. Formation of air-stable copper–silver core–shell nanoparticles for inkjet printing. *Journal of Materials Chemistry*, 19(19):3057–3062, 2009.
- [135] Tomohisa Yamauchi, Yasunori Tsukahara, Takao Sakata, Hirotaro Mori, Takeshi Yanagida, Tomoji Kawai, and Yuji Wada. Magnetic Cu–Ni (core–shell) nanoparticles in a one-pot reaction under microwave irradiation. *Nanoscale*, 2(4):515–523, 2010.
- [136] Guangjun Zhou, Mengkai Lu, and Zhongsen Yang. Aqueous synthesis of copper nanocubes and bimetallic copper/palladium core-shell nanostructures. *Langmuir*, 22(13):5900–5903, 2006.
- [137] Sebastiano Campisi, Marco Schiavoni, Carine Edith Chan-Thaw, and Alberto Villa. Untangling the role of the capping agent in nanocatalysis: recent advances and perspectives. *Catalysts*, 6(12):185, 2016.
- [138] Xiangyu Meng, Lan Yang, Nan Cao, Cheng Du, Kai Hu, Jun Su, Wei Luo, and Gongzhen Cheng. Graphene-supported trimetallic core–shell Cu@CoNi nanoparticles for catalytic hydrolysis of amine borane. *ChemPlusChem*, 79(2):325–332, 2014.
- [139] Cong Wang, Hongli Wang, Zhili Wang, Xiaojun Li, Yue Chi, Minggang Wang, Dawei Gao, and Zhankui Zhao. Mo remarkably enhances catalytic activity of Cu@MoCo core-shell nanoparticles for hydrolytic dehydrogenation of ammonia borane. *International Journal of Hydrogen Energy*, 43(15):7347–7355, 2018.
- [140] Mohammad Mahdi Najafpour, Monika Fekete, Davood Jafarian Sedigh, Eva-Mari Aro, Robert Carpentier, Julian J Eaton-Rye, Hiroshi Nishihara, Jian-Ren Shen, Suleyman I Allakhverdiev, and Leone Spiccia. Damage management in water-oxidizing catalysts: from photosystem II to nanosized metal oxides. *ACS Catalysis*, 5(3):1499–1512, 2015.
- [141] Manoj B Gawande, Anandarup Goswami, François-Xavier Felpin, Tewodros Asefa, Xiaoxi Huang, Rafael Silva, Xiaoxin Zou, Radek Zboril, and Rajender S Varma. Cu and Cu-based nanoparticles: synthesis and applications in catalysis. *Chemical Reviews*, 116(6):3722–3811, 2016.
- [142] Morris D Argyle and Calvin H Bartholomew. Heterogeneous catalyst deactivation and regeneration: a review. *Catalysts*, 5(1):145–269, 2015.
- [143] Byoung-Hoon Lee, Sunghak Park, Minho Kim, Arun K Sinha, Seong Chan Lee, Euiyeon Jung, Woo Je Chang, Kug-Seung Lee, Jeong Hyun Kim, Sung-Pyo Cho, Hyungjun Kim, Ki Tae Nam, and Taeghwan Hyeon. Reversible and cooperative photoactivation of single-atom Cu/TiO₂ photocatalysts. *Nature Materials*, 18(6):620–626, 2019.
- [144] Anthony R Kampf and Georges Favreau. Jacquesdietrichite, Cu₂[BO(OH)₂](OH)₃, a new mineral from the Tachgagalt mine, Morocco: Description and crystal structure. *European Journal of Mineralogy*, 16(2):361–366, 2004.
- [145] Suresh Babu Kalidindi, Udishnu Sanyal, and Balaji R Jagirdar. Nanostructured Cu and Cu@Cu₂O core shell catalysts for hydrogen generation from ammonia–borane. *Physical Chemistry Chemical Physics*, 10(38):5870–5874, 2008.
- [146] Qiang Xu and Manish Chandra. Catalytic activities of non-noble metals for hydrogen generation from aqueous ammonia–borane at room temperature. *Journal of Power Sources*, 163(1):364–370, 2006.

- [147] Dahlang Tahir and Sven Tougaard. Electronic and optical properties of Cu, CuO and Cu₂O studied by electron spectroscopy. *Journal of Physics: Condensed Matter*, 24(17):175002, 2012.
- [148] Kun Feng, Jun Zhong, Binhua Zhao, Hui Zhang, Lai Xu, Xuhui Sun, and Shuit-Tong Lee. Cu_xCo_{1-x}O nanoparticles on graphene oxide as a synergistic catalyst for high-efficiency hydrolysis of ammonia–borane. *Angewandte Chemie*, 128(39):12129–12133, 2016.
- [149] Prathik Roy, Arun Prakash Periasamy, Chi-Te Liang, and Huan-Tsung Chang. Synthesis of graphene-ZnO-Au nanocomposites for efficient photocatalytic reduction of nitrobenzene. *Environmental Science & Technology*, 47(12):6688–6695, 2013.
- [150] Lan Wen, Jun Su, Xiaojun Wu, Ping Cai, Wei Luo, and Gongzhen Cheng. Ruthenium supported on MIL-96: an efficient catalyst for hydrolytic dehydrogenation of ammonia borane for chemical hydrogen storage. *International Journal of Hydrogen Energy*, 39(30):17129–17135, 2014.
- [151] Qilu Yao, Zhang-Hui Lu, Zhujun Zhang, Xiangshu Chen, and Yaqian Lan. One-pot synthesis of core-shell Cu@SiO₂ nanospheres and their catalysis for hydrolytic dehydrogenation of ammonia borane and hydrazine borane. *Scientific Reports*, 4(1):1–8, 2014.
- [152] Yuwen Yang, Zhang-Hui Lu, Yujuan Hu, Zhujun Zhang, Weimei Shi, Xiangshu Chen, and Tingting Wang. Facile in situ synthesis of copper nanoparticles supported on reduced graphene oxide for hydrolytic dehydrogenation of ammonia borane. *RSC Advances*, 4(27):13749–13752, 2014.
- [153] Julia Patzsch, Benedict Berg, and Jonathan Z Bloh. Kinetics and optimization of the photocatalytic reduction of nitrobenzene. *Frontiers in Chemistry*, 7:289, 2019.
- [154] Jaime Wisniak and Miriam Klein. Reduction of nitrobenzene to aniline. *Industrial & Engineering Chemistry Product Research and Development*, 23(1):44–50, 1984.
- [155] Hari K Kadam and Santosh G Tilve. Advancement in methodologies for reduction of nitroarenes. *RSC Advances*, 5(101):83391–83407, 2015.
- [156] Klaus Weissmermel and Hans-Jürgen Arpe. *Industrial Organic Chemistry*. John Wiley & Sons, 2008.
- [157] Xinyu Li, Lianghao Song, Daowei Gao, Baotao Kang, Huaiqing Zhao, Cuncheng Li, Xun Hu, and Guozhu Chen. Tandem catalysis of ammonia borane dehydrogenation and phenylacetylene hydrogenation catalyzed by CeO₂ nanotube/Pd@MIL-53 (al). *Chemistry—A European Journal*, 2020.
- [158] Matthew J Gilkey and Bingjun Xu. Heterogeneous catalytic transfer hydrogenation as an effective pathway in biomass upgrading. *ACS Catalysis*, 6(3):1420–1436, 2016.
- [159] Caroline E Hartmann, Václav Jurčík, Olivier Songis, and Catherine SJ Cazin. Tandem ammonia borane dehydrogenation/alkene hydrogenation mediated by [Pd(NHC)(PR₃)](NHC= N-heterocyclic carbene) catalysts. *Chemical Communications*, 49(10):1005–1007, 2013.
- [160] Shaomin Fu, Nan-Yu Chen, Xufang Liu, Zhihui Shao, Shu-Ping Luo, and Qiang Liu. Ligand-controlled cobalt-catalyzed transfer hydrogenation of alkynes: Stereodivergent synthesis of z- and e-alkenes. *Journal of the American Chemical Society*, 138(27):8588–8594, 2016.
- [161] Zhihui Shao, Shaomin Fu, Mufeng Wei, Shaolin Zhou, and Qiang Liu. Mild and selective cobalt-catalyzed chemodivergent transfer hydrogenation of nitriles. *Angewandte Chemie*, 128(47):14873–14877, 2016.

Bibliography

- [162] Songlei Li, Gen Li, Wei Meng, and Haifeng Du. A frustrated Lewis pair catalyzed asymmetric transfer hydrogenation of imines using ammonia borane. *Journal of the American Chemical Society*, 138(39):12956–12962, 2016.
- [163] Mahesh Madasu, Chi-Fu Hsia, Sourav Rej, and Michael H Huang. Cu₂O pseudomorphic conversion to Cu crystals for diverse nitroarene reduction. *ACS Sustainable Chemistry & Engineering*, 6(8):11071–11077, 2018.
- [164] Jia-Lu Sun, Yu-Zhen Chen, Bang-Di Ge, Jin-Hua Li, and Guo-Ming Wang. Three-shell Cu@Co@Ni nanoparticles stabilized with a metal–organic framework for enhanced tandem catalysis. *ACS Applied Materials & Interfaces*, 11(1):940–947, 2018.
- [165] Tian-Jian Zhao, Ya-Nan Zhang, Kai-Xue Wang, Juan Su, Xiao Wei, and Xin-Hao Li. General transfer hydrogenation by activating ammonia-borane over cobalt nanoparticles. *RSC Advances*, 5(124):102736–102740, 2015.
- [166] Önder Metin, Adriana Mendoza-Garcia, Diğdem Dalmızrak, Mehmet Serdar Gültekin, and Shouheng Sun. FePd alloy nanoparticles assembled on reduced graphene oxide as a catalyst for selective transfer hydrogenation of nitroarenes to anilines using ammonia borane as a hydrogen source. *Catalysis Science & Technology*, 6(15):6137–6143, 2016.
- [167] Eleni Vasilikogiannaki, Charis Gryparis, Vasiliki Kotzabasaki, Ioannis N Lykakis, and Manolis Stratakis. Facile reduction of nitroarenes into anilines and nitroalkanes into hydroxylamines via the rapid activation of ammonia borane complex by supported gold nanoparticles. *Advanced Synthesis & Catalysis*, 355(5):907–911, 2013.
- [168] Qihao Yang, Yu-Zhen Chen, Zhiyong U Wang, Qiang Xu, and Hai-Long Jiang. One-pot tandem catalysis over Pd@MIL-101: boosting the efficiency of nitro compound hydrogenation by coupling with ammonia borane dehydrogenation. *Chemical Communications*, 51(52):10419–10422, 2015.
- [169] Chao Yu, Xuefeng Guo, Mengqi Shen, Bo Shen, Michelle Muzzio, Zhouyang Yin, Qing Li, Zheng Xi, Junrui Li, Christopher T Seto, et al. Maximizing the catalytic activity of nanoparticles through monolayer assembly on nitrogen-doped graphene. *Angewandte Chemie International Edition*, 57(2):451–455, 2018.
- [170] L Petrov, K Kumbilieva, and N Kirkov. Kinetic model of nitrobenzene hydrogenation to aniline over industrial copper catalyst considering the effects of mass transfer and deactivation. *Applied Catalysis*, 59(1):31–43, 1990.
- [171] Rex N Brogden and Stephen P Clissold. Flutamide. *Drugs*, 38(2):185–203, 1989.
- [172] You-Sin Jian, Ching-Wen Chen, Chih-An Lin, Hsiu-Ping Yu, Hua-Yang Lin, Ming-Yuan Liao, Shu-Huan Wu, Yan-Fu Lin, and Ping-Shan Lai. Hyaluronic acid–nimesulide conjugates as anticancer drugs against cD44-overexpressing hT-29 colorectal cancer in vitro and in vivo. *International Journal of Nanomedicine*, 12:2315, 2017.
- [173] Tanusri Dey, Paramita Chatterjee, Abir Bhattacharya, Sarbani Pal, and Alok K Mukherjee. Three nimesulide derivatives: synthesis, ab initio structure determination from powder X-ray diffraction, and quantitative analysis of molecular surface electrostatic potential. *Crystal Growth & Design*, 16(3):1442–1452, 2016.
- [174] Dario Formenti, Francesco Ferretti, Christoph Topf, Annette-Enrica Surkus, Marga-Martina Pohl, Joerg Radnik, Matthias Schneider, Kathrin Junge, Matthias Beller, and Fabio Ragaini. Co-based heterogeneous catalysts from well-defined α -diimine complexes: Discussing the role of nitrogen. *Journal of Catalysis*, 351:79–89, 2017.
- [175] Rajenahally V Jagadeesh, Annette-Enrica Surkus, Henrik Junge, Marga-Martina Pohl, Jörg Radnik, Jabor Rabeah, Heming Huan, Volker Schünemann, Angelika Brückner, and Matthias Beller. Nanoscale Fe₂O₃-based catalysts for selective hydrogenation of nitroarenes to anilines. *Science*, 342(6162):1073–1076, 2013.

- [176] Scott A May. Flow chemistry, continuous processing, and continuous manufacturing: a pharmaceutical perspective. *Journal of Flow Chemistry*, 7(3-4):137–145, 2017.
- [177] Li Fu, Wen Cai, Aiwu Wang, and Yuhong Zheng. Photocatalytic hydrogenation of nitrobenzene to aniline over tungsten oxide-silver nanowires. *Materials Letters*, 142:201–203, 2015.
- [178] Weiming Wu, Rui Lin, Lijuan Shen, Ruowen Liang, Rusheng Yuan, and Ling Wu. Highly efficient visible-light-induced photocatalytic hydrogenation of nitrobenzene to aniline in water. *RSC Advances*, 3(27):10894–10899, 2013.
- [179] Manohar A Bhosale, Divya R Chenna, and Bhalchandra M Bhanage. Ultrasound assisted synthesis of gold nanoparticles as an efficient catalyst for reduction of various nitro compounds. *ChemistrySelect*, 2(3):1225–1231, 2017.
- [180] Yoshimasa Okazaki, Kotaro Yamashita, Hiroyuki Ishii, Masato Sudo, and Minoru Tsuchitani. Potential of neurotoxicity after a single oral dose of 4-bromo-, 4-chloro-, 4-fluoro-or 4-iodoaniline in rats. *Journal of Applied Toxicology: An International Journal*, 23(5):315–322, 2003.
- [181] MM Telkar, JM Nadgeri, CV Rode, and RV Chaudhari. Role of a co-metal in bimetallic Ni–Pt catalyst for hydrogenation of *m*-dinitrobenzene to *m*-phenylenediamine. *Applied Catalysis A: General*, 295(1):23–30, 2005.
- [182] Dongwei Wei, Hui Li, Ya-Nan Li, and Jing Zhu. Effect of temperature on the solubility of 3-aminopyridine in binary ethanol + toluene solvent mixtures. *Fluid Phase Equilibria*, 316:132–134, 2012.
- [183] Maria Michela Dell’Anna, Simona Intini, Giuseppe Romanazzi, Antonino Rizzuti, Cristina Leonelli, Ferruccio Piccinni, and Piero Mastroilli. Polymer supported palladium nanocrystals as efficient and recyclable catalyst for the reduction of nitroarenes to anilines under mild conditions in water. *Journal of Molecular Catalysis A: Chemical*, 395:307–314, 2014.
- [184] Chao Yu, Jiaju Fu, Michelle Muzzio, Tunli Shen, Dong Su, Junjie Zhu, and Shouheng Sun. CuNi nanoparticles assembled on graphene for catalytic methanolysis of ammonia borane and hydrogenation of nitro/nitrile compounds. *Chemistry of Materials*, 29(3):1413–1418, 2017.
- [185] Upendra Sharma, Praveen Kumar, Neeraj Kumar, Vishal Kumar, and Bikram Singh. Highly chemo-and regioselective reduction of aromatic nitro compounds catalyzed by recyclable copper (II) as well as cobalt (II) phthalocyanines. *Advanced Synthesis & Catalysis*, 352(11-12):1834–1840, 2010.
- [186] Timothy C Wang, Nicolaas A Vermeulen, In Soo Kim, Alex BF Martinson, J Fraser Stoddart, Joseph T Hupp, and Omar K Farha. Scalable synthesis and post-modification of a mesoporous metal-organic framework called NU-1000. *Nature Protocols*, 11(1):149–162, 2016.
- [187] Alan A Coelho. Topas and topas-academic: an optimization program integrating computer algebra and crystallographic objects written in C++. *Journal of Applied Crystallography*, 51(1):210–218, 2018.
- [188] Roberto Dovesi, Alessandro Erba, Roberto Orlando, Claudio M. Zicovich-Wilson, Bartolomeo Civalleri, Lorenzo Maschio, Michel Rérat, Silvia Casassa, Jacopo Baima, Simone Salustro, and Bernard Kirtman. Quantum-mechanical condensed matter simulations with crystal. *WIREs Comput. Mol. Sci.*, 8(4):e1360, 2018.
- [189] Yoyo Hinuma, Giovanni Pizzi, Yu Kumagai, Fumiyasu Oba, and Isao Tanaka. Band structure diagram paths based on crystallography. *Computational Materials Science*, 128:140–184, 2017.

- [190] Thomas D. Kühne, Marcella Iannuzzi, Mauro Del Ben, Vladimir V. Rybkin, Patrick Seewald, Frederick Stein, Teodoro Laino, Rustam Z. Khaliullin, Ole Schütt, Florian Schiffmann, Dorothea Golze, Jan Wilhelm, Sergey Chulkov, Mohammad Hossein Bani-Hashemian, Valéry Weber, Urban Borštnik, Mathieu Taillefumier, Alice Shoshana Jakobovits, Alfio Lazzaro, Hans Pabst, Tiziano Müller, Robert Schade, Manuel Guidon, Samuel Andermatt, Nico Holmberg, Gregory K. Schenter, Anna Hehn, Augustin Bussy, Fabian Belleflamme, Gloria Tabacchi, Andreas Glöß, Michael Lass, Iain Bethune, Christopher J. Mundy, Christian Plessl, Matt Watkins, Joost VandeVondele, Matthias Krack, and Jürg Hutter. CP2K: An electronic structure and molecular dynamics software package - quickstep: Efficient and accurate electronic structure calculations. *The Journal of Chemical Physics*, 152(19):194103, 2020.
- [191] Keith T. Butler, Christopher H. Hendon, and Aron Walsh. Electronic chemical potentials of porous metal–organic frameworks. *The Journal of American Chemical Society*, 136(7):2703–2706, 2014.
- [192] Yeshuang Du, Nan Cao, Lan Yang, Wei Luo, and Gongzhen Cheng. One-step synthesis of magnetically recyclable rGO supported Cu@Co core–shell nanoparticles: highly efficient catalysts for hydrolytic dehydrogenation of ammonia borane and methylamine borane. *New Journal of Chemistry*, 37(10):3035–3042, 2013.
- [193] Ozgur Ozay, Erk Inger, Nahit Aktas, and Nurettin Sahiner. Hydrogen production from ammonia borane via hydrogel template synthesized Cu, Ni, Co composites. *International Journal of Hydrogen Energy*, 36(14):8209–8216, 2011.
- [194] Kübra Güngörmez and Önder Metin. Composition-controlled catalysis of reduced graphene oxide supported CuPd alloy nanoparticles in the hydrolytic dehydrogenation of ammonia borane. *Applied Catalysis A: General*, 494:22–28, 2015.
- [195] Jianmei Wang, Xiao Ma, Wenrong Yang, Xuping Sun, and Jingquan Liu. Self-supported Cu(OH)₂@Co₂CO₃(OH)₂ core–shell nanowire array as a robust catalyst for ammonia-borane hydrolysis. *Nanotechnology*, 28(4):045606, 2016.
- [196] Zhang-Hui Lu, Jinping Li, Aili Zhu, Qilu Yao, Wei Huang, Ruyi Zhou, Rongfei Zhou, and Xiangshu Chen. Catalytic hydrolysis of ammonia borane via magnetically recyclable copper iron nanoparticles for chemical hydrogen storage. *International Journal of Hydrogen Energy*, 38(13):5330–5337, 2013.
- [197] Haixia Wang, Limin Zhou, Mo Han, Zhanliang Tao, Fangyi Cheng, and Jun Chen. CuCo nanoparticles supported on hierarchically porous carbon as catalysts for hydrolysis of ammonia borane. *Journal of Alloys and Compounds*, 651:382–388, 2015.
- [198] Yuwen Yang, Fei Zhang, Hualan Wang, Qilu Yao, Xiangshu Chen, and Zhang-Hui Lu. Catalytic hydrolysis of ammonia borane by cobalt nickel nanoparticles supported on reduced graphene oxide for hydrogen generation. *Journal of Nanomaterials*, 2014, 2014.
- [199] Fangyuan Qiu, Yiling Dai, Li Li, Changchang Xu, Yanan Huang, Chengcheng Chen, Yijing Wang, Lifang Jiao, and Huatang Yuan. Synthesis of Cu@FeCo core–shell nanoparticles for the catalytic hydrolysis of ammonia borane. *International Journal of Hydrogen Energy*, 39(1):436–441, 2014.
- [200] Zhang-Hui Lu, Jinping Li, Gang Feng, Qilu Yao, Fei Zhang, Ruyi Zhou, Duanjian Tao, Xiangshu Chen, and Zhiqiang Yu. Synergistic catalysis of MCM-41 immobilized Cu–Ni nanoparticles in hydrolytic dehydrogenation of ammonia borane. *International Journal of Hydrogen Energy*, 39(25):13389–13395, 2014.
- [201] Hao Zhang, Xiaofeng Wang, Chengcheng Chen, Cuihua An, Yanan Xu, Yanan Huang, Qiuyu Zhang, Yijing Wang, Lifang Jiao, and Huatang Yuan. Facile synthesis of Cu@CoNi core-shell nanoparticles composites for the catalytic hydrolysis of ammonia borane. *International Journal of Hydrogen Energy*, 40(36):12253–12261, 2015.

- [202] Quanbing Liu, Shengjie Zhang, Jinyun Liao, Kejun Feng, Yuying Zheng, Bruno G Pollet, and Hao Li. CuCo₂O₄ nanoplate film as a low-cost, highly active and durable catalyst towards the hydrolytic dehydrogenation of ammonia borane for hydrogen production. *Journal of Power Sources*, 355:191–198, 2017.
- [203] Xiangyu Meng, Shuangshi Li, Bingquan Xia, Lan Yang, Nan Cao, Jun Su, Man He, Wei Luo, and Gongzhen Cheng. Decoration of graphene with tetrametallic Cu@FeCoNi core-shell nanoparticles for catalytic hydrolysis of amine boranes. *RSC Advances*, 4(62):32817–32825, 2014.
- [204] Ayman Yousef, Nasser AM Barakat, Mohamed El-Newehy, and Hak Yong Kim. Chemically stable electrospun NiCu nanorods@carbon nanofibers for highly efficient dehydrogenation of ammonia borane. *International Journal of Hydrogen Energy*, 37(23):17715–17723, 2012.
- [205] Qilu Yao, Zhang-Hui Lu, Yuqing Wang, Xiangshu Chen, and Gang Feng. Synergetic catalysis of non-noble bimetallic Cu–Co nanoparticles embedded in SiO₂ nanospheres in hydrolytic dehydrogenation of ammonia borane. *The Journal of Physical Chemistry C*, 119(25):14167–14174, 2015.
- [206] Yawei Wu, Xin Wu, Qiuwen Liu, Caijin Huang, and Xiaoqing Qiu. Magnetically recyclable Ni@h-BN composites for efficient hydrolysis of ammonia borane. *International Journal of Hydrogen Energy*, 42(25):16003–16011, 2017.
- [207] Yusuke Yamada, Kentaro Yano, Qiang Xu, and Shunichi Fukuzumi. Cu/Co₃O₄ nanoparticles as catalysts for hydrogen evolution from ammonia borane by hydrolysis. *The Journal of Physical Chemistry C*, 114(39):16456–16462, 2010.
- [208] Suresh Babu Kalidindi, M Indirani, and Balaji R Jagirdar. First row transition metal ion-assisted ammonia-borane hydrolysis for hydrogen generation. *Inorganic Chemistry*, 47(16):7424–7429, 2008.
- [209] Gurpreet Kour, Monika Gupta, B Vishwanathan, and K Thirunavukkarasu. Cu/NCNTs: a new high temperature technique to prepare a recyclable nanocatalyst for four component pyridine derivative synthesis and nitroarenes reduction. *New Journal of Chemistry*, 40(10):8535–8542, 2016.
- [210] Alexey L Nuzhdin, Ekaterina A Artiukha, Galina A Bukhtiyarova, Elizaveta A Derevyannikova, and Valerii I Bukhtiyarov. Synthesis of secondary amines by reductive amination of aldehydes with nitroarenes over supported copper catalysts in a flow reactor. *Catalysis Communications*, 102:108–113, 2017.
- [211] Tian-Nan Ye, Yangfan Lu, Jiang Li, Takuya Nakao, Hongsheng Yang, Tomofumi Tada, Masaaki Kitano, and Hideo Hosono. Copper-based intermetallic electride catalyst for chemoselective hydrogenation reactions. *Journal of the American Chemical Society*, 139(47):17089–17097, 2017.
- [212] Hari K Kadam and Santosh G Tilve. Copper (II) bromide as a procatalyst for in situ preparation of active Cu nanoparticles for reduction of nitroarenes. *RSC Advances*, 2(14):6057–6060, 2012.
- [213] Mahesh Tumma and Rajendra Srivastava. Transition metal nanoparticles supported on mesoporous polyaniline catalyzed reduction of nitroaromatics. *Catalysis Communications*, 37:64–68, 2013.
- [214] Jaqueline F de Souza, Gabriela T da Silva, and André R Fajardo. Chitosan-based film supported copper nanoparticles: A potential and reusable catalyst for the reduction of aromatic nitro compounds. *Carbohydrate Polymers*, 161:187–196, 2017.
- [215] RK Sharma, Yukti Monga, and Aditi Puri. Magnetically separable silica@Fe₃O₄ core-shell supported nano-structured copper (II) composites as a versatile catalyst for the reduction of nitroarenes in aqueous medium at room temperature. *Journal of Molecular Catalysis A: Chemical*, 393:84–95, 2014.

Bibliography

- [216] Mira V Parmekar and AV Salker. Room temperature complete reduction of nitroarenes over a novel $\text{Cu}/\text{SiO}_2/\text{NiFe}_2\text{O}_4$ nano-catalyst in an aqueous medium—a kinetic and mechanistic study. *RSC Advances*, 6(110):108458–108467, 2016.
- [217] Anup Kumar Sasmal, Soumen Dutta, and Tarasankar Pal. A ternary $\text{Cu}_2\text{O}-\text{Cu}-\text{CuO}$ nanocomposite: a catalyst with intriguing activity. *Dalton Transactions*, 45(7):3139–3150, 2016.
- [218] Amit Saha and Brindaban Ranu. Highly chemoselective reduction of aromatic nitro compounds by copper nanoparticles/ammonium formate. *The Journal of Organic Chemistry*, 73(17):6867–6870, 2008.
- [219] Thirumeni Subramanian and Kasi Pitchumani. Selective reduction of nitroarenes by using zeolite-supported copper nanoparticles with 2-propanol as a sustainable reducing agent. *ChemCatChem*, 4(12):1917–1921, 2012.
- [220] Xingchao Dai, Xinjiang Cui, Hangkong Yuan, Youquan Deng, and Feng Shi. Cooperative transformation of nitroarenes and biomass-based alcohols catalyzed by CuNiAlOx . *RSC Advances*, 5(11):7970–7975, 2015.
- [221] Behzad Zeynizadeh, Iman Mohammadzadeh, Zahra Shokri, and Seyed Ali Hosseini. Synthesis and characterization of $\text{NiFe}_2\text{O}_4/\text{Cu}$ nanoparticles as a magnetically recoverable catalyst for reduction of nitroarenes to arylamines with NaBH_4 . *Journal of Colloid and Interface Science*, 500:285–293, 2017.
- [222] Itika Kainthla, Venkata Ramesh Babu Gurram, Jayesh T Bhanushali, Seetha Rama Rao Kamaraju, Rangappa S Keri, Suresh W Gosavi, Arvind H Jadhav, and Bhari Mallanna Nagaraja. In situ generation of Cu^0 supported on TiO_2 aerogel as a catalyst for the vapour phase hydrogenation of nitrobenzene to aniline. *Catalysis Letters*, 148(9):2891–2900, 2018.
- [223] Haiyan Zhang, Shutao Gao, Ningzhao Shang, Chun Wang, and Zhi Wang. Copper ferrite-graphene hybrid: a highly efficient magnetic catalyst for chemoselective reduction of nitroarenes. *RSC Advances*, 4(59):31328–31332, 2014.
- [224] Haiyan Zhang, Ying Zhao, Weihua Liu, Shutao Gao, Ningzhao Shang, Chun Wang, and Zhi Wang. Preparation of magnetically separable $\text{Cu}_{6/7}\text{Co}_{1/7}\text{Fe}_2\text{O}_4$ -graphene catalyst and its application in selective reduction of nitroarenes. *Catalysis Communications*, 59:161–165, 2015.
- [225] S Mohammad Sajadi, Mahmoud Nasrollahzadeh, and Mehdi Maham. Aqueous extract from seeds of *silybum marianum* l. as a green material for preparation of the $\text{Cu}/\text{Fe}_3\text{O}_4$ nanoparticles: a magnetically recoverable and reusable catalyst for the reduction of nitroarenes. *Journal of Colloid and Interface Science*, 469:93–98, 2016.
- [226] Jaya Pal, Chanchal Mondal, Anup Kumar Sasmal, Mainak Ganguly, Yuichi Negishi, and Tarasankar Pal. Account of nitroarene reduction with size- and facet-controlled $\text{CuO}-\text{MnO}_2$ nanocomposites. *ACS Applied Materials & Interfaces*, 6(12):9173–9184, 2014.

Fatma Pelin Uran (Kinik)

Chemical Engineer - Doctoral Researcher

E-mail: pelin_kinik@hotmail.com

LinkedIn: <https://ch.linkedin.com/in/fpelinkinik/>



EDUCATION

PhD in Chemical Sciences and Engineering, EPFL

2017 – 2021

MSc in Chemical and Biological Engineering, Koç University

2015 – 2017

BSc in Chemical Engineering, Istanbul Technical University

2010 – 2015

EXPERIENCE

EPFL Laboratory of Molecular Simulation, *PhD Thesis*

2017 – 2021

Hydrogen Release from Chemical Hydrides and Its Utilization

- Explored hydrogen release from ammonia borane through heterogeneous catalysis.
- Discovered a cost-effective method to synthesize a rare self-healing mineral in laboratory.
- Developed a safe and efficient catalytic hydrogen release process from ammonia borane using this mineral.
- Performed industrial hydrogenation reactions (e.g. hydrogenation of drug molecules) by the use of released hydrogen.

Photocatalytic Hydrogen Generation from Water

- Explored hydrogen production from water through photocatalysis using MOFs.
- Mapped the relation between chemical and structural characteristics of MOFs and hydrogen generation performance.

Additional Activities

- Participated in an interdisciplinary collaboration project (PrISMa) for process-informed design and synthesis of MOFs for gas adsorption and separation applications.
- Assisted teaching for several chemical engineering design and laboratory courses.
- Charged as unit safety coordinator (COSEC) of Laboratory of Molecular Simulation.

Koç University Nanomaterials, Energy and Molecular Modeling Laboratory, *MSc Thesis*

2017

- Worked on the purification of flue gas and natural gas mixtures.
- Improved the gas adsorption and separation performances of MOFs by the incorporation of ionic liquids.
- The resulting composite materials performed better CO₂/CH₄ and CO₂/N₂ separation than MOFs.

Istanbul Technical University Membrane Laboratory, *Graduation Project*

2016

- Worked on the development of mixed-matrix membranes prepared with ionic liquids and zeolites for gas separation.

Arcelik Group, *R&D Intern*

2014

- Analyzed the decolorization and disinfection effects of caustic soda and hypochlorous acid on textiles and rinse water.

Bayer CropSciences, *Quality Control Laboratory Intern*

2013

- Performed physical and chemical analyses of fungicides, herbicides and insecticides in quality control laboratory.

EXPERTISE

- **Design and synthesis of organic and inorganic structures:** Metal-organic frameworks (MOFs), organic ligands, metal nanoparticles, metal oxides.
- **Characterization and analysis techniques:** Powder X-ray diffraction (PXRD), thermogravimetric analysis (TGA), nuclear magnetic resonance (NMR) spectroscopy, infrared (IR) spectroscopy, photoluminescence (PL) spectroscopy, scanning electron microscopy (SEM), gas chromatography (GC), volumetric and gravimetric gas adsorption systems.
- **Data analysis and reporting:** Origin, MestReNova, Mercury, ChemDraw, Latex.

LANGUAGES

Turkish (native), English (advanced), French (A2).

AWARDS

- The Scientific and Technological Research Council of Turkey (TUBITAK) Scholarship, 2015-2017.
- Koç University Master's Fellowship, 2015-2017.

SCIENTIFIC OUTPUT

Journal Articles

- F. P. Kinik, A. Ortega-Guerrero, F. M. Ebrahim, C. P. Ireland, O. Kadioglu, A. Mace, M. Asgari, and B. Smit, "Towards optimal photocatalytic hydrogen generation from water using pyrene-based metal-organic frameworks", *in preparation*.
- F. P. Kinik, A. Ortega-Guerrero, D. Ongari, C. P. Ireland, and B. Smit, "Pyrene-Based Metal Organic Frameworks: From Synthesis to Applications", *ChemSocRev* 2021, 50, 3143-3177. DOI: 10.1039/D0CS00424C.
- F. P. Kinik, S. Kampouri, F. M. Ebrahim, B. Valizadeh, K. C. Stylianou, "Porous Metal-Organic Frameworks for Advanced Applications", *Reference Module in Chemistry, Molecular Sciences and Chemical Engineering*, Elsevier, 2020. DOI: 10.1016/B978-0-08-102688-5.00011-8.
- F. P. Kinik, T. N. Nguyen, K. C. Stylianou, B. Smit, "Sustainable Hydrogenation of Nitroarenes to Anilines with Highly Active in-situ Generated Copper Nanoparticles", *ChemCatChem* 2020, 12, 2833–2839. DOI: 10.1002/cctc.202000150.
- F. P. Kinik, T. N. Nguyen, E. Oveisi, B. Valizadeh, F. M. Ebrahim, A. Gładysiak, M. Mensi, K. C. Stylianou, "Discovery of a Self-Healing Catalyst for the Hydrolytic Dehydrogenation of Ammonia Borane", *Journal of Materials Chemistry A* 2019, 7, 23830-23837. DOI: 10.1039/C9TA02123J.
- F. P. Kinik, A. Uzun, S. Keskin, "Ionic Liquid/Metal–Organic Framework Composites: From Synthesis to Applications", *ChemSusChem* 2017, 14, 2842-2863. DOI: 10.1002/cssc.201700716.
- B. Koyuturk, C. Altintas, F. P. Kinik, S. Keskin, A. Uzun, "Improving Gas Separation Performance of ZIF-8 by [BMIM][BF₄] Incorporation: Interactions and Their Consequences on Performance", *The Journal of Physical Chemistry C*, 2017, 19, 10370-10381. DOI: 10.1021/acs.jpcc.7b00848.
- F. P. Kinik, C. Altintas, V. Balci, B. Koyuturk, A. Uzun, S. Keskin, "[BMIM][PF₆] Incorporation Doubles CO₂ Separation in ZIF-8: Elucidation of Interactions and Their Consequences on Performance", *ACS Applied Materials & Interfaces* 2016, 8, 30992-31005. DOI: 10.1021/acsami.6b11087.

Conference Presentations

- AAAFM International Conference on Advances in Functional Materials, *United States*, 2019.
- Latsis Symposium: 12th International Symposium Hydrogen & Energy, *Switzerland*, 2018.
- American Institute of Chemical Engineers Annual Meeting, *United States*, 2016.

PERSONAL INTERESTS

Hiking and skiing, jewelry design, painting, cooking.

PERSONAL DETAILS

Nationality: Turkish (Swiss B permit since September 2017).

Date / Place of Birth: 24.07.1992 / Istanbul, Turkey.